Applications of ultra-high-field magnetic resonance imaging (MRI) and proton magnetic resonance spectroscopy (^{1}H-MRS) in preclinical research

by

Ivina Mali

B.S., Purbanchal University, 2016

AN ABSTRACT OF A DISSERTATION

submitted in partial fulfillment of the requirements for the degree

DOCTOR OF PHILOSOPHY

Department of Chemistry
College of Arts and Sciences

KANSAS STATE UNIVERSITY
Manhattan, Kansas

2022

Abstract

Magnetic resonance imaging (MRI) is widely used to non-invasively evaluate anatomical and physiological properties of tissues in both clinical and preclinical studies making it the gold standard in medical imaging. The protocols and workflows for MRI are well established; such is not the case for Magnetic Resonance Spectroscopy (MRS). In contrast to MRI or as a complement, MRS provides biochemical composition and quantitative information of the tissue being analyzed. Modern MRI scanners can be used for MRS without any hardware modifications. MR scanners used in the clinic are of low field strength (1.5 Tesla (T) or 3 T) and require contrast agents to improve the visibility of tissue structures. On the other hand, small animal imaging requires scanners of high field strength to acquire higher resolutions to visualize similar structures and produce clinically translatable results. In this study, we use an ultra-high-field scanner of 14.1 T and optimized pulse sequences to obtain MRI and image-guided-MRS data of high spatial and spectral resolution, respectively.

This work focuses on small animal models of solid tumors and neurological disorders. We monitored the growth of pancreatic ductal adenocarcinomas (PDAC) on C57BL/6 mice using a RARE (Rapid Acquisition with Relaxation Enhancement) pulse sequence after tumor implantation. MRI-guided thermal treatments were applied to mouse models of PDACs and aldosterone-producing adenoma *in vivo*. To evaluate the tissues before and after treatment, T1 mapping techniques were used.

Another objective of this study was to use single voxel ^{1}H-MRS (Proton MRS) techniques to study metabolite levels in cell lines and tissues *ex vivo*. We used a PRESS (Point RESolved Spectroscopy) sequence to acquire spectral information from five different cell lines (four cancer and one non-cancer) and solid tumors excised from mouse models and human

subjects. Short, intermediate, and long echo times (TEs) were explored where short TE was found effective in resolving major metabolites compared to conventional long TE scans. Spectra with high SNR (signal-to-noise ratio) were acquired from voxel sizes up to 2 x 2 x 2 mm^3.

The current work also uses the valproic acid (VPA) model of autism spectrum disorder (ASD) in rodents. We collected 3D MRI scans to measure gray matter volumes in cerebellar and frontal regions of VPA-treated and control rat brains *ex vivo*. High-resolution MRI data allowed accurate segmentation across different regions of the rat brains. Altogether, we demonstrate diverse applications of MRI and image-guided ^{1}H-MRS in preclinical studies using an ultra-high-field scanner.

Applications of ultra-high-field magnetic resonance imaging (MRI) and proton magnetic resonance spectroscopy (^{1}H-MRS) in preclinical research

by

Ivina Mali

B.S., Purbanchal University, 2016

A DISSERTATION

submitted in partial fulfillment of the requirements for the degree

DOCTOR OF PHILOSOPHY

Department of Chemistry
College of Arts and Sciences

KANSAS STATE UNIVERSITY
Manhattan, Kansas

2022

Approved by:

Co-Major Professor
Dr. Christine Aikens

Approved by:

Co-Major Professor
Dr. Stefan Bossmann

Copyright

Abstract

Magnetic resonance imaging (MRI) is widely used to non-invasively evaluate anatomical and physiological properties of tissues in both clinical and preclinical studies making it the gold standard in medical imaging. The protocols and workflows for MRI are well established; such is not the case for Magnetic Resonance Spectroscopy (MRS). In contrast to MRI or as a complement, MRS provides biochemical composition and quantitative information of the tissue being analyzed. Modern MRI scanners can be used for MRS without any hardware modifications. MR scanners used in the clinic are of low field strength (1.5 Tesla (T) or 3 T) and require contrast agents to improve the visibility of tissue structures. On the other hand, small animal imaging requires scanners of high field strength to acquire higher resolutions to visualize similar structures and produce clinically translatable results. In this study, we use an ultra-high-field scanner of 14.1 T and optimized pulse sequences to obtain MRI and image-guided-MRS data of high spatial and spectral resolution, respectively.

This work focuses on small animal models of solid tumors and neurological disorders. We monitored the growth of pancreatic ductal adenocarcinomas (PDAC) on C57BL/6 mice using a RARE (Rapid Acquisition with Relaxation Enhancement) pulse sequence after tumor implantation. MRI-guided thermal treatments were applied to mouse models of PDACs and aldosterone-producing adenoma *in vivo*. To evaluate the tissues before and after treatment, T1 mapping techniques were used.

Another objective of this study was to use single voxel ^{1}H-MRS (Proton MRS) techniques to study metabolite levels in cell lines and tissues *ex vivo*. We used a PRESS (Point RESolved Spectroscopy) sequence to acquire spectral information from five different cell lines (four cancer and one non-cancer) and solid tumors excised from mouse models and human

subjects. Short, intermediate, and long echo times (TEs) were explored where short TE was found effective in resolving major metabolites compared to conventional long TE scans. Spectra with high SNR (signal-to-noise ratio) were acquired from voxel sizes up to 2 x 2 x 2 mm^3.

The current work also uses the valproic acid (VPA) model of autism spectrum disorder (ASD) in rodents. We collected 3D MRI scans to measure gray matter volumes in cerebellar and frontal regions of VPA-treated and control rat brains *ex vivo*. High-resolution MRI data allowed accurate segmentation across different regions of the rat brains. Altogether, we demonstrate diverse applications of MRI and image-guided ^{1}H-MRS in preclinical studies using an ultra-high-field scanner.

Table of Contents

List of Figures

List of Tables

Acknowledgements

I am extremely grateful to the following people who helped and supported me throughout this journey.

Principal Investigator/Co-Advisor
Dr. Stefan H. Bossmann

Co-Advisor
Dr. Christine Aikens

Collaborators
Dr. Tej Shrestha
Dr. Punit Prakash
Dr. Bethany Plakke
Dr. Matthew T. Basel
Dr. Mary Cain
Dr. Kimberly Kirkpatrick
Dr. Christopher Culbertson
Dr. Andrew Godwin
Dr. Thomas Mueller

KSU Faculty and Staff
Dr. Daniel Higgins
Dr. Christer Aakeroy
Dr. Ryan Rafferty
Dr. Simon Sham
Dr. Mark Weiss
Marla Pyle
Jim Hodgson
Bart Bath
Tobe Eggers

Supervisory committee members
Dr. Stefan H. Bossmann
Dr. Christine Aikens
Dr. Christopher Culbertson
Dr. Bethany Plakke
Dr. Santosh Aryal

Bossmann Group
Dr. Obdulia Covarrubias-Zambrano
Dr. Kayla Echliman
Dr. Jose Covarrubias
Dr. Macy Payne
Sumia Ehsan
Raul Neri

Postdoctoral and Graduate Researchers
Dr. Jan Sebek
Dr. Jay Sibbitts
Alma Romualdo Pahua
Abby Kreznor

Funding
Midwest Institute of Comparative Stem Cell Biotechnology
National Institute of General Medical Science GM113109

Friends and Family
Bhimmaya Mali
Iman Mali
Christina Thapa
Jordan Gipper
Lori Gipper
Tim Gipper
Kayla Echliman
Steven Echliman
Sumia Ehsan
Sabita Ranabhat
Sagar Rayamajhi
Edruce Edouarzin
Annika Pattison
Logan Trowbridge
Macy Payne
Katharine Bossmann
Rijesh Karmacharya
Priyasha Shrestha
Anuja Paudyal
Tej Man Tamang
Sandeep Shrestha
Gaurav Shrestha
Rabina Shrestha
Sushovita Pal

Dedication

To my late father

Dharma Mali

Chapter 1 - Introduction to Magnetic Resonance Imaging and Spectroscopy

Magnetic Resonance Imaging (MRI) is a powerful and non-invasive imaging tool that provides excellent anatomical and physiological details without any radiation exposure. It is based on the principle of Nuclear Magnetic Resonance (NMR). Isidor Rabi discovered the effect of NMR in 1938.[1] In 1946, physicists Felix Bloch and Edward Purcell measured NMR in water and solid paraffin, respectively.[2,3] The groundbreaking work of Ernst and Anderson in 1966 reports concepts of application of short radiofrequency (RF) pulses and the use of Fourier Transformation (FT) technique, which led to increased sensitivity of NMR.[4] This study by Ernst and Anderson provided the theoretical background for modern NMR. The first MRI instrument was invented by Raymond Damadian in 1972, and in 1973, Paul Lauterbur created the first MR image of small water capillaries.[5] The first MR image of a human body part, a finger, was published in 1977 by Peter Mansfield followed by whole body MR images by Raymond Damadian in the same year.[6,7] Since the development of commercial MRI scanners, there have been tremendous advances made in this field. These advances include modification in field strength, hardware, pulse sequences, and image quality.[8,9] Nowadays, MRI is one of the most used imaging modalities to investigate different diseases in both clinical and preclinical studies.

Magnetic Resonance Spectroscopy (MRS), used in conjunction with MRI, is a non-invasive technique to determine tissue metabolites. While MRI is used to identify the anatomical details and physiological processes, MRS provides biochemical composition and quantitative information in the form of MR spectra. The first *in vivo* proton MRS (^{1}H-MRS) was acquired from a rat brain using a surface coil at 360.13 MHz (8.5 Tesla (T)), reported by Behar et al. in 1983.[10] In 1985, Bottomley et al. reported the first *in vivo* spatially localized human brain ^{1}H-

MRS using a 1.5 T MR scanner.[11] Early MRS studies also focused on the ^{31}P nucleus to detect the level of metabolites associated with energy, like phosphocreatine and adenosine triphosphate (ATP).[12–14] However, ^{1}H-MRS is the most commonly used because of hydrogen's higher sensitivity and high natural abundance in the human body compared to other nuclei like ^{13}C, ^{31}P, and ^{23}Na. In addition, ^{1}H-MRS can be implemented in most commercial MRI scanners without any alterations in the hardware, like transmitters, coils, and receivers.[15]

1.1 Basics of MRI

MRI makes use of powerful magnets, usually superconducting ones, to produce a strong magnetic field that aligns the magnetic moment of protons in the body along or against the applied field (B_0). Typically, these protons are aligned randomly in the tissue being imaged. The hydrogen nucleus (^{1}H) is most commonly used because of its abundance in tissue water and fat. The strong magnetic field also causes these protons to spin around them, and the frequency of spinning (also known as the Larmor or precessional frequency) depends on the strength of the primary magnetic field and the magnetic moment of the proton. Larmor frequency can further be explained by the Larmor equation, $\omega = \gamma B$, where ω is the Larmor frequency (MHz), γ is the gyromagnetic ratio (MHz / Tesla), a constant fixed for specific nucleus, and B is the magnetic field strength (Tesla). The gyromagnetic ratio for ^{1}H is 42.58 MHz / T: at 1.5 T, the Larmor frequency for ^{1}H is ~ 63 MHz.

With the application of a radiofrequency (RF) pulse to the resonance frequency, the protons can absorb the energy that flips their net magnetization from longitudinal to the transverse plane. When the RF pulse is turned off, the spins return to their original longitudinal orientation, also known as T1 relaxation (or spin-lattice relaxation), and the de-phasing of the

spins occurs, also known as T2 relaxation (or spin-spin relaxation). While doing so, the absorbed energy is emitted in the form of a signal that one or more receiver coils can detect.

Three sets of gradient coils, also known as, G_z, G_x, and G_y, are used for spatial encoding along three axes (slice selection along Z-axis, frequency encoding along X-axis, and phase encoding along Y-axis, respectively), which causes changes in the magnetic field strength resulting in spatially linear variation of the resonance frequency. This allows inverse Fourier transformation of the frequency measurements at different positions in space. The digitized values of the spatial-frequency content are stored in a temporary image space known as k-space, and different trajectories can be used to fill this space. Once it is filled, image reconstruction tools can be used. Depending on the type of tissue being imaged, the relaxation rates vary. This property along with other variables involved in the tissue are used to construct MR images.

1.2 The MRI Scanner

The MRI scanners main components are the magnet, gradient coils, radiofrequency (RF) coils and computer systems. The FONAR (Field Focused Nuclear Magnetic Resonance) corporation was founded by Damadian in 1978, which created the first commercial MRI scanner in 1980.[16] Earlier MR systems made use of permanent and resistive magnets cooled by water. Permanent magnets required low power, but they were extremely heavy and had field strengths up to 1 T. Resistive magnets were lighter than permanent magnets, however they required high power and gave even lower field strengths compared to permanent magnets. Most of the modern MR scanners are made up of superconducting magnet in a cryostat. The higher field strengths offered by superconducting magnets provide advantages over both permanent and resistive magnets. They also offer high signal to noise ratio (SNR), shorter scan times along with better image quality.[17]

Superconducting magnets are usually made of niobium/titanium (Nb-Ti) alloy with a critical temperature about 9.7 K. Critical temperature is the temperature where certain materials have zero electrical resistivity and behave as superconductors. Most superconductors are maintained below their critical temperature by using an insulated liquid helium cooled cryostat. The basic diagram of an MRI scanner is shown in **Figure 1.1**.

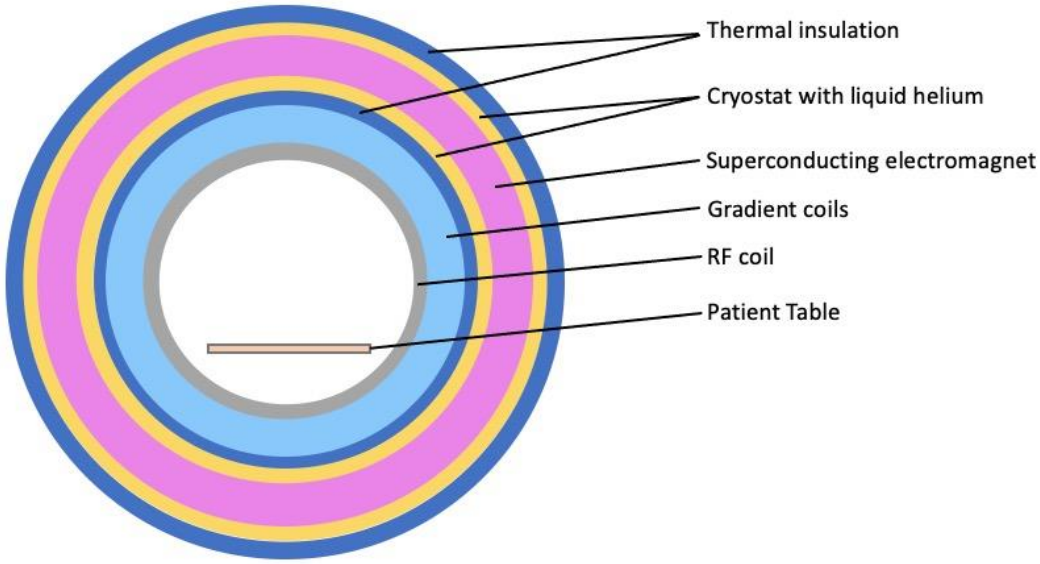

Figure 1.1 Components of an MRI scanner

The main field is generated by the superconducting magnet, maintained in a cryostat with liquid helium, which is surrounded by thermal insulation. The gradient coils inside the bore of the scanner are used for spatial localization. Two important parameters for gradient coils are maximum gradient strengths (commonly measured in mT/m) and slew rate (commonly measured in mT/m/ms). Slew rate can be defined as how fast the gradients can be switched. The third component of the MRI scanner consists of RF transmit and receive coils. The same coil can be used to transmit and receive signal, or two separate coils can be used too. There are different types of RF coils, but most of them fall under the category of either surface coils or volume coils.

Surface coils are placed adjacent to the tissue being imaged and offer good signal to noise ratio. Volume coils, on the other hand, extend over a large area and can be used for whole body imaging. A movable patient table is also used to move the subject to the isocenter of the magnet. One or more computers are used to control the gradient and RF systems for data acquisition, and to process the data. These processes are controlled by an operator via a console. To maintain a homogenous magnetic field and to reduce the effects caused by the magnet to the surrounding environment, active or passive shielding is usually employed.

1.3 MRI sequences

An MRI sequence is comprised of RF pulses and gradients, which can be controlled using several parameters. Echo time (TE) and repetition time (TR) are a few of the important parameters used in both MRI and MRS. Another important factor in a pulse sequence, signal-to-noise ratio (SNR), is used to determine the quality of images in MRI. It is measured by calculating the difference between signal intensity from the region of interest and the background noise and dividing it by the standard deviation of the signal intensity from the background.[18] Echo time is the time between the application of RF pulse and signal acquisition after excitation. Repetition time is the time between two sequential RF pulses. TE and TR, usually measured in milliseconds (ms), are two critical parameters determining the pulse sequence type and impact SNR and image quality.

Based on the pulse sequence structure, there are two main classes: spin echo (SE) and gradient echo (GE). Spin-echo pulse sequence is one of the most widely used pulse sequence in MRI and it will be discussed in this chapter. SE sequence consists of a 90° excitation pulse which flips the magnetization to the transverse plane. T2* relaxation causes the transverse magnetization (dephasing of spins) to decay much faster (also known as T2* decay). It is caused

by spin relaxation (T2 relaxation) and inhomogeneities in the primary magnetic field. The 90° excitation pulse is followed by a 180° refocusing or inversion pulse which rephases the signal to form an echo by removing the dephasing caused by inhomogeneities.[19] The general mechanism of a spin echo pulse sequence is shown in **Figure 1.2**.

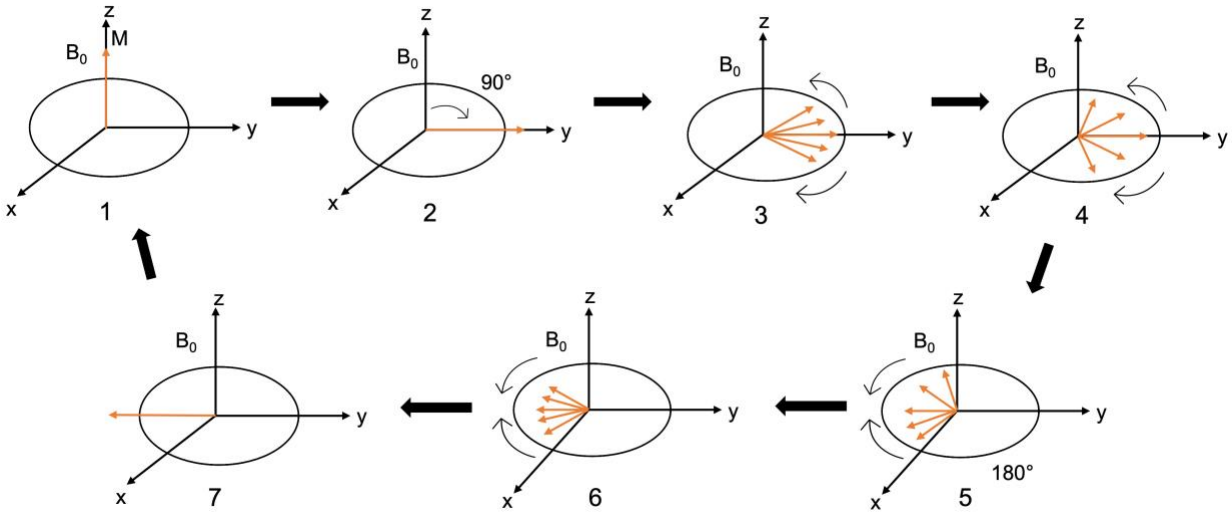

Figure 1.2 Mechanism of a spin echo sequence. Application of a 90° RF pulse flips the magnetization from longitudinal (1) to transverse plane (2). After the RF pulse is turned off the spins begin to dephase (3-4). A 180° inversion pulse rephases the spins (5-6) and a spin echo is generated (7). B_0, primary magnetic field; M, net magnetization.

The total echo time is the sum of the time between the initial 90° pulse to the 180° refocusing pulse (TE/2) and the time from application of a 180° refocusing pulse to the acquisition of the spin echo (TE/2). The time to complete this whole cycle is TR and it can be repeated multiple times along with application of spatial localization gradients. A generic spin echo pulse sequence with TE and TR is shown in **Figure 1.3**.

The slice selective gradient (G_{slice} along z-axis) is turned on during the application of any excitation pulses (90° and 180° pulses). The phase encoding gradient (G_{phase} on y-axis) is usually

applied after the 90° excitation pulse and the frequency encoding gradient ($G_{frequency}$ on x-axis) is turned on during the signal readout.

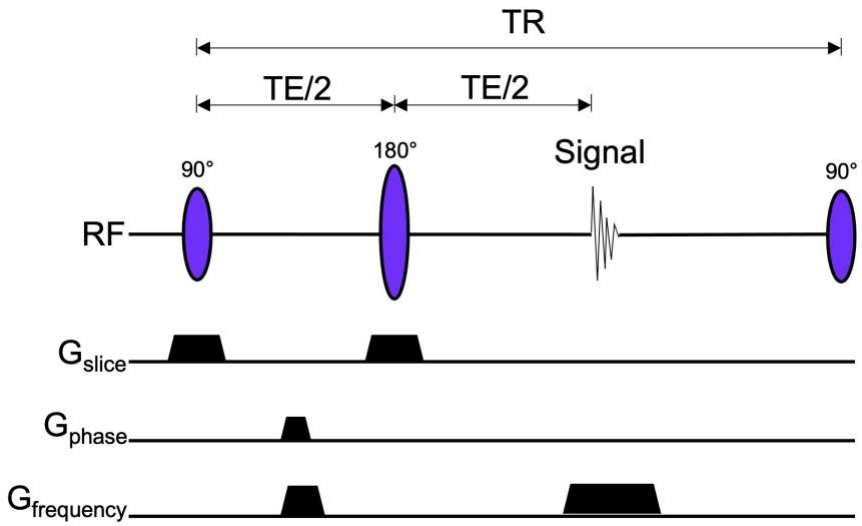

Figure 1.3 An example of a spin echo pulse sequence. TE, Echo time; TR, Repetition time; G_{phase}, $G_{frequency}$ and G_{slice} are gradients for spatial localization.

The more common MRI sequences are based on the final image contrast: T1-weighted, T2-weighted, and proton density weighted imaging.

1.3.1 T1 and T2 weighted imaging

The relaxation time of any tissue depends on its constituents. By choosing the right parameters, contrast can be enhanced between tissue types and scan time can be reduced. T1-weighted imaging is dependent on the T1 properties of tissues, and it makes use of short TEs (usually lower than 30 ms) and short TRs (usually lower than 500 ms). For instance, fat tissues have a short T1 relaxation time (~260 ms) and appear bright in T1 weighted images, whereas water and cerebrospinal fluid (CSF) appears dark due to their long T1-relaxation time (3000 - 5000ms).[20] In contrast, T2-weighted imaging makes use of long TEs (usually greater than 1500

ms) and long TRs (usually greater than 90 ms). Water appears bright and fat appears bright in T2-weighted imaging.

1.3.2 Proton density weighted imaging

Proton density (PD) weighted imaging utilizes the high density of protons rather than the magnetic properties of the protons. Tissues with high proton density appear the brightest on PD scans because transverse magnetization increases with the increase in concentration of protons in a tissue. Long TRs (usually 2000- 5000ms) and short TEs (usually 10-20ms) are used to minimize the effect of T1 and T2 properties of tissues.

1.4 Basics of MRS

MRI techniques use gradient magnetic fields to provide spatial information to generate an image, while MRS uses these fields to localize a specific volume of interest to obtain spectral information from that region. The MR spectrum consists of a plot with peaks representing signal intensities of a defined voxel against the relative shift in frequency (expressed in parts per million).

Some of the key metabolites MRS can measure are creatine, choline, N-acetyl aspartate, glutamate, γ-aminobutyric acid (GABA), lactate and, myoinositol (the structures of which are shown in **Figure 1.4**). The concentration of these metabolites can be compared within a voxel of interest, which can provide more insight to characterize the underlying disease. A majority of MRS studies have focused on neurological disorders like multiple sclerosis, epilepsy, and Alzheimer's disease; however, the applications of MRS are equally valuable in studying metabolic and psychiatric disorders.[21,22]

In ^{1}H-MRS, the signals received for metabolites within the tissue are very low compared to the signals received for water. This is because the molecular concentration of metabolites in

the tissue is 10,000 times lower than water.[23] Therefore, to obtain high-quality MRS data for metabolite quantification, different approaches must be taken. These approaches include using appropriate water suppression techniques, spatial localization using different pulse sequences, and maintaining a homogeneous magnetic field.

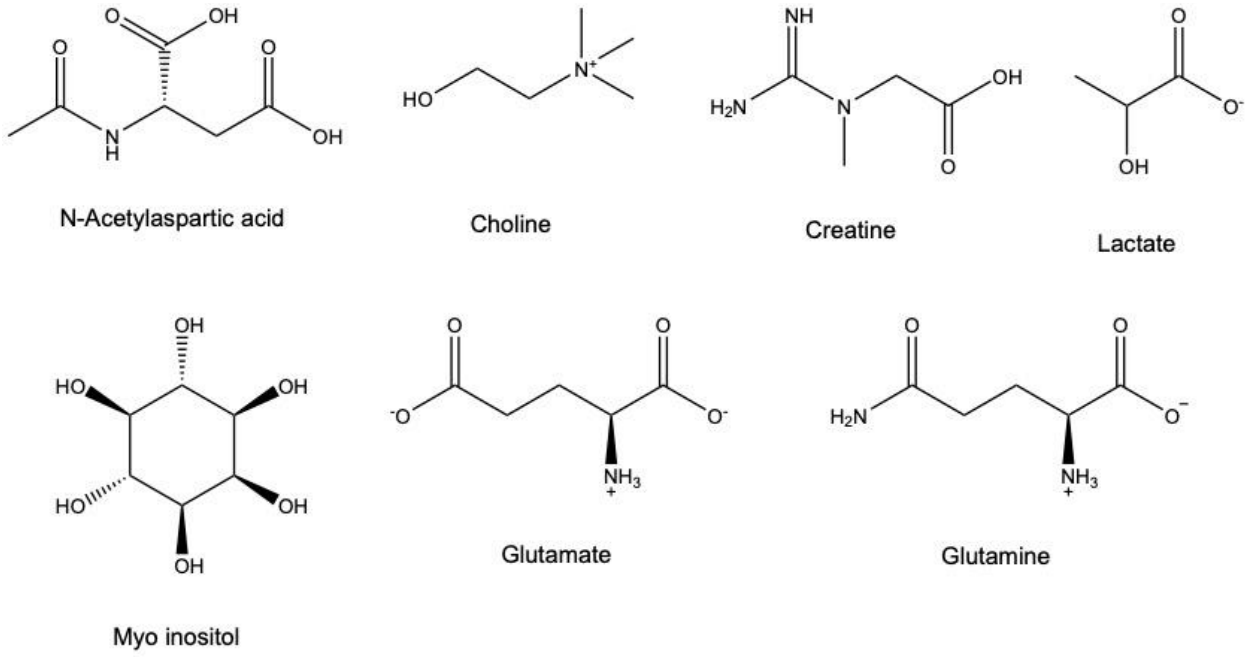

Figure 1.4 Chemical structures of common metabolites detected by ^{1}H-MRS.

Spectral data can be obtained from either a single selected region of tissue, also known as single voxel ^{1}H spectroscopy; or from multiple regions, also known as multi-voxel spectroscopy or Chemical Shift Imaging (CSI).[23,24]

1.4.1 Single Voxel ^{1}H-Spectroscopy

The purpose of this technique is to limit the acquisition of signals from a single voxel and suppress signals from outside of this region. Two of the most used pulse sequences for spatial localization in single-voxel ^{1}H-spectroscopy are PRESS (Point RESolved Spectroscopy) and STEAM (STimulated Echo Acquisition Model).

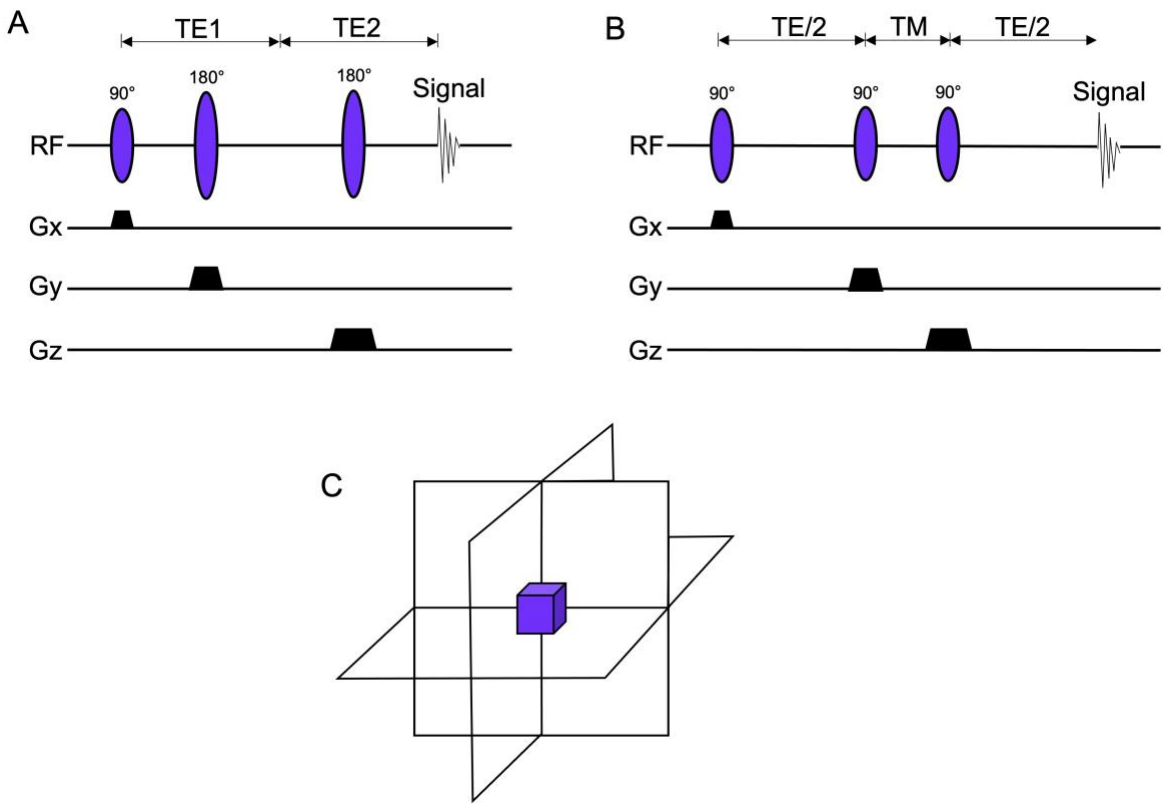

Figure 1.5 Single voxel localization methods. (A) PRESS pulse sequence (B) STEAM pulse sequence (C) Voxel where three orthogonal slices overlap; Gx, Gy, and Gz are orthogonal planes; RF, radiofrequency pulses; TE, echo time; TM, mixing time.

One of the most widely used spin-echo pulse sequences in ^{1}H-Spectroscopy is PRESS. This sequence consists of a 90° radiofrequency (RF) pulse applied concurrently with a slice-selective x-gradient to excite a slice in one direction followed by two 180° refocusing pulses with two slice-selective gradients (y and z in the orthogonal directions, respectively). Only the desired voxel where all three orthogonal slices overlap will experience the three RF pulses (**Figure 1.5 C**). The first spin echo is formed at time TE1, and the second echo is formed at time TE2 as shown in **Figure 1.5 A**, where the total echo time (TE) is TE1 + TE2.[25]

STEAM is comprised of a combination of three 90° RF pulses with three slice-selective orthogonal field gradients (x, y, and z) to acquire a stimulated echo (STE). Similar to PRESS, only the desired voxel where all three planes overlap will experience the three 90° RF pulses and

provide a signal. The time to acquire the stimulated echo depends on the time between the RF pulses. If TE/2 is the time separating the first two RF pulses and TM is the mixing time (usually a few milliseconds) that separates the second and third RF pulses, STE is acquired at time TE/2 after the third RF pulse as shown in **Figure 1.5 B**. The total time to acquire STE is TE + TM.[26,27] An example of a single voxel spectroscopy with PRESS localization in rat brain *ex vivo* is shown in **Figure 1.6**.

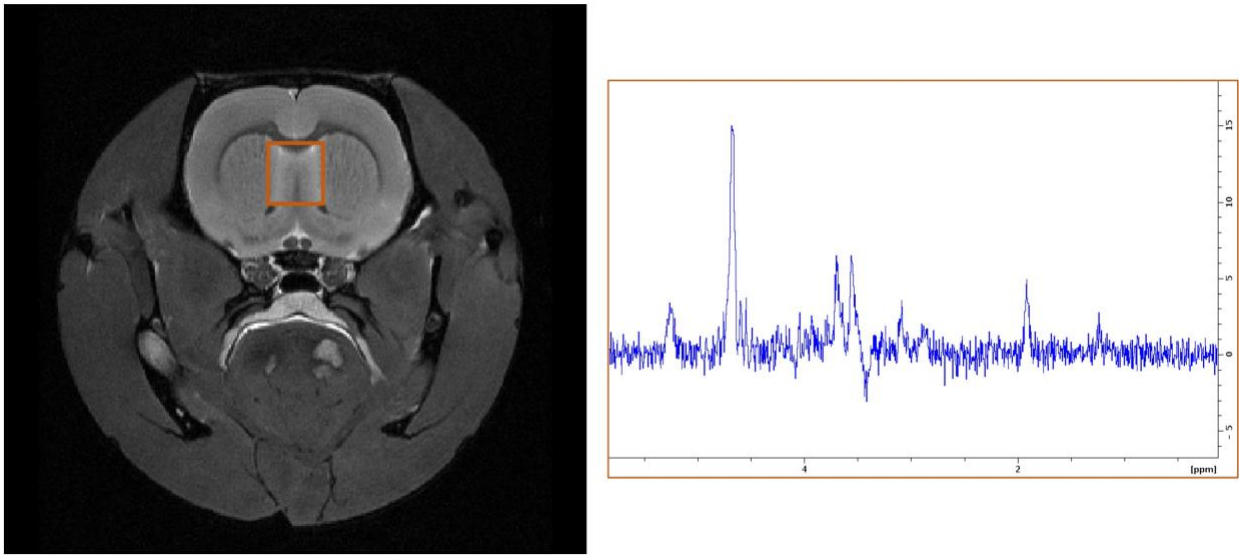

Figure 1.6 Example of a single voxel ^{1}H spectroscopy with PRESS localization in a rat brain *ex vivo*. T2 RARE MR image with voxel placement (left); Representative spectrum (right).

STEAM pulse sequence makes use of very short echo times and allows detection of metabolites with short T2 relaxation times such as myoinositol, glutamate, and glutamine.[28] However, compared to STEAM, PRESS is used more often in the clinical field because the signal to noise ratio is two times better, and it is less susceptible to motion artifacts.[27]

1.4.2 Multi voxel ^{1}H-Spectroscopy or Chemical Shift Imaging

While single voxel techniques are easy to perform with short acquisition times and excellent SNR, they are restricted to limited coverage. This can be overcome by using chemical

shift imaging (CSI) techniques. The main purpose of multi-voxel ^{1}H-spectroscopy, also known as magnetic resonance spectroscopy imaging (MRSI), is to acquire MR spectra and spatial distribution of metabolites from either a one, two, or three-dimensional array of voxels simultaneously by using a single sequence.[29] It can use the same pulse sequences as a single voxel ^{1}H-MRS (PRESS and STEAM) for localization.

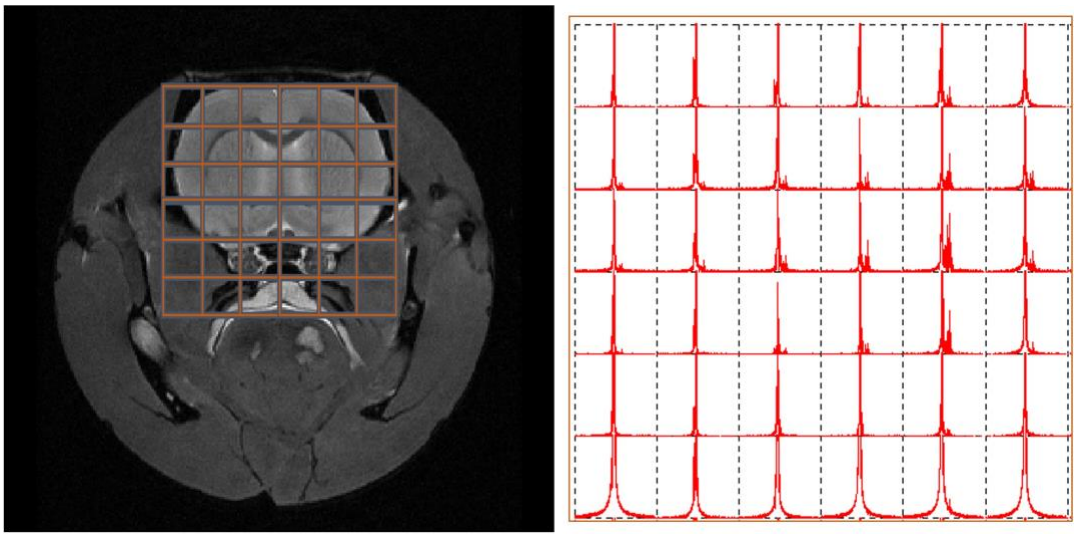

Figure 1.7 An example of *ex vivo* 2D ^{1}H-MRSI in a rat brain with PRESS localization. T2 RARE MR image with CSI grid covering the entire brain (left); Representative spectra (right).

MRSI techniques makes use of gradients for slice selection and phase encoding to obtain spatial information. RF pulse is applied simultaneously with a slice-selective gradient (Gss), followed by phase encoding gradients (Gp). This method, however, does not use a frequency encoding gradient.[30,31] An example of 2D ^{1}H-MRSI of a rat brain *ex vivo* is shown in **Figure 1.7**.

1.4.3 FAST MRSI

The conventional multi-voxel MRSI approach is an essential tool to collect spectroscopic data with broad spatial coverage. However, it comes with challenges like long acquisition times, low SNR, insufficient water suppression, and spectral contamination from neighboring voxels.[32] The long scan times and other complications make it inconvenient for clinical studies since it can

cause patient discomfort, increase in costs, and motion artifacts. Multiple fast MRSI data acquisition techniques have been developed to overcome problems arising from time-consuming MRSI sequences. Some of them are spiral, turbo, echo-planar, and parallel imaging techniques.[15,32]

Depending on the type of fast MRSI approach, they involve reducing repetition times, under sampling of k-space, reconstruction of data, and acquiring multiple k-space points per TR. These acceleration techniques and the development of powerful magnets help reduce acquisition time, minimize artifacts, increase the spatial resolution, and other benefits.[33] However, each of these techniques has its limitations as well.

1.5 References

1. Rabi II, Zacharias JR, Millman S, Kusch P. A New Method of Measuring Nuclear Magnetic Moment. *Physical Review*. 1938;53(4):318. doi:10.1103/PhysRev.53.318

2. Bloch F. Nuclear Induction. *Physical Review*. 1946;70(7-8):460. doi:10.1103/PhysRev.70.460

3. Purcell EM, Torrey HC, Pound R v. Resonance absorption by nuclear magnetic moments in a solid [7]. *Physical Review*. 1946;69(1-2):37-38.

4. Ernst RR, Anderson WA. Application of Fourier Transform Spectroscopy to Magnetic Resonance. *Review of Scientific Instruments*. 2004;37(1):93. doi:10.1063/1.1719961

5. Lauterbur PC. Image Formation by Induced Local Interactions: Examples Employing Nuclear Magnetic Resonance. *Nature 1973 242:5394*. 1973;242(5394):190-191. doi:10.1038/242190a0

6. Mansfield P, Maudsley AA. Medical imaging by NMR. *British Journal of Radiology*. 1977;50(591):188-194. doi:10.1259/0007-1285-50-591-188

7. Damadian R, Goldsmith M, Minkoff L. NMR in cancer: XVI. FONAR image of the live human body. *Physiological Chemistry and Physics*. 1977;9(1):97-100, 108.

8. Edelman RR. The history of MR imaging as seen through the pages of radiology. *Radiology*. 2014;273(2):S181-S200. doi:10.1148/radiol.14140706

9. Sobol WT. Recent advances in MRI technology: Implications for image quality and patient safety. *Saudi Journal of Ophthalmology*. 2012;26(4):393-399. doi:10.1016/j.sjopt.2012.07.005

10. Behar KL, Den Hollander JA, Stromski ME. High-resolution 1H nuclear magnetic resonance study of cerebral hypoxia in vivo. *Proc Natl Acad Sci U S A*. 1983;80(16 I):4945-4948. doi:10.1073/pnas.80.16.4945

11. Bottomley PA, Edelstein WA, Foster TH, Adams WA. *In vivo* solvent-suppressed localized hydrogen nuclear magnetic resonance spectroscopy: A window to metabolism? *Proc Natl Acad Sci U S A*. 1985;82(7):2148-2152. doi:10.1073/PNAS.82.7.2148

12. Moon RB, Richards JH. Determination of intracellular pH by 31P magnetic resonance. *Journal of Biological Chemistry*. 1973;248(20):7276-7278. doi:10.1016/S0021-9258(19)43389-9

13. Henderson TO, Costello AJR, Omachi A. Phosphate metabolism in intact human erythrocytes: determination by phosphorus 31 nuclear magnetic resonance spectroscopy. *Proc Natl Acad Sci U S A*. 1974;71(6):2487-2490. doi:10.1073/pnas.71.6.2487

14. Hoult DI, W Busby SJ, Gadian DG, Radda GK, Richards RE, Seeley PJ. Observation of tissue metabolites using 31 P nuclear magnetic resonance. *Trans Amer geophys Un*. 1974;252:169-170.

15. Zhu H, Barker PB. MR Spectroscopy and Spectroscopic Imaging of the Brain. *Methods Mol Biol*. 2011;711:203. doi:10.1007/978-1-61737-992-5_9

16. Morrow G. Progress in MRI magnets. *IEEE Transactions on Applied Superconductivity*. 2000;10(1):744-751. doi:10.1109/77.828339

17. Natukunda F, Twongyirwe TM, Schiff SJ, Obungoloch J. Approaches in cooling of resistive coil-based low-field Magnetic Resonance Imaging (MRI) systems for application in low resource settings. *BMC Biomedical Engineering 2021 3:1*. 2021;3(1):1-11. doi:10.1186/S42490-021-00048-6

18. Dietrich O, Raya JG, Reeder SB, Reiser MF, Schoenberg SO. Measurement of signal-to-noise ratios in MR images: influence of multichannel coils, parallel imaging, and reconstruction filters. *J Magn Reson Imaging*. 2007;26(2):375-385. doi:10.1002/JMRI.20969

19. Leviti MH, Freeman R. NMR population inversion using a composite pulse. *Journal of Magnetic Resonance (1969)*. 1979;33(2):473-476. doi:10.1016/0022-2364(79)90265-8

20. Westbrook C, Talbot J. *MRI in Practice 5th*. Wiley-Blackwell; 2019.

21. Rudkin TM, Arnold DL. Proton Magnetic Resonance Spectroscopy for the Diagnosis and Management of Cerebral Disorders. *Archives of Neurology*. 1999;56(8):919-926. doi:10.1001/ARCHNEUR.56.8.919

22. Dager SR, Corrigan NM, Richards TL, Posse S. Research Applications of Magnetic Resonance Spectroscopy (MRS) to Investigate Psychiatric Disorders. *Top Magn Reson Imaging*. 2008;19(2):81. doi:10.1097/RMR.0B013E318181E0BE

23. Posse S, Otazo R, Dager SR, Alger J. MR spectroscopic imaging: Principles and recent advances. *Journal of Magnetic Resonance Imaging*. 2013;37(6):1301-1325. doi:10.1002/JMRI.23945

24. Öz G, Alger JR, Barker PB, et al. Clinical proton MR spectroscopy in central nervous system disorders. *Radiology*. 2014;270(3):658-679. doi:10.1148/RADIOL.13130531/SUPPL_FILE/RADIOL.13130531.SUPPL

25. Barker PB, Lin DDM. *In vivo* proton MR spectroscopy of the human brain. *Progress in Nuclear Magnetic Resonance Spectroscopy*. 2006;49(2):99-128. doi:10.1016/J.PNMRS.2006.06.002

26. Klose U. Measurement sequences for single voxel proton MR spectroscopy. *Eur J Radiol*. 2008;67(2):194-201. doi:10.1016/J.EJRAD.2008.03.023

27. Muñoz-Hernández MC, García-Martín ML. *In vivo* 1H magnetic resonance spectroscopy. *Methods in Molecular Biology*. 2018;1718:151-167.

28. Ulmer S, Backens M, Ahlhelm FJ. Basic Principles and Clinical Applications of Magnetic Resonance Spectroscopy in Neuroradiology. *J Comput Assist Tomogr*. 2016;40(1):1-13.

29. Keevil SF. Spatial localization in nuclear magnetic resonance spectroscopy. *Physics in Medicine & Biology*. 2006;51(16):R579. doi:10.1088/0031-9155/51/16/R01

30. Bertholdo D, Watcharakorn A, Castillo M. Brain proton magnetic resonance spectroscopy: introduction and overview. *Neuroimaging Clin N Am*. 2013;23(3):359-380. doi:10.1016/J.NIC.2012.10.002

31. Faghihi R, Zeinali-Rafsanjani B, Mosleh-Shirazi MA, et al. Magnetic Resonance Spectroscopy and its Clinical Applications: A Review. *J Med Imaging Radiat Sci*. 2017;48(3):233-253. doi:10.1016/J.JMIR.2017.06.004

32. Al-Iedani O, Lechner-Scott J, Ribbons K, Ramadan S. Fast magnetic resonance spectroscopic imaging techniques in human brain- applications in multiple sclerosis. *Journal of Biomedical Science 2017 24:1*. 2017;24(1):1-19. doi:10.1186/S12929-017-0323-2

33. Bogner W, Otazo R, Henning A. Accelerated MR spectroscopic imaging—a review of current and emerging techniques. *NMR in Biomedicine*. 2021;34(5):e4314. doi:10.1002/NBM.4314

Chapter 2 - Studying the effects of thermal therapy on mouse models of solid tumors via high-resolution MRI

2.1 Background

Thermal treatments like mild hyperthermia and ablation have been studied for its potential in combination with radiotherapy and chemotherapy to kill cancer cells.[1,2] However, much of it is still experimental and more research is required to understand its therapeutic effects in detail. Thermal treatments use temperatures above the physiological temperature to shrink the tumor. In mild hyperthermia, living tissues are treated with temperatures between 41 – 45° Celsius (C) to induce cytotoxicity.[3] In contrast, ablation makes use of higher temperatures (usually above 50°C).[4] There is a strong time-temperature relationship that need to be considered while studying the effects of these treatments.[5] Current thermal treatments use different techniques to deliver heat. Most of them induce heating through microwave, ultrasound, radiofrequency, laser, and magnetic hyperthermia. These sources can be utilized to perform a local, regional, or whole-body hyperthermia.

Animal models offer valuable information in understanding different diseases and developing potential treatments. Small rodents such as rats and mice are preferred for research over other animal species since they share the same biology and genetics as humans and can closely recapitulate human diseases and conditions. They are also easily accessible, require low maintenance, have a short life cycle, and are relatively inexpensive.[6] Both, *ex vivo* and *in vivo* small animal imaging studies help in visualizing structural and functional changes associated with different disorders. Imaging modalities like micro-CT (computed tomography), micro-PET (positron emission tomography), ultrasound, and single-photon emission computerized tomography (SPECT) can be used for small animal imaging depending on the type of study.

However, these modalities suffer from limitations such as insufficient soft-tissue contrast, low spatial and temporal resolution, and poor image quality.[7]

With the use of Magnetic Resonance Imaging (MRI), repeated non-invasive imaging can be performed with excellent soft-tissue contrast, and enhanced resolution. For clinical studies, MRI scanners of low field strengths, usually 1.5 T or 3.0 T, are used. Using clinical scanners for small rodents such as mice and rats, makes it more challenging, because it is limited by smaller voxel size resulting in low signal-to-noise ratio (SNR).[8] To overcome these issues, rodent MRI require dedicated small-bore scanners of high field strength, like 7 T, 9.4 T, 14 T, or higher.[9]

This study focuses on application of microwave thermal therapy on solid tumors implanted on mouse models. Small animals implanted with tumors were either treated with mild hyperthermia or ablation therapy. Two types of mouse models were used for this study: (a) pancreatic ductal adenocarcinoma and (b) aldosterone producing adenoma.

Of all cancers, pancreatic cancer is the most aggressive, has the highest mortality rate, and the general 5-year survival rate is only 10%.[10] More than 90% of pancreatic cancer are pancreatic ductal adenocarcinoma (PDAC) that arise from the exocrine glands. The less common ones are pancreatic neuroendocrine tumors (PNETs) that arise from the endocrine glands of the pancreas.[11] Compared to PDAC, PNETs have a better prognosis. One of the main issues in pancreatic cancer is late diagnosis due to the lack of diagnostic tools and specific symptoms. Almost 80% of pancreatic cancer patients are diagnosed when the disease has metastasized to other parts of the body, leading to a life expectancy of only 4-6 months.[12] Based on the stage of the disease, treatments available after diagnosis include surgery, chemotherapy, radiation therapy, or combinations of these treatments. A better understanding of tumor progression is necessary for the early diagnosis of the disease. It is also important to use an effective preclinical

model of PDAC to monitor the progression of the disease that can closely recapitulate human PDACs.

Tumors in the adrenal glands can be benign (adenomas) or malignant (carcinomas). Adrenal carcinomas are very rare and affect 300 to 500 people in a year in the US.[13] Adenomas, on the other hand are very common, especially in the elderly population. The cortex of the adrenal glands is where most of the tumors develop. The adrenal cortex is responsible for making hormones like cortisol, aldosterone, and androgens. Tumor in this region can disrupt hormonal balance in the body. Based on the disruption of hormone levels, and the potential for adenomas to turn into cancer, treatment may vary. Surgery is the current choice of treatment if the adenoma is likely to be cancer. Non-invasive techniques like thermal ablation or hyperthermia might be helpful to manage adrenal tumors and PDACs, and to overcome challenges associated to surgery.[14]

The primary objectives of this study were: (a) to monitor the growth of pancreatic tumors in mice after tumor implantation surgery with the use of ultra-high-field MRI and optimum pulse sequences, (b) to apply mild hyperthermia on PDAC model of mice and thermal ablation on mouse models of aldosterone producing adenoma, and (c) to use T1 mapping techniques to compare changes in the tumor tissues in relation to mild hyperthermia and ablation therapy. A schematic showing the experimental flow is shown in **Figure 2.1**.

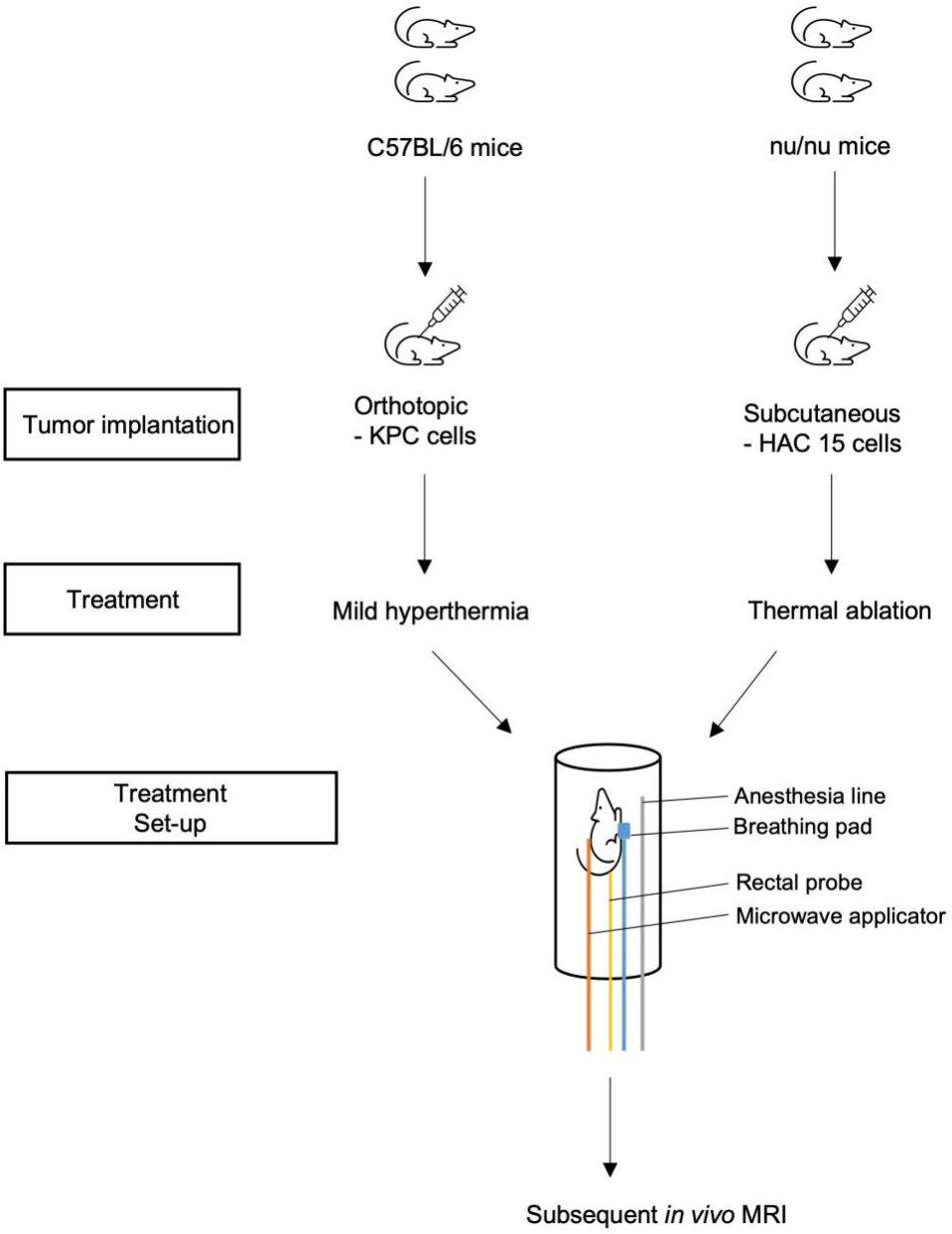

Figure 2.1 Schematic representation showing the experimental flow for application of thermal therapy on mouse models of solid tumors.

2.2 Materials and Methods

2.2.1 Tumor implantation

KPC cells, derived from primary pancreatic ductal adenocarcinoma were used for orthotopic tumor implantation in C57BL/6 mice. Cells were cultured in Dulbecco's modified eagle medium (DMEM) supplemented with 10% fetal bovine serum (FBS) and cultured in a standard cell culture incubator at 37°C in a humidified 5% CO_2 atmosphere. KPC cells were trypsinized and resuspended in a 1:1 ratio of Matrigel and phosphate-buffered saline (PBS). For implantation, a surgical incision was made in the abdominal cavity, and 50,000 KPC cells were slowly injected into the pancreatic tissue of anesthetized C57BL/6 mice.

HAC15 cells, (human adrenal gland carcinoma cells, ATCC: CRL-3301) were subcutaneously injected in the right hind flank of nude mice (nu/nu, Charles River strain #490). Approximately 6 x 10^6 HAC15 cells were used for injection. All studies with live mice were conducted following local IACUC (Institutional Animal Care and Use Committee) protocols.

2.2.2 *In vivo* MRI and heating procedure

All MRI experiments were performed in a 14.1 T vertical scanner (600 MHz Bruker Ascend III, MA, USA (**Figure 2.2 A**)). MRI probe of 30mm diameter was used for all small-animal imaging experiments. Paravision 6.0.1, a preclinical MRI software, was used to control the scanner. Mice bearing tumors were anesthetized using isoflurane (5% induction, 1–2% maintenance), and they were secured to a cradle with maintained anesthesia during all imaging experiments. For monitoring the respiratory rate during imaging, a respiration sensor was attached to the abdominal wall of the mouse. The respiration rate data was monitored using an external computer with software PC-SAM (SA Instruments Inc., Stony Brook, NY, USA) was

used. A rectal thermocouple probe (SA Instruments Inc., Stony Brook, NY, USA) was used to measure the core body temperature of the mice.

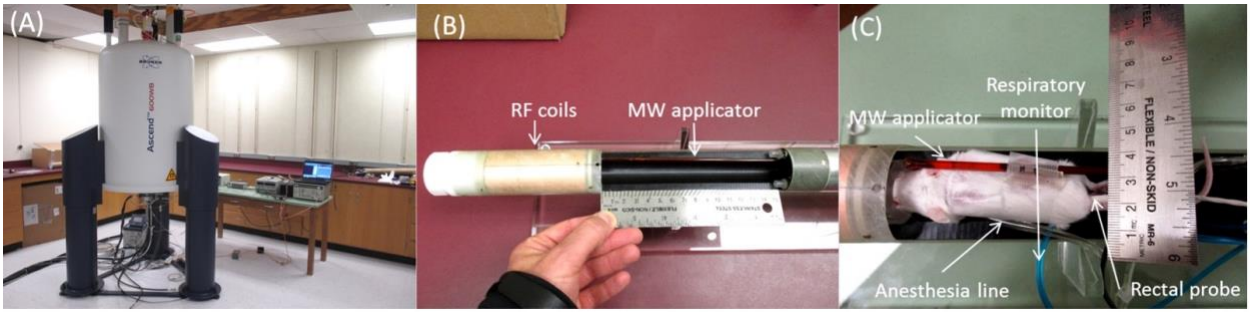

Figure 2.2 *In vivo* small animal MRI set up. (A) A picture of the 14.1 T vertical MRI scanner used in the study. (B) Micro-imaging probe of 30 mm diameter with the microwave (MW) applicator placed inside. Radiofrequency (RF) coils inside the probe are shown. (C) Example showing experimental set up for thermal therapy on a BALB/c mouse.[49]

For thermal treatment, a water-cooled microwave applicator (**Figure 2.2 B-C**) developed by the group of Dr. Punit Prakash (Department of Electrical and Computer Engineering, Kansas State University) was used. They developed a 2.45 GHz microwave thermal therapy platform that can be utilized to deliver ablation or hyperthermia treatments to small animals under MRI guidance.[15,16]

Mice were examined for tumor starting day seven post tumor implantation. For KPC mice (n = 4), upon detection of a small palpable mass, high-resolution MRI scans were acquired. Two mice were used for hyperthermia experiments and two were sham mice (control). For hyperthermia experiments, MRI scans were acquired before and after the treatment to check for movement of the sample. Two control mice were used for longitudinal study to monitor the growth of pancreatic tumor without any treatment. The MRI probe with the animal, was inserted into the scanner vertically. MRI experiments with KPC mice were performed 12 days post tumor implantation surgery on a 600 MHz Bruker Ascend. An optimized T2-TurboRARE pulse sequence (TR = 1125 ms, TE = 13.87 ms, number of averages = 4, rare factor = 8, field of view

(FOV) = 30 x 30 mm^2, matrix size = 256 x 256, slice thickness = 0.6 mm, and resolution = 0.117 x 0.117 mm^2) was used to acquire high-resolution axial, sagittal and coronal images to cover the whole tumor region. MR images were processed and visualized using ITK-SNAP software.[17]

For HAC15 mice (n = 6), once the tumor reached 5mm in one direction, mice were treated with thermal ablation. Initial evaluation of the tumor location was done with a T2-TurboRARE pulse sequence (TR = 1500 ms, TE = 14 ms, number of averages = 2, flip angle (FA) = 90°, FOV = 30 × 30 mm^2, matrix size = 256 x 256, slice thickness = 0.5 mm, and resolution = 0.11 × 0.11 mm^2).

2.2.3 T1 mapping

A modified RAREVTR (Rapid Acquisition with Relaxation Enhancement with Variable Repetition Time), a type of saturation recovery sequence, was used to collect T1 relaxation data of tumor tissues before and after thermal treatments on small animals. Initial T2-TurboRARE images were used as a reference to locate the area with tumor. Depending on the size of tumor, multiple slices were acquired for each sample to cover the entire tumor region and the surrounding tissues to see the effect of mild hyperthermia or ablation. T1 relaxation time was calculated using parameters: TE = 30.85 ms, multiple TRs = 442 ms, 884 ms, 1452 ms, 2249 ms, 3593 ms, 9942 ms, FA = 90°, FOV = 30 × 30 mm^2, matrix size = 256 x 128, slice thickness = 1 mm, number of averages = 1, and RARE factor = 8. The total acquisition time per scan was 5 mins 2 secs. For each animal, it took a total of 10 mins 4 secs to acquire the data (before and after thermal treatment).

2.3 Results

2.3.1 Monitoring tumor growth in KPC mice

High-resolution 2D axial, sagittal and coronal images were acquired using the optimized T2-TurboRARE pulse sequence to cover the whole tumor region along with surrounding tissues. RARE anatomical images were also acquired from a healthy mouse abdomen for comparison as shown in **Figure 2.3**. MRI was performed on day 12, 15, 19 and 22 after tumor implantation surgery.

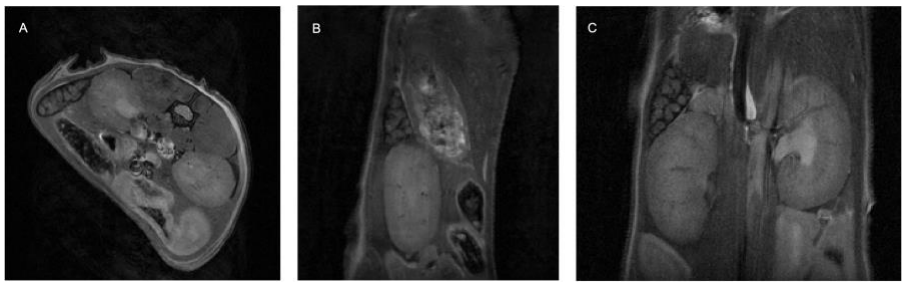

Figure 2.3 (A) Axial, (B) Sagittal, and (C) Coronal RARE anatomical images of a healthy mouse abdomen.

Longitudinal MRI experiments of orthotopic pancreatic tumors in KPC mice demonstrated an increase in the size of the tumor with age as shown in **Figure 2.4 – 2.6**. Multiple tumor masses were also observed in the axial slices (**Figure 2.4 C-D**). RARE pulse sequence, also known as fast spin-echo, was utilized in the study to minimize imaging time. With conventional spin-echo pulse sequences, a single echo is acquired with each repetition time. However, with a fast-spin echo pulse sequence, multiple echoes can be acquired with each repetition time resulting in multiple k-space lines.

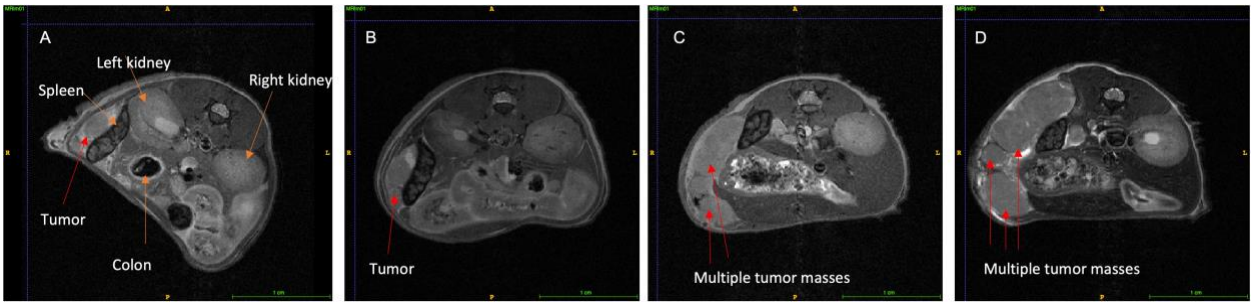

Figure 2.4 Axial RARE images of a C57BL/6 mouse bearing orthotopic pancreatic tumor (A) day 12, (B) day 15, (C) day 19, and (D) day 22 after injection of KPC cells. Red arrows indicate regions with tumor. Multiple tumor masses can be seen in (C) and (D).

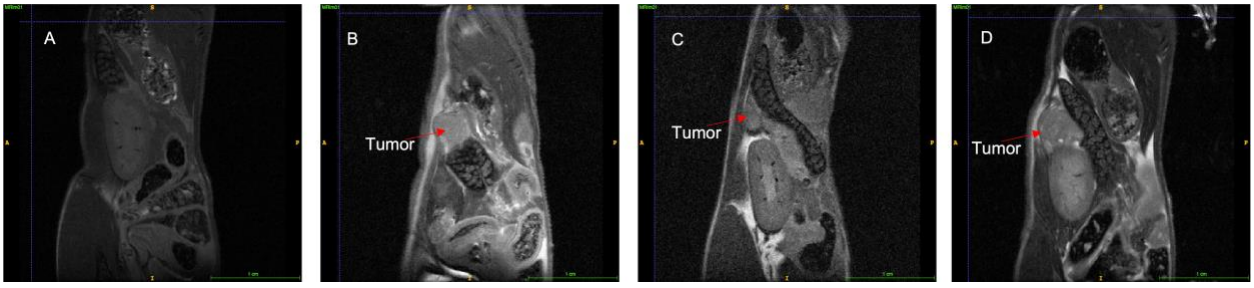

Figure 2.5 Sagittal RARE images of a C57BL/6 mouse bearing orthotopic pancreatic tumor (A) day 12, (B) day 15, (C) day 19, and (D) day 22 after injection of KPC cells. Red arrows indicate regions with tumor.

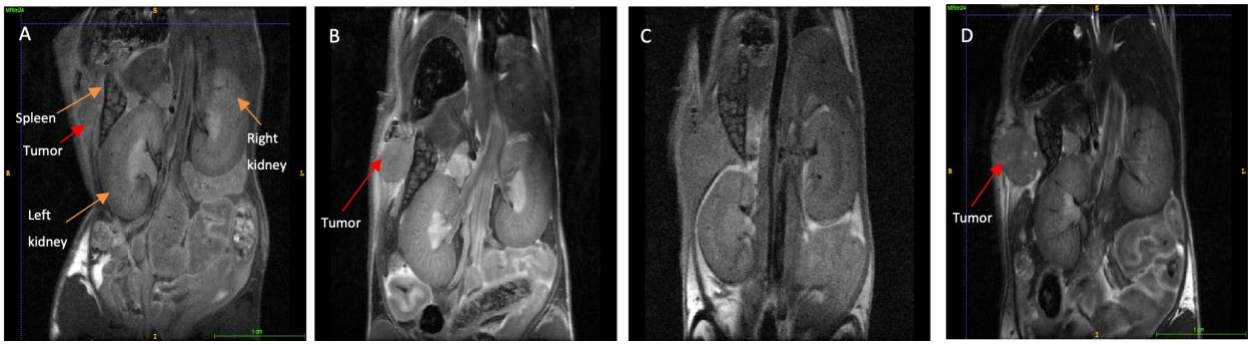

Figure 2.6 Coronal RARE images of a C57BL/6 mouse bearing orthotopic pancreatic tumor (A) day 12, (B) day 15, (C) day 19, and (D) day 22 after injection of KPC cells. Red arrows indicate regions with tumor.

This study made use of the ultra-high-field magnet and optimized pulse sequences to get high-resolution MR images of orthotopic pancreatic tumors in mice. Ultra-high-field MRI has the advantages of increased signal-to-noise and contrast-to-noise ratios without the need for any

contrast agents. Tumor tissues and vital organs in close proximity, kidneys and spleen, were clearly visible. The effect of increasing tumor size on these organs were also detectable.

2.3.2 Thermal treatments

Anesthetized mouse secured to a cradle with a rectal probe, respiratory probe, and microwave antenna was loaded into the MRI scanner vertically. Before the heating treatment, an initial MRI scan was performed to confirm on the position and rotation of the microwave applicator adjacent to the tumor tissue. Two KPC mice (Mouse 2 and mouse 3) were treated with mild hyperthermia at 42°C for 30 mins at day 16 and day 19.

Subcutaneous HAC15 tumor was treated with thermal ablation and the threshold temperature was kept 55°C. The heating treatment was terminated after the control points in the tumor region exceeded that temperature. This was done with the help of real time temperature monitoring. The treatment time was between 103 – 259 secs across experiments.[16]

During the heating experiment, cooling water was continuously circulated through the applicator. T1 maps were recorded before and after the thermal treatment during each experiment. After the treatment, mouse was removed from the scanner carefully and moved into a warm cage to let it recover. Once it recovered completely, it was transported to the animal facility. Because of the ultra-high field magnet, the orientation of the microwave applicator or antenna was clearly visible in the anatomical images as shown in **Figure 2.7 (A-C)**. Estimation of the tumor boundaries were done for all six mice with HAC15 as shown in **Figure 2.7 D**.

Out of the six HAC15 mice treated with ablation, the treatment was terminated for five mice after the temperature at the control points exceeded 55°C. In one of the treatments, the temperature did not exceed 50.5 °C (even after 250 secs) and in another treatment, data was not usable due to motion artifacts caused by the movement of animal. However, four out of the six

treatments had more than 90% of the tumor volume heated to thermal doses exceeding 240 CEM43 (240 cumulative equivalent minutes at 43°C).[16]

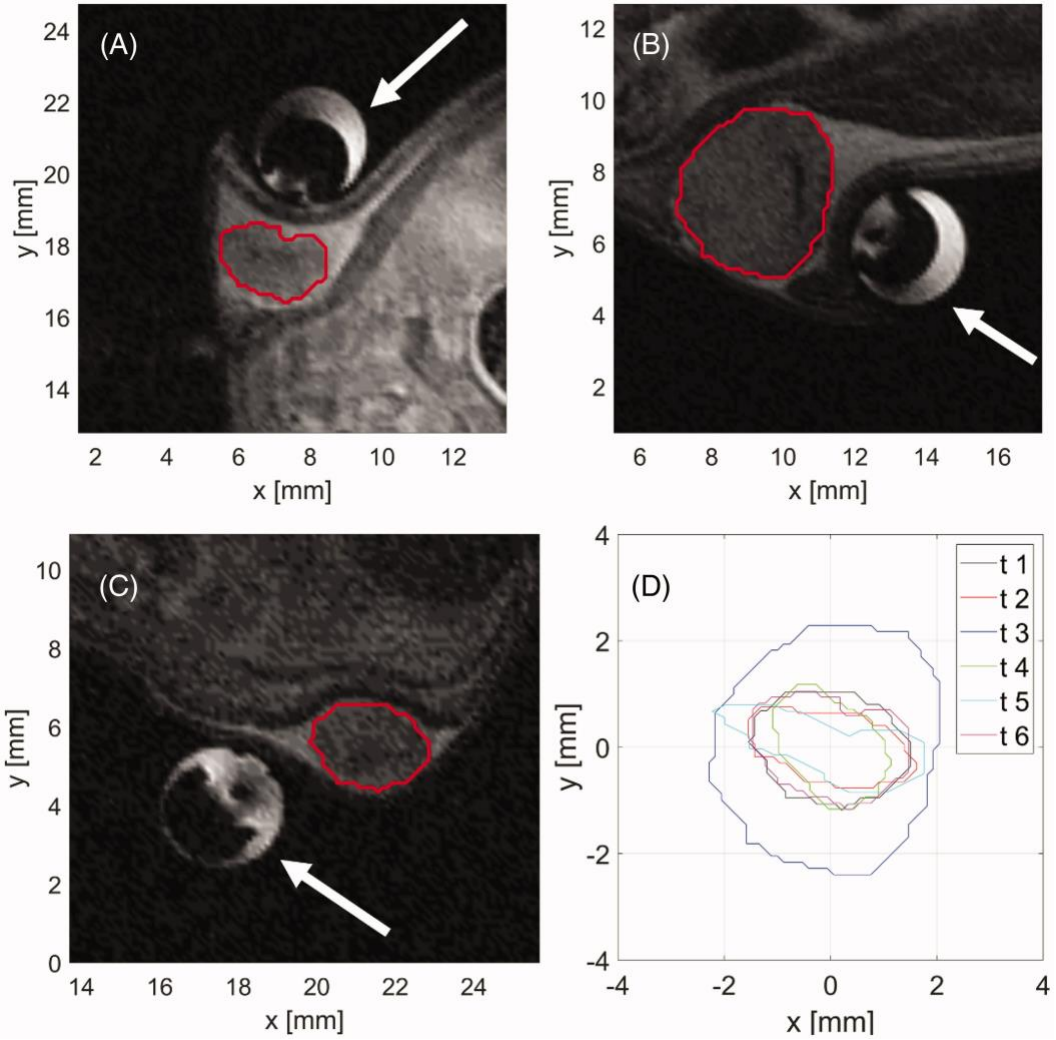

Figure 2.7 Example (A–C) anatomic MR images of subcutaneously implanted HAC15 tumors (red contour) and the microwave ablation applicator (white arrow). The boundaries of all six treated tumors (D) in a central axial plane through the tumor.[16] Adapted with permission from Sebek, J., Shrestha, T. B., Basel, M. T., Chamani, F., Zeinali, N., Mali, I., Payne, M., Timmerman, S. A., Faridi, P., Pyle, M., O'Halloran, M., Dennedy, M. C., Bossmann, S. H., & Prakash, P. (2022). System for delivering microwave ablation to subcutaneous tumors in small-animals under high-field MRI thermometry guidance. *International Journal of Hyperthermia*, *39*(1), 584–594.

2.3.3 T1 measurements

In vivo T1 relaxation values for normal tissues and tumor tissues (before and after thermal therapy) were calculated by using the software modules within Paravision 6.0.1 (ISA, Image Sequence Analysis Tool). Region of interest (ROI) based approach was used to calculate the values at different repetition times. Data was acquired in axial 2D slices to save time.

A

ROI name	ISA_1			ISA_2			ISA_3		
ROI area	0.0181 cm2			0.0181 cm2			0.0181 cm2		
parameter	value	std dev	usage	value	std dev	usage	value	std dev	usage
absolute bias	0	0	fixed	0	0	fixed	0	0	fixed
signal intensity	6.70882	0.114039	varied	4.46522	0.179026	varied	4.94997	0.107955	varied
T1 relaxation time [ms]	2687.77	70.898	varied	3206.52	230.677	varied	3071.12	126.243	varied
std dev of the fit	0.0411124			0.0933861			0.0648997		
recovery time [msec]	mean	std dev	func	mean	std dev	func	mean	std dev	func
442.15	0.99	0.24	1.02	0.62	0.156148	0.58	0.67	0.189937	0.66
884.12	1.93	0.36	1.88	1.14	0.196508	1.08	1.27	0.199744	1.24
1452.30	2.80	0.48	2.80	1.67	0.227692	1.63	1.88	0.284596	1.87
2248.94	3.80	0.66	3.80	2.26	0.225998	2.25	2.60	0.297037	2.57
3592.98	4.89	0.82	4.95	2.84	0.254596	3.01	3.25	0.372504	3.41
9942.15	6.57	1.11	6.54	4.35	0.321039	4.26	4.79	0.338499	4.76

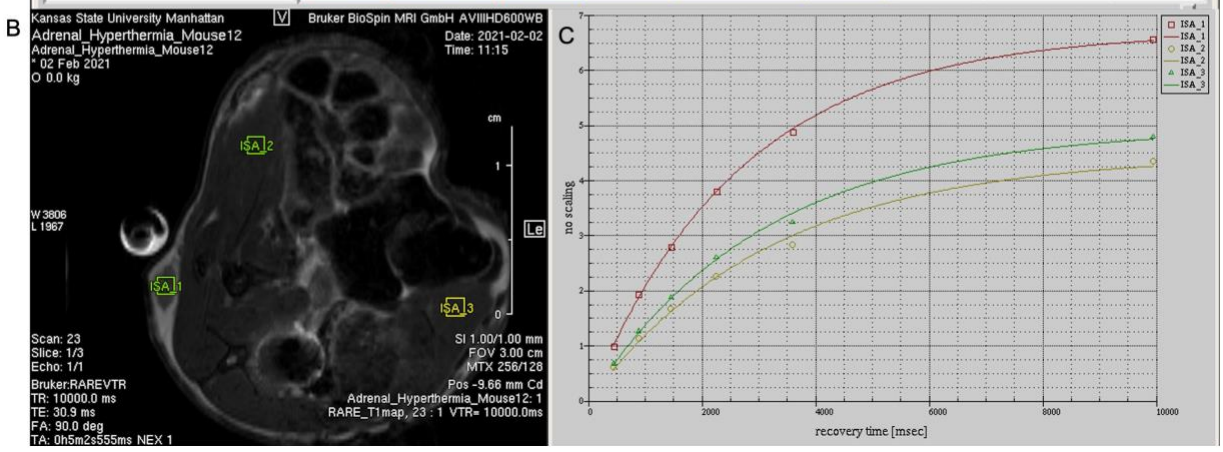

Figure 2.8 T1 relaxation values for mouse 12 with an adrenal tumor pre-ablation. (A) ISA 1 (red) is for the region with the tumor; ISA 2 and ISA 3 (yellow and black, respectively) are for regions outside the tumor. Red box with star indicates T1 relaxation times. (B) Representative image used for ROI placement is shown. (C) Representative fit showing different recovery times in msec.

A

ROI name	ISA_1			ISA_2			ISA_3		
ROI area	0.0181 cm2			0.0181 cm2			0.0181 cm2		
parameter	value	std dev	usage	value	std dev	usage	value	std dev	usage
absolute bias	0	0	fixed	0	0	fixed	0	0	fixed
signal intensity	5.5999	0.0295149	varied	5.41728	0.151062	varied	4.58671	0.0975046	varied
T1 relaxation time [ms]	2936.13	23.3496	varied	2812.98	130.519	varied	3048.43	114.54	varied
std dev of the fit	0.00960177			0.0656215			0.0530659		
recovery time [msec]	mean	std dev	func	mean	std dev	func	mean	std dev	func
442.15	0.78	0.27	0.78	0.74	0.208338	0.79	0.67	0.20751	0.62
884.12	1.46	0.36	1.46	1.54	0.318302	1.46	1.17	0.183722	1.15
1452.30	2.19	0.51	2.19	2.22	0.353003	2.18	1.78	0.19966	1.74
2248.94	2.99	0.72	3.00	2.98	0.420181	2.98	2.36	0.219436	2.39
3592.98	3.97	0.90	3.95	3.82	0.517044	3.91	3.10	0.264365	3.18
9942.15	5.40	1.26	5.41	5.30	0.699456	5.26	4.46	0.333049	4.41

B

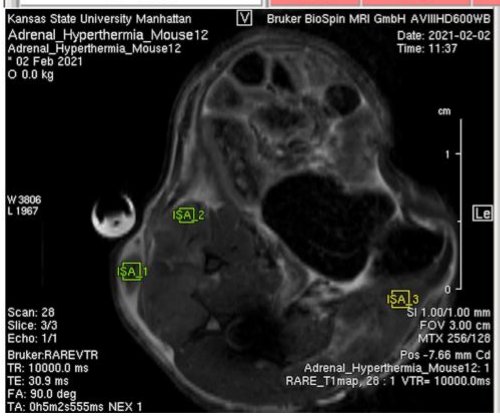

C

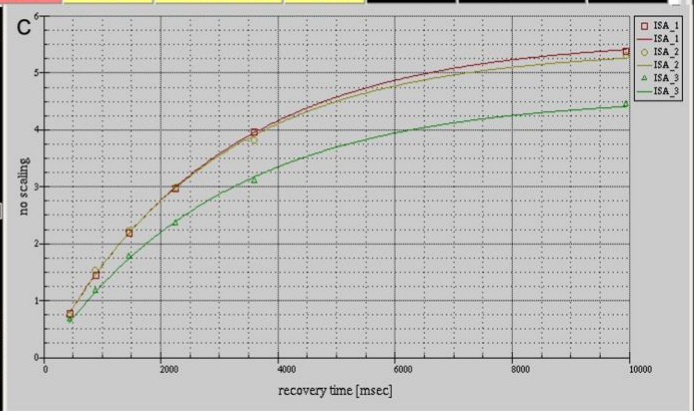

Figure 2.9 T1 relaxation values for mouse 12 with an adrenal tumor post-ablation. (A) ISA 1 (red) is for the region with the tumor; ISA 2 and ISA 3 (yellow and black, respectively) are for regions outside the tumor. Red box with star indicates T1 relaxation times. (B) Representative image used for ROI placement is shown. (C) Representative fit showing different recovery times in msec.

Among the few slices acquired for each sample, the slice that covered most of the tumor region was used for T1 estimation. The ROI area selected to get the T1 relaxation values was 0.0181cm^2 and it was kept consistent between regions and samples. An example for T1 relaxation estimation on HAC15 tumor compared to normal tissue by using the Image Sequence Analysis Tool is shown (**Figure 2.8 and 2.9**). T1 relaxation values pre-ablation is shown in **Figure 2.8** and post-ablation is shown in **Figure 2.9**. ISA_1 (blue) is the region of interest with tumor (**Figure 2.8 A and 2.9 A**). ISA_2 and ISA_3 (orange) are normal tissues outside of the

tumor region. The change in the longitudinal recovery times for ROIs is plotted in **Figure 2.8 C** and **Figure 2.9 C**. Due to movement of mouse 12, ISA_2 pre-ablation and post-ablation were two different regions and the data for ISA_2 was not used for comparison.

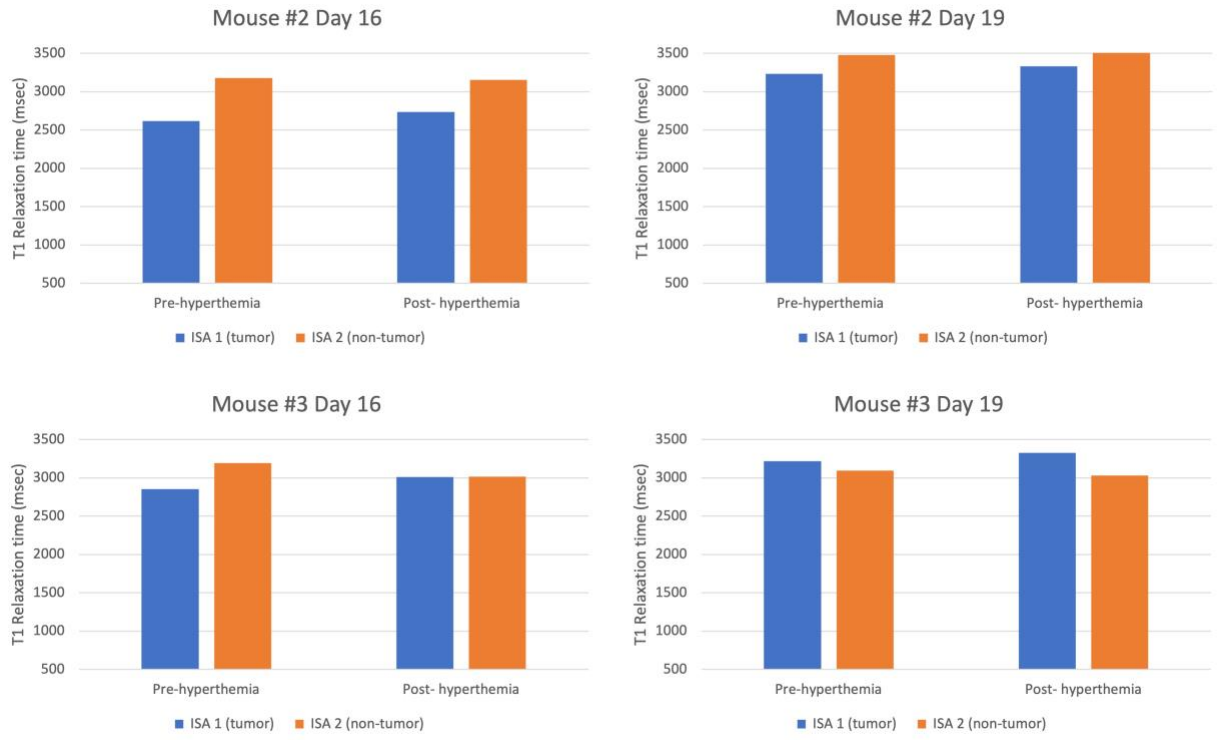

Figure 2.10 T1 relaxation data for KPC mice treated with hyperthermia on day 16 and day 19. ISA 1 (blue) is the region with tumor and ISA_2 (orange) is the non-tumor region.

T1 relaxation values acquired for two KPC mice on day 16 and day 19 before and after application of mild hyperthermia are shown in **Figure 6.1 – Figure 6.8**, and the bar graph is shown in **Figure 2.10**. The T1 relaxation time for the pancreatic tumor tissues increased after application of mild hyperthermia on both mice. For non-tumor tissues, the values did not change drastically.

Similar results were observed in adrenal tumor tissues (**Figure 6.9 – Figure 6.14**). T1 relaxation time for adrenal tumor tissues increased after the application of ablation therapy on all

four mice, whereas the T1 values remained fairly constant for non-tumor regions as shown in **Figure 2.11**.

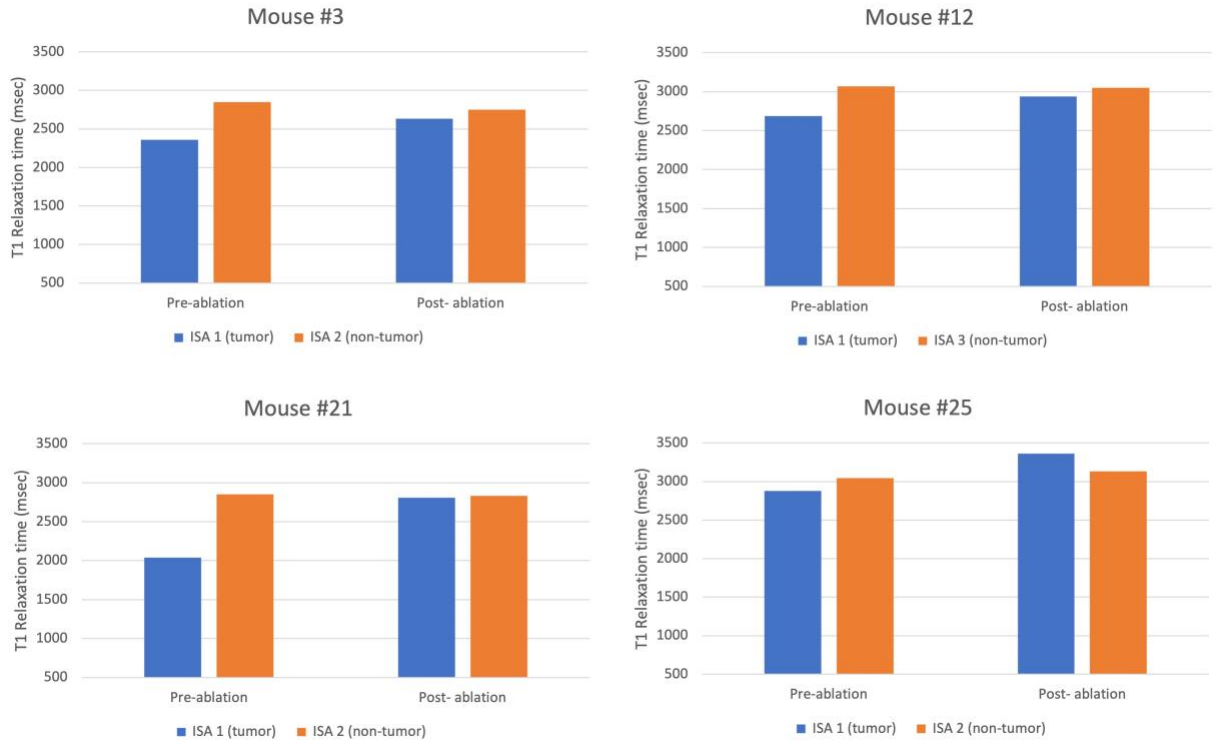

Figure 2.11 T1 relaxation data for four HAC15 mice treated with thermal ablation. ISA 1 (blue) is the region with tumor and ISA_2 and ISA_3 (orange) are the non-tumor regions.

2.4 Discussion

Chemotherapy and radiotherapy are effective in many cancers. However, PDACs are relatively resistant to them due to the accumulation of stromal desmoplasia. Desmoplastic cells are non-tumor cells that hinder vascularization, creating a hypoxic tumor microenvironment. This makes PDAC cells less sensitive to chemotherapeutics or other drugs requiring a higher dose for cytotoxic effects.[18]

The core of the tumor is usually resistant to standard treatments like chemotherapy and radiotherapy because of the low drug supply to those areas resulting from the hypoxic environment of the tumors. Thermal treatments like mild hyperthermia and ablation expands the

tumor vasculature and increases blood flow. Studies have demonstrated that localized hyperthermia combined with other anti-cancer drugs increases the accumulation of drugs to the tumor site, negatively impacting the tumor cells. Because of this, the dose of the drug can be minimized to reduce the potential side effects.[18,19]

The efficacy of mild hyperthermia has been tested on subcutaneous pancreatic cancer on rat and mouse models using ultrasound imaging.[20] However, limited research has been done on orthotopic pancreatic cancer models that adequately depict the human PDACs. KPC mouse model of PDAC, which has mutations in Kras and Trp53 is a well-validated model that closely recapitulates the features of human PDACs. It is a genetically engineered mouse model that results in solid malignancies with extensive stromal desmoplasia.[21] This study used ultra-high field MRI to monitor the growth of pancreatic tumor after tumor implantation surgery. Contrast-enhanced images were obtained without the use of contrast agents by utilizing ultra-high-field magnets and optimum pulse sequences. Optimization of the pulse sequences is essential in acquiring high-quality images with excellent signal-to-noise ratio. Image sequences such as RARE helps in speeding the imaging time, since it can acquire multiple k-space lines with each repetition time. The use of ultra-high field MRI also helped target the tumor tissues better which resulted in increasing the specificity of thermal treatments on mouse models of pancreatic tumor and adrenal tumor.

T1 mapping is a valuable quantitative MRI technique that allows the measurement of T1 or spin-lattice relaxation times of different tissues. It has been used widely to characterize myocardial and hepatocellular diseases. [22,23] Only a few studies have been reported on T1 mapping of pancreatic cancer and adrenal tumor with the use of low magnetic field strength scanners. An increase in the T1 relaxation values were observed in both mouse models after the

application of mild hyperthermia and ablation therapy. These values might be useful in discriminating tumor tissues with non-tumor tissues and to validate if a tissue underwent thermal treatment effectively.

2.5 Conclusion

In conclusion, we successfully used ultra-high field MRI to monitor the growth of PDACs in mouse models. The high-resolution acquired during MRI studies helped in increasing the specificity of mild hyperthermia and ablation therapy on KPC mice and HAC15 mice respectively. T1 mapping studies further helped in differentiating tumor tissues and normal tissues, and in studying the effects of thermal therapy on T1 relaxation properties of tumor tissues non-invasively. Moreover, this study can be used as a reference for future studies with T1 relaxation values of PDACs and HAC15 in mice with and without thermal treatments using a 14.1 T magnet, given the parameters for imaging and thermal treatments are kept constant.

Some limitations to this study are small sample size, potential off-target ablation or hyperthermia due to animal motion, and difficulty in stabilizing the microwave antenna adjacent to the region of interest. Future studies should include a bigger sample size to validate this study and gating strategies should be used to minimize artifacts due to animal motion.

2.6 References

1. Atanackovic D, Nierhaus A, Neumeier M, Hossfeld DK, Hegewisch-Becker S. 41.8°C whole body hyperthermia as an adjunct to chemotherapy induces prolonged T cell activation in patients with various malignant diseases. *Cancer Immunology, Immunotherapy 2002 51:11*. 2002;51(11):603-613. doi:10.1007/S00262-002-0327-X

2. Ahmed M, Brace CL, Lee FT, Goldberg SN. Principles of and advances in percutaneous ablation. *Radiology*. 2011;258(2):351-369. doi:10.1148/RADIOL.10081634

3. Rao W, Deng ZS, Liu J. A review of hyperthermia combined with radiotherapy/chemotherapy on malignant tumors. *Crit Rev Biomed Eng*. 2010;38(1):101-116.

4. Zhang Y, Zhang W, Geng C, et al. Thermal ablation versus conventional regional hyperthermia has greater anti-tumor activity against melanoma in mice by upregulating CD4+ cells and enhancing IL-2 secretion. *Progress in Natural Science*. 2009;19(12):1699-1704. doi:10.1016/J.PNSC.2009.05.007

5. Dewey WC. Arrhenius relationships from the molecule and cell to the clinic. *Int J Hyperthermia*. 2009;25(1):3-20. doi:10.1080/02656730902747919

6. Medicine M, Bryda EC. The Mighty Mouse: The Impact of Rodents on Advances in Biomedical Research. *Missouri Medicine*. 2013;110(3):207.

7. Brockmann MA, Kemmling A, Groden C. Current issues and perspectives in small rodent magnetic resonance imaging using clinical MRI scanners. *Methods*. 2007;43(1):79-87. doi:10.1016/J.YMETH.2007.07.001

8. Hoyer C, Gass N, Weber-Fahr W, Sartorius A. Advantages and Challenges of Small Animal Magnetic Resonance Imaging as a Translational Tool. *Neuropsychobiology*. 2014;69(4):187-201. doi:10.1159/000360859

9. Cho KH, Huang SM, Choi CH, et al. Development, integration and use of an ultra-high-strength gradient system on a human-size 3 T magnet for small animal MRI. *PLoS One*. 2019;14(6). doi:10.1371/JOURNAL.PONE.0217916

10. Pancreatic Cancer: Statistics | Cancer.Net. Accessed June 17, 2022. https://www.cancer.net/cancer-types/pancreatic-cancer/statistics

11. Pancreatic Cancer Facts - Hirshberg Foundation for Pancreatic Cancer Research. Accessed June 17, 2022. https://pancreatic.org/pancreatic-cancer/pancreatic-cancer-facts/

12. Pancreatic Cancer Treatment, Symptoms, Cause, Stages & Survival Rates. Accessed June 17, 2022. https://www.emedicinehealth.com/pancreatic_cancer/article_em.html

13. Adrenal Tumors - Symptoms, Diagnosis & Treatment | MD Anderson Cancer Center. Accessed June 18, 2022. https://www.mdanderson.org/cancer-types/adrenal-tumors.html

14. Donlon P, Dennedy MC. Thermal ablation in adrenal disorders: A discussion of the technology, the clinical evidence and the future. *Current Opinion in Endocrinology, Diabetes and Obesity*. 2021;28(3):291-302. doi:10.1097/MED.0000000000000627

15. Curto S, Faridi P, Shrestha TB, et al. An integrated platform for small-animal hyperthermia investigations under ultra-high-field MRI guidance. *https://doi.org/101080/026567362017133912*6. 2017;34(4):341-351. doi:10.1080/02656736.2017.1339126

16. Sebek J, Shrestha TB, Basel MT, et al. System for delivering microwave ablation to subcutaneous tumors in small-animals under high-field MRI thermometry guidance. *International Journal of Hyperthermia*. 2022;39(1):584-594. doi:10.1080/02656736.2022.2061727/SUPPL_FILE/IHYT_A_2061727_SM7241.PDF

17. Yushkevich PA, Piven J, Hazlett HC, et al. User-guided 3D active contour segmentation of anatomical structures: significantly improved efficiency and reliability. *Neuroimage*. 2006;31(3):1116-1128. doi:10.1016/J.NEUROIMAGE.2006.01.015

18. Farr N, Wang YN, D'Andrea S, et al. Hyperthermia-enhanced targeted drug delivery using magnetic resonance-guided focused ultrasound: a pre-clinical study in a genetic model of pancreatic cancer. *Int J Hyperthermia*. 2018;34(3):284-291. doi:10.1080/02656736.2017.1336675

19. Kong G, Anyarambhatla G, Petros WP, et al. Efficacy of Liposomes and Hyperthermia in a Human Tumor Xenograft Model: Importance of Triggered Drug Release 1. *CANCER RESEARCH*. 2000;60:6950-6957.

20. Bai Z, Shi Y, Wang J, et al. Intratumoral radiofrequency hyperthermia-enhanced direct chemotherapy of pancreatic cancer. *Oncotarget*. 2017;8(2):3591-3599. doi:10.18632/ONCOTARGET.12295

21. Lee JW, Komar CA, Bengsch F, Graham K, Beatty GL. Genetically engineered mouse models of pancreatic cancer: The KPC model (LSL-KrasG12D/+;LSL-Trp53R172H/+;Pdx-1-Cre), its variants, and their application in immuno-oncology drug discovery. *Curr Protoc Pharmacol*. 2016;2016:14.39.1-14.39.20.

22. Peng Z, Jiang M, Cai H, et al. Gd-EOB-DTPA-enhanced magnetic resonance imaging combined with T1 mapping predicts the degree of differentiation in hepatocellular carcinoma. *BMC Cancer*. 2016;16(1). doi:10.1186/S12885-016-2607-4

23. Kali A, Choi EY, Sharif B, et al. Native T1 Mapping by 3-T CMR Imaging for Characterization of Chronic Myocardial Infarctions. *JACC Cardiovasc Imaging*. 2015;8(9):1019-1030. doi:10.1016/J.JCMG.2015.04.018

Chapter 3 - Proton MRS in Investigating Cells and Solid Tumors

3.1 Introduction

Many clinical and preclinical studies have used MRS techniques for examining metabolic profiles *in vivo* and *ex vivo* for different diseases. Some of those diseases are cancer in the brain, prostate, breast, and strokes, dementia, and inflammatory and infectious diseases.[1–3] Previous studies with *in vivo* ^{1}H-MRS have shown an association of elevated levels of choline-containing compounds to malignancy, whereas normal tissues exhibit low choline levels.[4,5] Both proton MRS and MRSI are being studied for their application in studying solid tumor's metabolic features. However, acquiring high-resolution spectral information with the use of proton MRS requires a lot of technical considerations, such as spatial localization, water suppression techniques, and magnet strengths. With low field strength scanners used in clinical studies, only a few metabolites can be detected depending on the type of disease and parameters used during the study.[6] Use of high magnetic field strengths in preclinical research involving ^{1}H-MRS studies have shown potential in resolving high spectral resolutions of metabolites.

This study aims to use an ultra-high-field MR scanner and optimized ^{1}H-MRS parameters to acquire high-resolution spectral information from tumor cell lines and excised tumor tissues. Understanding the metabolic features can help build a fingerprint for each cell line, which can later be compared with the tumor cells *in vivo* to make a more accurate interpretation. MRI plays a critical role in identifying solid tumors and in monitoring the response of treatment. However, to further characterize the tumor via histopathology, biopsies are required. Non-invasive techniques like MRS have potential to replace or increase specificity of invasive techniques like biopsies by accurately identifying the chemical composition of tumor and non-tumor tissues.

While multi voxel MRSI techniques can be used to cover a larger region of interest to study tissue heterogeneity, single voxel MRS techniques are preferred for investigating solid tumors owing to their short scan times, high signal-to-noise ratio, and easy implementation. This study focuses on using single voxel MRS combined with MRI to study the metabolites in different types of cell lines. Three glioma cell lines, one pancreatic cancer cell line and one non-cancer cell line were used for the study. The data acquired for glioma cell lines were compared with excised human glioma tissues and the data acquired for pancreatic cancer cell line was compared with excised KPC tumors from mice treated and untreated with hyperthermia.

3.2 Materials and Methods

3.2.1 Cell lines and sample preparation

A total of five cell lines were used for the ^{1}H-MRS studies. The KPC cell line, derived from primary pancreatic ductal adenocarcinoma, was cultured in Dulbecco's modified eagle medium (DMEM) supplemented with 10% fetal bovine serum (FBS). The C6 cancer cell line, derived from rat gliomas, was cultured in Ham's F12K medium supplemented with 2.5% FBS, 15% horse serum, and 1% penicillin/streptomycin. U87 cell line, derived from human malignant gliomas, were cultured in DMEM supplemented with 1% penicillin/streptomycin and 10% FBS. The GL26 cell line, derived from mouse gliomas, was cultured in RPMI-1640 medium supplemented with 1% pyruvate and 10% FBS. The NSC cell line, derived from murine neural stem cells, was cultured in DMEM media supplemented with 5% horse serum, 10% FBS, 1% glutamax and 1% pyruvate.

Cells were cultured in a standard cell culture incubator at 37°C in a humidified 5% CO_2 atmosphere. Cells were lifted with 0.1 % Trypsin-EDTA and 3x respective media was added to neutralize the trypsin. An initial cell count was performed, and cell viability checked by staining

cells with trypan blue and using a TC20 automated cell counter (Bio-rad). Initial cell viability was above 90 % for all cell lines. Approximately 12 X 10^6 cells were used for all ^{1}H-MRS studies of cells. Cells were washed with PBS a few times and centrifuged at 1000 rpm for 3 mins to form a pellet.

Custom-made NMR tubes of 10 mm diameter with a flat bottom were used for this study. The cell pellet was suspended in the center of the NMR tube using 2% agarose gel. 5-6 ml of agarose was first poured in the NMR tube and transferred to a beaker with ice to solidify the agar. The cell pellet was then carefully transferred on top of the agar using 200ul PBS (Phosphate Buffered Saline). Slowly, 5-6 ml agarose was added on top of the cells. The top agar layer was allowed to solidify on ice as well. The samples were then transported to the NMR/MRI facility in an ice box. For all the samples, data was collected within 2 hours of sample preparation followed by a final cell count to check for cell viability before discarding the samples. A cell viability of 63 - 83% was observed for all cell lines.

3.2.3 Excised tissue preparation

Following MRI scans and hyperthermia experiments as explained in chapter 2, C57BL/6 mice (n = 2) were sacrificed three weeks after tumor implantation surgery and orthotopic tumors were harvested. Thigh muscle from a mouse was also harvested for relative comparison. Custom-made flat bottom NMR tubes of 10 mm diameter were used, and tissue samples were suspended in the center of the NMR tube using 2% agarose gel. 5-6ml of agarose was poured in the NMR tube and allowed to solidify on ice. The excised tissue was carefully added on top of the agar and 5ml PBS was added to cover the tissue completely.

Frozen human glioblastoma samples were acquired from the biospecimen repository core facility, The University of Kansas Cancer Center, IRB00000161/5920, IRB ID: CR00010506,

PI: Prof. Dr. Andrew Godwin. A total of six biospecimens from white patients (three males, three females) was obtained (0.20g frozen tissue (- 80˚C)). All samples were classified as Glioblastoma multiforme / WHO grade IV.

Upon arrival, the samples were transferred to -80 °C freezer. Before sample preparation, they were let to thaw at 4°C for 24 hrs. Samples were transferred to a 10 mm NMR tube and 5ml PBS was gently added using a glass Pasteur pipette.

3.2.2 MRI and MRS experiments

All MRI and ^{1}H-MRS experiments were performed on a Bruker 600MHz (14.1 T) wide-bore MR scanner. This scanner can fit imaging coils of 10 – 30 mm diameter for high-resolution imaging. For ^{1}H-MRS studies of cell lines, a 10mm diameter probe was used. The probe with the NMR tube was loaded vertically into the MR scanner. An initial estimation of sample position was done using a series of localizer scans with FLASH pulse sequence (TE = 1.64 ms, TR = 120 ms, number of averages = 1, matrix size = 128 x 128, FOV = 10 x 10 mm^2, resolution 0.078 x 0.078 mm^2, and scan time = 23 secs). A B_0 map was acquired, and automatic map shim was performed to optimize the homogeneity of the field in the region of interest. T2 RARE pulse sequence with varying TE and TRs was used to acquire axial, sagittal, and coronal images for voxel positioning. Other parameters used were: RARE = 4, averages = 2, image size = 128 x 128, FOV = 10 x 10 mm^2, resolution 0.078 x 0.078 mm^2, and slice thickness = 0.5 - 0.7 mm.

^{1}H-MRS data was acquired using a PRESS pulse sequence. Bruker PRESS sequence was modified to acquire the spectral data with a wider range of metabolites. A TE / TR of 16.17 / 2500 and 68 / 1500 was tested on cell lines based on previous studies. An isotropic voxel of 2.5mm was placed within the center of the cell pellet (using the RARE data as a reference). An initial PRESS sequence with VAPOR (VAriable Power and Optimized Relaxations delays) water

suppression pulses and OVS (Outer Volume Suppression) was acquired with 64 averages. For voxel specific shim adjustment, local shim was also performed. The area picked for local shim was slightly bigger than the voxel size, to avoid spectral contamination from neighboring area. The total scan time was 2 min 40 secs. After evaluating the initial scan, a PRESS scan with TE/TR of 16.17 / 2500 with 1024 averages was run and the total scan time was 42 mins 40 secs. For PRESS scan with TE / TR of 68 / 1500 with 1024 averages, the total scan time was 25 mins 36 secs. A scan without water suppression was also acquired for comparison.

A similar method was followed for ^{1}H-MRS of excised tumor samples. A set of localizer scans followed by T2 RARE scans were acquired in axial, sagittal and coronal orientation. For ^{1}H-MRS, PRESS sequence with VAPOR water suppression and OVS was used with voxel specific shim adjustments. Voxel size was 2.5 x 2.5 x 2.5 mm^3 for KPC tumor samples and 2 x 2 x 2 mm^3 for human glioblastoma samples. A TE / TR of 16.17 / 2500 ms was used for KPC tumor tissues. Three different TEs (30 ms, 68 ms, and 125 ms) were tested for ^{1}H-MRS of human glioblastoma samples.

3.2.3 Data Analysis

Completed scans (Localizers and T2 RARE images) were viewed directly on the examination card in the Paravision software. These scans were used as a reference to plan new MRS scans. All MR images were also exported to dicom format using the Paravision software, to allow visualization using external software like ITK-SNAP.[7] For PRESS data, once the scan ran to completion, it was exported to TopSpin software (Bruker software for spectroscopy analysis). A quick qualitative analysis of the spectra was done using TopSpin software, after Fourier Transformation (FT) of the signal. For a detailed analysis, an external software Chenomx

(Chenomx Inc. Edmonton, Canada) was used. Chenomx was used to process the spectra and to identify the metabolites, based on the library of metabolites it has for different magnet strengths.

3.3 Results

3.3.1 MRI-guided ^{1}H-MRS of cell lines

Figure 3.1 A shows a 10 mm NMR tube with cell pellet in the center, and agar layers on the top and bottom. T2 RARE images acquired in axial, sagittal and coronal orientation for KPC cells are presented in **Figure 3.1 (B-D)**. A 2.5 mm isotropic voxel covering the cell pellet is also shown in the RARE images.

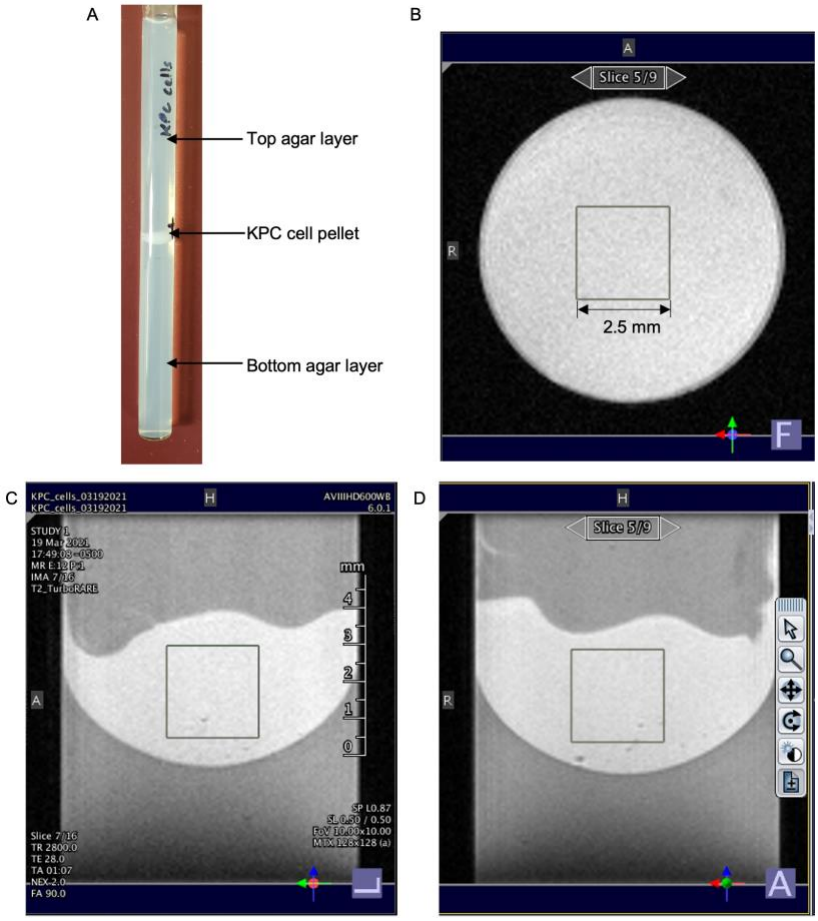

Figure 3.1 Experimental set-up for ^{1}H-MRS of cell lines. 10 mm NMR tube showing KPC cells suspended in between the agar layers (A). T2 RARE axial (B), sagittal (C), and coronal (D) images showing voxel positioning in KPC cell pellet. Voxel size = 2.5 mm isotropic, TE = 28 ms and TR = 2800 ms.

Figure 3.2 shows the spectrum acquired for KPC cells without water suppression. No major metabolites were visible due to the huge water peak suppressing the signal from other compounds. **Figure 3.3** represents spectra of KPC cells with VAPOR water suppression. Spectra were acquired from KPC cells at two different passage numbers to study its effects on the level of metabolites detected by ^{1}H-MRS. The spectrum for KPC cells for passage number 42 is shown in black and for passage number 29 is shown in green in **Figure 3.3**.

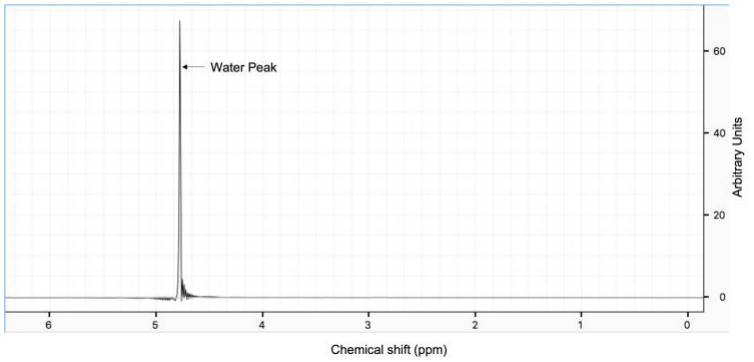

Figure 3.2 ^{1}H-MRS of KPC cells without water suppression. No metabolites are visible without application of water suppression pulses.

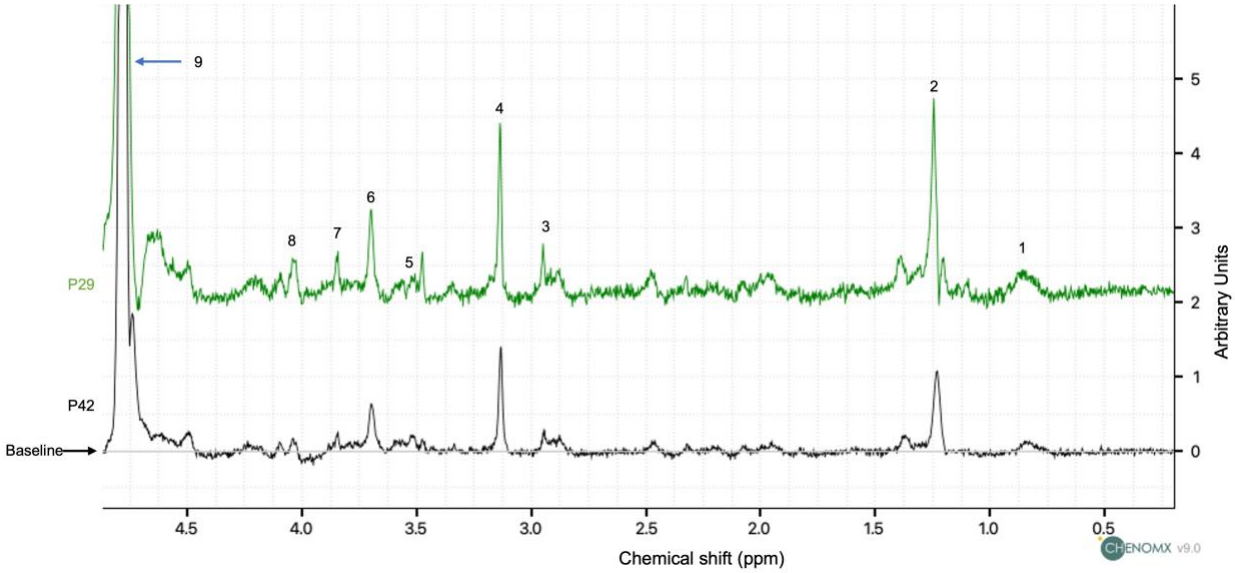

Figure 3.3 ^{1}H-MRS of KPC cells with VAPOR water suppression. Spectrum for KPC cells Passage 49 (P49) is shown in black and for Passage 29 (P29) is shown in green. Signals were present from lipid and lactate (1-2), creatine (3, 7), total choline (4), inositol (5, 8), glutamine/glutamate (6). Residual water is shown with a blue arrow (9). Baseline is shown with a black arrow.

Phase correction was applied to the spectra using the Processor module of Chenomx software, followed by a baseline correction. With VAPOR water suppression, signals from major metabolites were detected. These metabolites include lipid, lactate, creatine, total choline, inositol, and glutamine/glutamate. A decrease in the metabolite concentration was observed in KPC cells of higher passage number (P42) compared to lower passage number (P29) as shown in **Figure 3.3**.

A TE/TR of 16.17 / 2500 was found suitable compared to a TE/TR of 68 / 1500 to acquire ^{1}H-MRS data from cell lines. An example for spectra acquired for GL26 cells with 256 averages and different TE/TR is shown in **Figure 3.4**. Higher signal intensities and better spectral resolution were observed for data collected with short echo time even with 256 averages (scan time = 10 mins 40 sec)

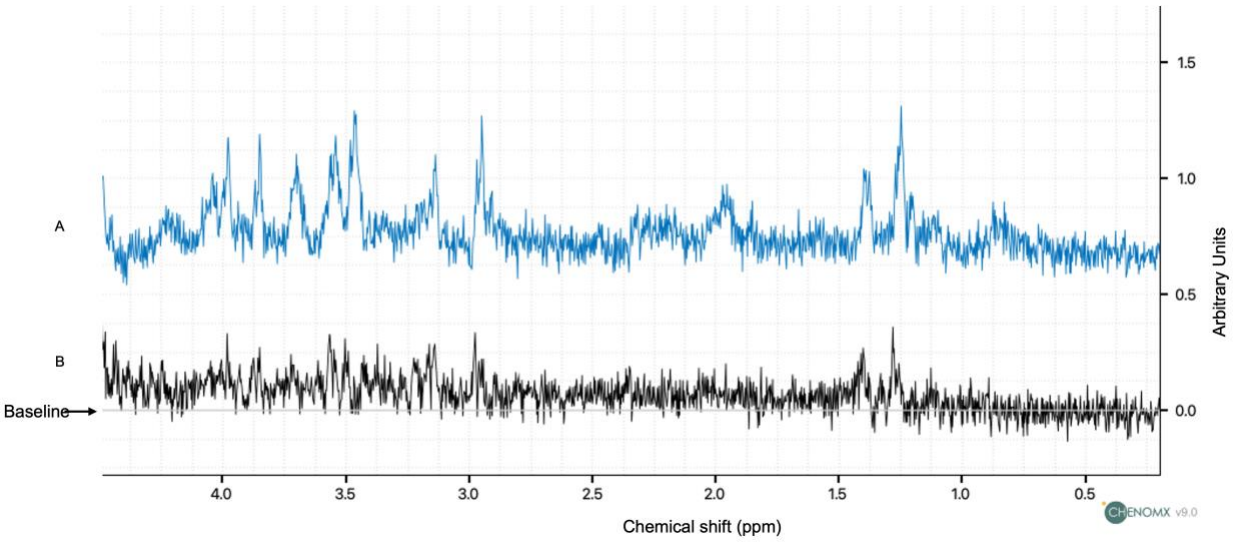

Figure 3.4 ^{1}H-MRS data acquired for GL26 cells with different TE and TR. Spectrum for cells with (A) TE / TR of 16.17 / 2500, and (B) TE / TR of 68 / 1500 is shown in blue and black respectively. Black arrow represents the baseline. TE, Echo Time; TR, Repetition Time.

^{1}H-MRS spectra acquired for glioma cell lines (GL26, U87 and C6) with 1024 averages are represented in **Figure 3.5**. Signals were detected from lipids (1), lactate (2), N-acetyl

aspartate (3), creatine (4, 9), total choline (5), inositol (6, 7, 10) and glutamine/glutamate (8) in all three glioma cell lines. The parameters used for acquiring the spectra was kept constant. Signal intensities were higher for choline containing compounds (5) and glutamine/glutamate (8) in U87 cell line compared to GL26 and C6 cell lines. Signals from choline, phosphocholine, and glycerophosphocholine were resolved for C6 cells. The signal of inositol was highest in C6 cell lines, whereas the signal from creatine remained relatively constant in all cell lines.

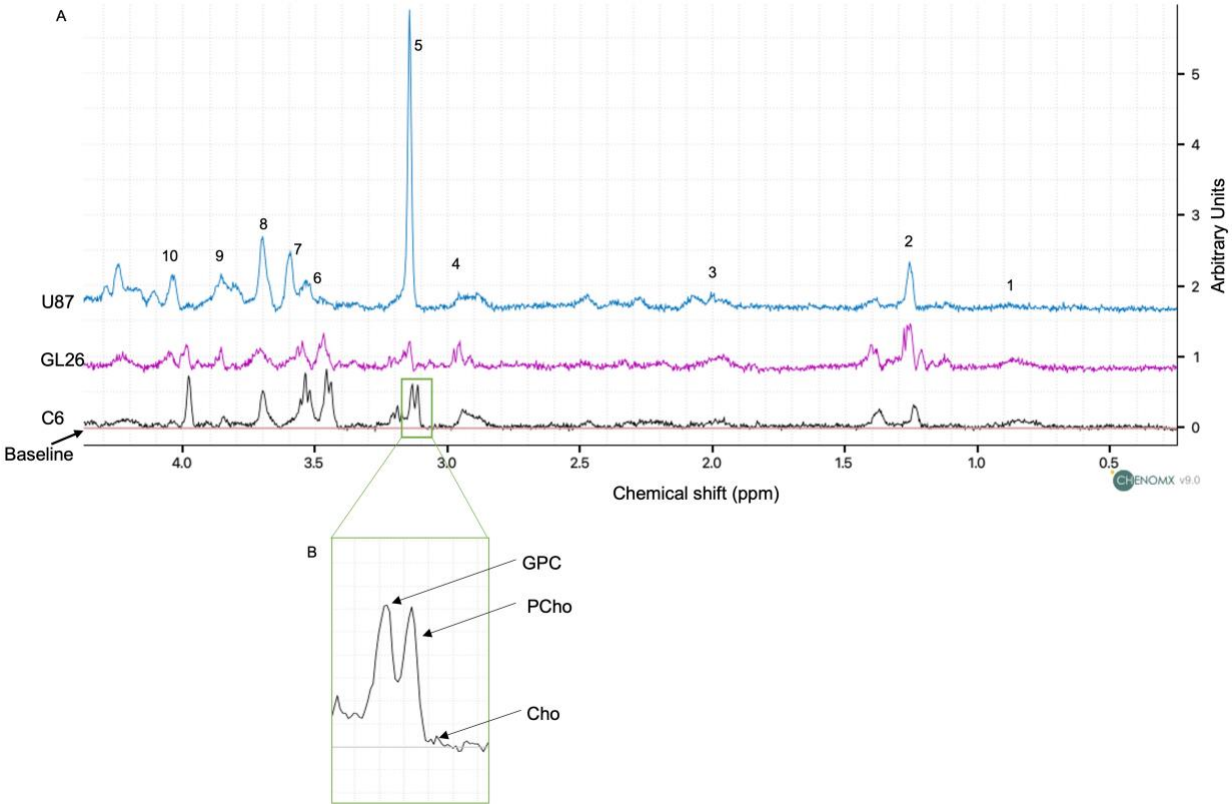

Figure 3.5 High-resolution ^{1}H-MRS spectra for glioma cell lines acquired at 14.1 T. (A) Spectra for U87 cells, GL26 cells, and C6 cells are shown in blue, pink, and black, respectively. Signals from lipid and lactate (1-2), N-acetyl aspartate (3), creatine (4, 9), total choline (5), inositol (6, 7, 10), glutamine/glutamate (8) are shown. (B) The green box shows the enlarged peaks for total choline for C6 cells. GPC, glycerophosphocholine; PCho, phosphocholine; Cho, choline respectively.

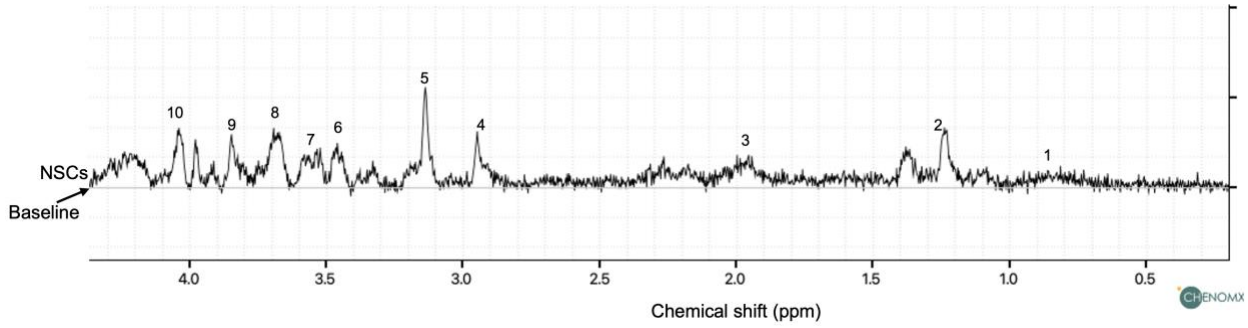

Figure 3.6 ^{1}H-MRS for NSC cells. Signals from lipid and lactate (1-2), N-acetyl aspartate (3), creatine (4, 9), total choline (5), inositol (6, 7, 10), glutamine/glutamate (8) are shown. Black arrow represents the baseline.

NSC cell line (non-cancerous cell line) was used to obtain another set of data for relative comparison shown in **Figure 3.6**. The signal from creatine was higher for NSCs compared to glioma cells.

3.3.2 ^{1}H-MRS of excised KPC tumors

An example of a 10 mm NMR tube with the pancreatic tumor excised from C57BL/6 mice is shown in **Figure 3.7 (A).** T2 RARE images (axial, sagittal and coronal) acquired for tumor samples were used as a reference for voxel placement for MRS studies as shown in **Figure 3.7 (B-C)**.

Figure 3.8 represents *ex vivo* proton MRS data acquired for excised orthotopic pancreatic tumors from C57BL/6 mice. The data acquired for excised KPC tumor from mouse #2 treated with mild hyperthermia is shown in black (KPC 2) and the untreated excised tumor from mouse #1 (Sham) is shown in green (KPC 1). Signals from metabolites lactate and lipids (1, 2), creatine (3), total choline (4), inositol (5) were detected. In KPC 2 (hyperthermia treated sample) the signal from creatine was much lower compared to KPC 1. The signal from inositol was also less prominent in KPC 2.

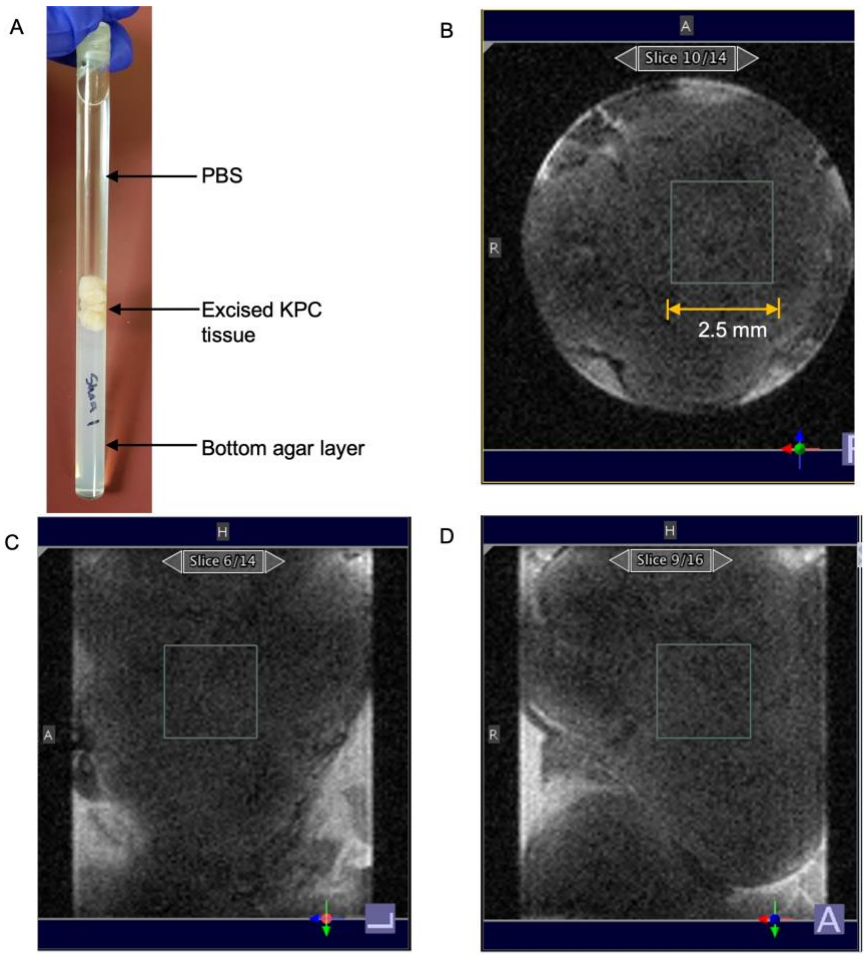

Figure 3.7 Experimental set-up for ^{1}H-MRS of excised pancreatic tumor tissue. (A) 10 mm NMR tube showing KPC tumor immersed in PBS. T2 RARE axial (B), sagittal (C), and coronal (D) images showing voxel positioning in KPC cell pellet. Voxel size was 2.5 mm isotropic (B). TE = 30 ms and TR = 1500 ms.

Ex vivo T2 RARE images of thigh muscle from a C57BL/6 mouse are shown in **Figure 3.9**. Axial, sagittal, and coronal images show a 2.5 mm isotropic voxel used for acquiring proton MRS spectrum. The representative spectrum is shown in **Figure 3.9 (D)**. Only a few metabolites (Total choline and lactate) were visualized for the thigh muscle.

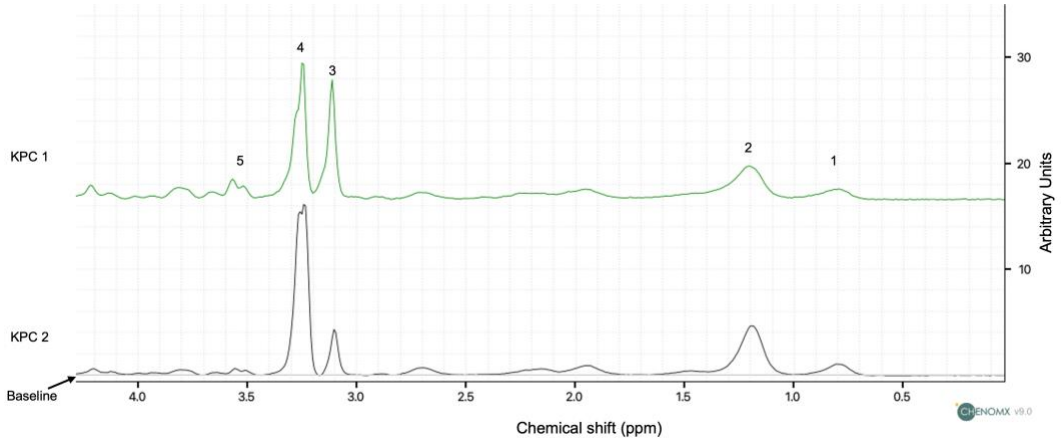

Figure 3.8 *Ex vivo* ^{1}H-MRS spectra for pancreatic tumors excised from C57BL/6 mice. KPC 2 (black) is the spectrum acquired for excised tumor from KPC mice treated with mild hyperthermia and KPC 1 (green) is the spectrum acquired for excised tumor from KPC mice that was not treated. Signals were detected from lactate and lipids (1, 2), creatine (3), total choline (4), inositol (5).

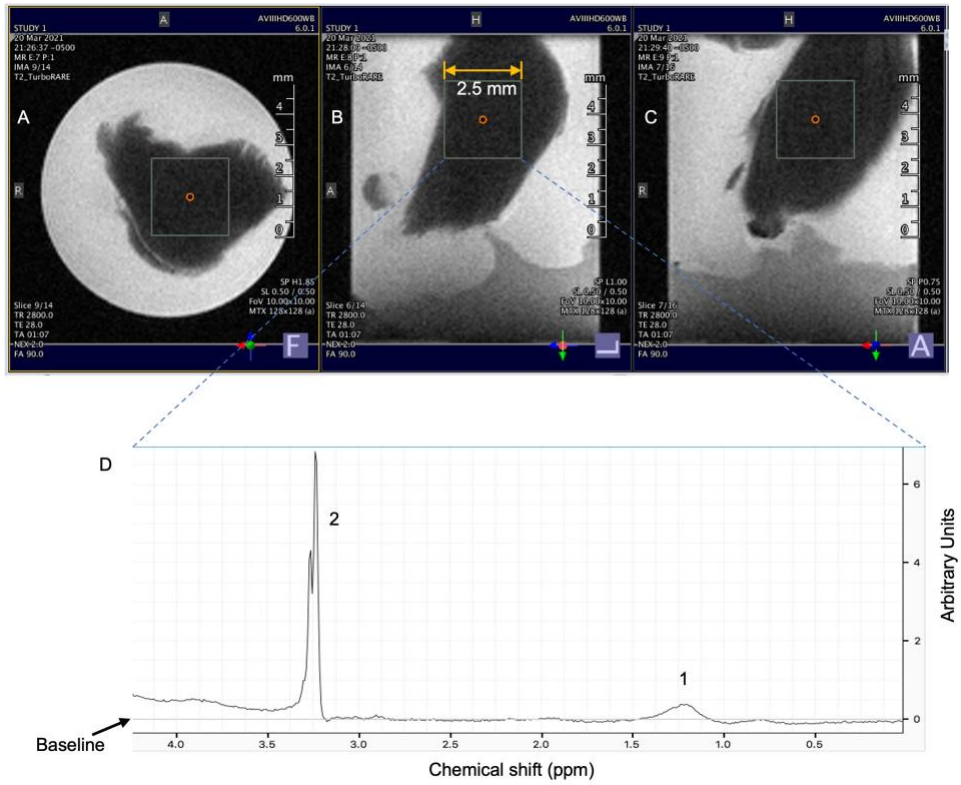

Figure 3.9 T2 RARE images of a thigh muscle excised from C57BL/6 mouse and representative ^{1}H-MRS spectrum. Axial (A), sagittal (B) and coronal (C) T2 RARE images with TE 28 ms and TR 2800 ms are shown with a 2.5 mm isotropic voxel. Representative spectrum (D) shows signal from lactate (1) and total choline (2).

3.3.3 ^{1}H-MRS of human glioblastoma samples

T2 RARE images of a glioblastoma sample (Sample #1) excised from a human subject are shown in **Figure 3.10 (A-C)**. A 2 mm isotropic voxel was selected to acquire the spectroscopy data. Phosphate buffered saline (PBS) appear bright and the tumor tissues appear dark in the RARE images. ^{1}H-MRS data acquired for Sample #1 with different echo times of 30 ms (blue), 68 ms (green), and 125 ms (black) is shown in **Figure 2.2 A**. Signals were detected from lactate (lac), N-acetyl aspartate (NAA), creatine (Cr), total choline (Tcho), and inositol (Ins). TE of 30 ms resulted in visualization of most peaks, along with resolving the characteristic doublet resonance for lactate. Similar results were observed for Sample #2 with different echo times as shown in **Figure 6.16**. ^{1}H-MRS data acquired for Sample #1 with and without VAPOR water suppression is shown in **Figure 6.15.** A huge water peak is visible without the application of water suppression pulses.

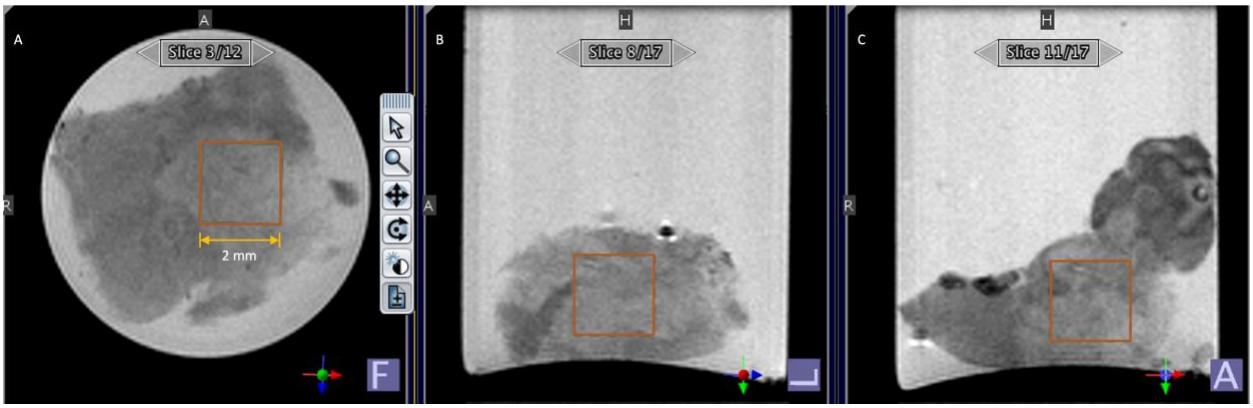

Figure 3.10 *Ex vivo* T2 RARE images of a glioblastoma sample excised from a human subject. Voxel size (shown in orange) was 2 mm isotropic. Bright signal represents PBS (phosphate buffered saline), and dark signal is for tumor. A, B and C are axial, sagittal, and coronal images respectively.

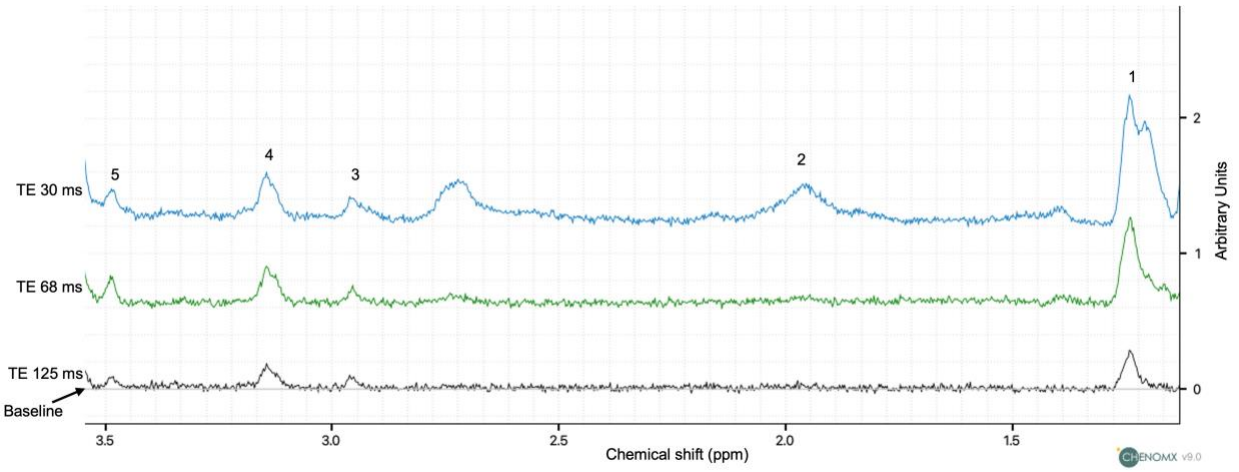

Figure 3.11 ^{1}H-MRS acquired with different TEs for glioblastoma sample excised from a human subject. Varying TEs of 30 ms (blue), 68 ms (green) and 125 ms (black) were used. Signals were detected from lactate (1), N-acetyl aspartate (2), creatine (3), total choline (4), and inositol (5). TE, echo time.

A comparison of ^{1}H-MRS data acquired for two samples of glioblastoma excised from two human subjects are shown in **Figure 3.12**. A TE of 30 ms and a TR of 1500 ms was used to acquire the spectra. The metabolite peaks of lactate and choline for sample 1 (green) is elevated compared to sample 2 (black), suggesting a pattern for increasing grade of malignancy.

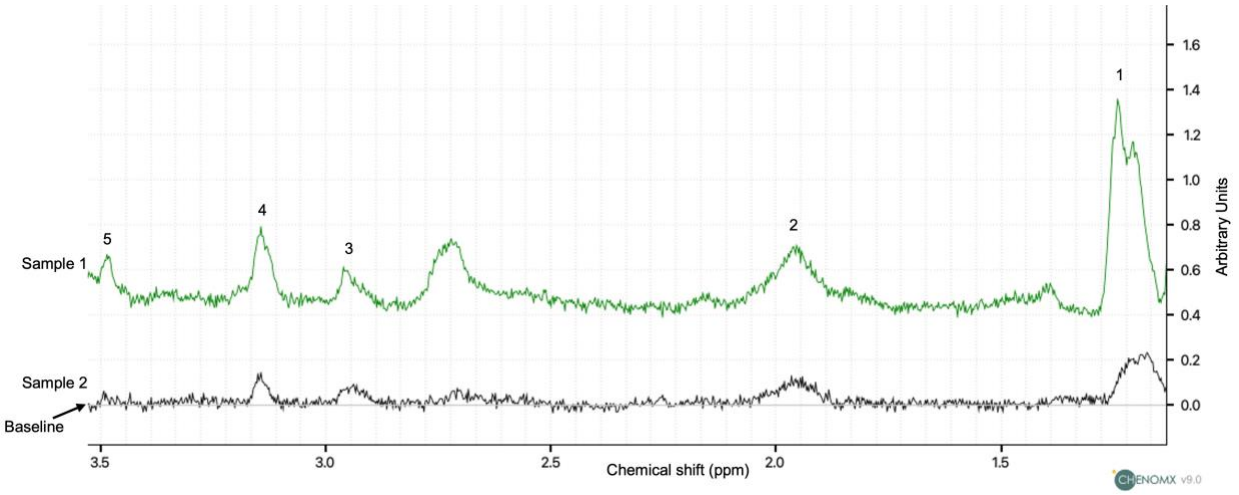

Figure 3.12 ^{1}H-MRS data acquired for two glioblastoma samples excised from human subjects. Spectra for sample 1 and sample 2 are shown in green and black respectively. Signals were detected from lactate (1), N-acetyl aspartate (2), creatine (3), total choline (4), and inositol (5).

3.4 Discussion

In the current study, proton MRS was acquired for glioma cell lines and solid glioblastoma tissues excised from human subjects. Gliomas are infiltrative lesions with heterogenous patterns, which begin in the glial cells of the brain and make up most of the common primary brain tumors in adults. Grade IV gliomas are called glioblastoma multiforme, and they are the most aggressive and malignant of all brain tumors. The median survival rate for people suffering from glioma is very low, even when they are treated with the current standard care.[8] Multi voxel ^{1}H-MRSI studies have shown potential in understanding the spatial variations of metabolites in glioma patients.[9,10] However, MRSI studies have low SNR and suffer from insufficient water and lipid suppression due to having to cover a larger region of interest. In contrast, single voxel MRS studies have advantages of better SNR with higher sensitivity and specificity.

The purpose of this study was to explore the feasibility of the ^{1}H-MRS experiments in cell lines and solid tumors. Clinical scanners make use of low field strengths like 1.5 T and 3T, resulting in low spectral resolution. With an ultra-high-field magnet ($\geq$ 7 T), higher spectral resolutions can be acquired. This study makes use of a 14.1 T magnet to acquire MRS information from voxel sizes up to 2 mm isotropic. With technical considerations, it is possible to acquire high spectral resolutions from even the smallest voxel. In this study, scan shim and local shims were performed before acquiring the MRS data. Voxel specific shim adjustments improved the homogeneity within the voxel. Outer volume suppression (OVS) helped in minimizing the large lipid signals from outside the region of interest. More importantly, VAPOR water suppression was applied in all MRS experiments to measure the metabolites clearly without the effects of a broad water peak. The concentration of the metabolites (mM range) is

very low compared to water (Molar range). However, studying these metabolites is crucial in understanding the chemical alterations in different pathological conditions. Some of the major metabolites identified in the study are discussed here.

N-acetyl aspartate (NAA) is a neuronal marker, formed from acetate and acetyl-coenzyme A. The decrease in its level is associated with damage or loss of neurons by a disease process.[11] NAA peak is the highest peak in normal brain and the acetyl moiety of NAA shows up at 2.01 ppm.

Myoinositol (mI), a simple sugar, shows up at 3.5 ppm and is a glial marker since it is synthesized in the brain's glial cells. An increase in its level is associated with the proliferation of glial cells, which can be seen in conditions like malignant tumors and Alzheimer's.[12] It is also a product of myelin degradation. In ^{1}H-MRS studies of cell lines, the signals for mI were prominent in all three glioma cell lines, whereas KPC cell line showed lower levels of mI. Moreover, mI signal was slightly higher in untreated excised KPC tumor compared to the KPC tumor treated with mild hyperthermia.

Total creatine (Cr), which comprises of creatine and phosphocreatine, is a marker for energy metabolism. Both creatine and phosphocreatine show up at 3.0 ppm and cannot be resolved even with high field magnets. It is usually taken as a reference level since it stays relatively constant even during disease processes. However, decreased levels of Cr have been observed in high-grade gliomas.[13] *Ex vivo* MRS studies of KPC tumors showed significant decrease in Cr levels for tumor treated with hyperthermia compared to untreated tumor. These results support recent studies suggesting the promoting effects of Cr on pancreatic cancer metastasis.[14] Furthermore, it shows the therapeutic effect of mild hyperthermia and its specificity on orthotopic pancreatic cancer of mouse models.

Glutamate and glutamine (Gln/Glu) show overlapping peaks at 2.35 and 3.75 ppm, so they are generally measured together as a composite peak. The peaks of Gln/Glu are hard to detect in lower magnetic field strengths like 1.5 T. Both glutamate and glutamine are essential in brain metabolism, where glutamate is an excitatory neurotransmitter.[11,15] Due of their critical roles in brain function, there is an increasing interest in understanding the role of Gln/Glu in tumor metabolism and tumor microenvironment. Our studies have shown that with short TE times, Gln/Glu can be detected in cell lines using an ultra-high-field MRI (**Figure 3.5 - 3.6**). However, spectral editing tools are required to discriminate their resonances.

Choline (Cho), which appears at 3.2 ppm, is considered a marker of membrane activity because the breakdown of the myelin membrane results in the release of phosphocholines, and it is elevated during malignant processes. Previous MRS studies have shown elevated levels of choline-containing compounds in cancer cells. [16,17] Low resolution ^{1}H-MRS usually show one overlapping signal of total choline (tCho). However, our results demonstrate that with an ultra-high-field magnet, high spectral resolutions can be acquired, and signals for total choline can be distinguished. **Figure 3.5 B** shows the resolved peaks for choline (Cho), phosphocholine (PCho), and glycerophosphocholine (GPC). Structures for Cho, PCho, and GPC are shown in **Figure 3.13**.

Lactate (Lac), which is represented as a doublet at 1.3 ppm, is a marker of cell death and tissue necrosis.[11] It is hard to detect lactate in normal conditions due to its low concentration. However, the level of lactate increases in pathological conditions, which can be easily detected. Significant increase in lactate signal was observed for excised glioblastoma sample 1 compared to sample 2 suggesting higher tumor grade for sample 1.

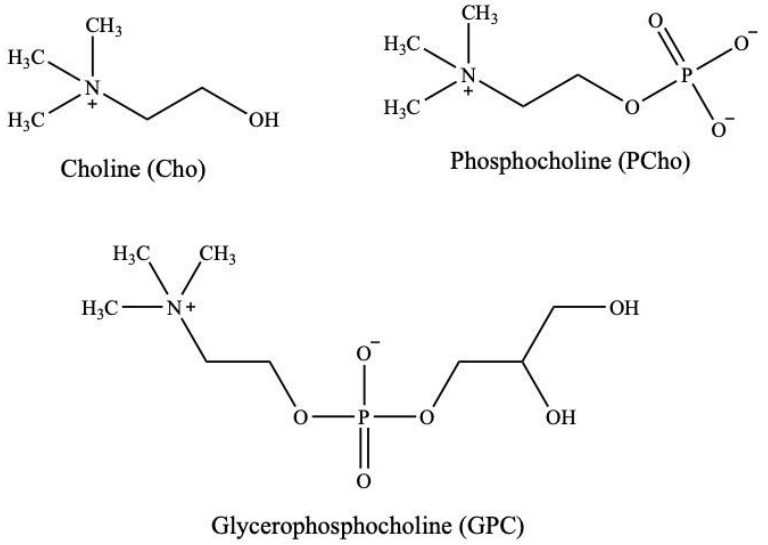

Figure 3.13 Choline containing compounds. The signal for total choline is comprised of choline, phosphocholine and glycerophosphocholine.

Detection of metabolites is dependent on the TE used during the study, which is based on the T2 relaxation time. In the study, localized spectroscopy was performed using a PRESS sequence. A PRESS sequence with TE/TR of 16.17 / 2500 was found suitable compared to a TE/TR of 68 / 1500 to acquire maximum number of metabolites for *in vitro* MRS studies of cell lines. Similar was the case for MRS studies of *ex vivo* tissues of pancreatic tumor acquired from C57BL/6 mice. For *ex vivo* MRS analysis of human glioblastoma tissues, a TE of 30 ms was found best compared to TE of 68 ms and 125 ms. Short TE MRS showed promising results with higher signal intensities in all *in vitro* and *ex vivo* MRS experiments in this study.

3.5 Conclusion

MRI guided ^{1}H-MRS experiments of cell lines and excised tissues were investigated in this study. A PRESS sequence was utilized for localization and short, intermediate, and long TE were evaluated. With an ultra-high field magnet, major metabolite peaks were detected at short TE. It is important to maintain B_0 homogeneity during all MRS experiments to improve the

spectral resolution. In this study, shimming was performed prior to all MRS experiments. Water suppression pulses and outer volume suppression helped in better visualization of the metabolite peaks. Chenomx software was used to process the spectra post-acquisition. Phase correction and baseline correction were performed to make phase adjustments and to correct asymmetric baselines.

In vitro MRS studies of KPC cells demonstrated that passage number can influence the spectral information. The signal for metabolites decreases with increasing passage number. MRS studies of GL26 cell line with short TE showed high-resolution spectrum even with 256 averages in 10 mins 40 sec. This demonstrates the feasibility of acquiring high-resolution ^{1}H-MRS from small voxels up to 2 x 2 x 2 mm^3 in a short period. ^{1}H-MRS was also helpful in detecting metabolite changes in hyperthermia treated and untreated tumor tissues excised from C57BL/6 mice. Furthermore, MRS studies of glioblastoma tissues excised from human subjects may help in understanding and predicting tumor grade. Specific biomarkers can also be identified using ^{1}H-MRS techniques with the optimization of TE and TRs. The next steps for this project include quantitative analysis of the spectra using different software and external standards. It is important to perform MRS studies on mouse models to better understand the challenges with *in vivo* MRS studies.

3.6 References

1. Meisamy S, Bolan PJ, Baker EH, et al. Adding *in vivo* quantitative 1H MR spectroscopy to improve diagnostic accuracy of breast MR imaging: preliminary results of observer performance study at 4.0 T. *Radiology*. 2005;236(2):465-475. doi:10.1148/RADIOL.2362040836

2. Kurhanewicz J, Vigneron DB, Hricak H, Narayan P, Carroll P, Nelson SJ. Three-dimensional H-1 MR spectroscopic imaging of the in situ human prostate with high (0.24-0.7 cm3) spatial resolution. *https://doi.org/101148/radiology19838628874*. 1996;198(3):795-805. doi:10.1148/RADIOLOGY.198.3.8628874

3. Howe FA, Barton SJ, Cudlip SA, et al. Metabolic profiles of human brain tumors using quantitative *in vivo* 1H magnetic resonance spectroscopy. *Magn Reson Med*. 2003;49(2):223-232. doi:10.1002/MRM.10367

4. Jacobs MA, Barker PB, Bottomley PA, Bhujwalla Z, Bluemke DA. Proton magnetic resonance spectroscopic imaging of human breast cancer: a preliminary study. *J Magn Reson Imaging*. 2004;19(1):68-75. doi:10.1002/JMRI.10427

5. García-Figueiras R, Baleato-González S, Padhani AR, et al. Proton magnetic resonance spectroscopy in oncology: the fingerprints of cancer? *Diagnostic and Interventional Radiology*. 2016;22(1):75. doi:10.5152/DIR.2015.15009

6. Zhu H, Barker PB. MR Spectroscopy and Spectroscopic Imaging of the Brain. *Methods Mol Biol*. 2011;711:203.

7. Yushkevich PA, Piven J, Hazlett HC, et al. User-guided 3D active contour segmentation of anatomical structures: significantly improved efficiency and reliability. *Neuroimage*. 2006;31(3):1116-1128. doi:10.1016/J.NEUROIMAGE.2006.01.015

8. Survival Rates for Selected Adult Brain and Spinal Cord Tumors. Accessed July 1, 2022. https://www.cancer.org/cancer/brain-spinal-cord-tumors-adults/detection-diagnosis-staging/survival-rates.html

9. Li Y, Lafontaine M, Chang S, Nelson SJ. Comparison between Short and Long Echo Time Magnetic Resonance Spectroscopic Imaging at 3T and 7T for Evaluating Brain Metabolites in Patients with Glioma. *ACS Chem Neurosci*. 2018;9(1):130-137.

10. Laino ME, Young R, Beal K, et al. Magnetic resonance spectroscopic imaging in gliomas: clinical diagnosis and radiotherapy planning. *BJR Open*. 2020;2(1):20190026. doi:10.1259/BJRO.20190026

11. Scheau C, Preda EM, Popa GA, Ghergus AE, Capsa RA, Lupescu IG. Magnetic Resonance Spectroscopy – a non-invasive method in evaluating focal and diffuse central nervous system disease. *Journal of Medicine and Life*. 2012;5(4):423. Accessed July 2, 2022. /pmc/articles/PMC3539838/

12. Shonk TK, Moats RA, Gifford P, et al. Probable Alzheimer disease: diagnosis with proton MR spectroscopy. *Radiology*. 1995;195(1):65-72. doi:10.1148/RADIOLOGY.195.1.7892497

13. Lowry OH, Berger SJ, Chi MM -Y, Carter JG, Blackshaw A, Outlaw W. Diversity of metabolic patterns in human brain tumors--I. High energy phosphate compounds and basic composition. *J Neurochem*. 1977;29(6):959-977. doi:10.1111/J.1471-4159.1977.TB06500.X

14. Zhang L, Bu P. The two sides of creatine in cancer. *Trends in Cell Biology*. 2022;32(5):380-390. doi:10.1016/J.TCB.2021.11.004

15. Swanberg KM, Landheer K, Pitt D, Juchem C. Quantifying the Metabolic Signature of Multiple Sclerosis by *in vivo* Proton Magnetic Resonance Spectroscopy: Current Challenges and Future Outlook in the Translation from Proton Signal to Diagnostic Biomarker. *Frontiers in Neurology*. 2019;10:1173. doi:10.3389/FNEUR.2019.01173/BIBTEX

16. Glunde K, Bhujwalla ZM, Ronen SM. Choline metabolism in malignant transformation. *Nat Rev Cancer*. 2011;11(12):835-848. doi:10.1038/NRC3162

17. Penet MF, Shah T, Bharti S, et al. Metabolic imaging of pancreatic ductal adenocarcinoma detects altered choline metabolism. *Clinical Cancer Research*. 2015;21(2):386-395.

Chapter 4 - Increased volumes of lobule VI in a valproic acid model of autism are associated with worse set-shifting performance in male Long-Evan rats[1,2]

4.1 Abstract

Autism spectrum disorder (ASD) is a neurodevelopmental disorder with a skewed sex-based diagnostic ratio. While males are at a higher risk for ASD, it is critical to understand the neurobiology of the disorder to develop better treatments for both males and females. Our prior work has demonstrated that VPA (valproic acid) treated offspring had impaired performance on an attentional set-shifting task. The current study used MRI and regions of interest analyses to measure the volumes of cerebellar subregions in VPA and controls rats that had participated in the attentional set-shifting task. VPA males had significantly more volume in lobule VI compared to male controls. VPA female rats had significantly less volume in lobules I, IV and X compared to female controls. In addition, it was revealed that decreases in volume for VPA females was associated with worse performance. Males with increases in lobule VI were also impaired on the set-shifting task. Similar volumetric differences within the cerebellum have been observed in humans with ASD, which suggests that the VPA model is capturing some of the same brain changes observed in humans with ASD, and that these changes in volume may be impacting cognition.

[1]Reprinted with permission from Payne, M., Mali, I., McKinnell, Z. E., Vangsness, L., Shrestha, T. B., Bossmann, S. H., & Plakke, B. (2021). Increased volumes of lobule VI in a valproic acid model of autism are associated with worse set-shifting performance in male Long-Evan rats. *Brain Research, 1765*, 147495.

[2]As a second co-author, my contributions to this project are sample preparation for imaging, MRI acquisition and analysis, and image segmentation using ITK-Snap software.

4.2 Introduction

Autism spectrum disorder (ASD) is characterized by deficits in social interactions, communication, and increases in repetitive behavior. Another common symptom of ASD is problems with executive functions.[1–4] The neurobiology of ASD is not well understood, however there are consistently alterations within the cerebellum in humans with ASD[5–8] and in animal models of ASD[9–12]. Recent human studies have examined the volume of cerebellar lobules and found that decreases in volume correlate to increased ASD symptomology.[5] In addition, it has been suggested that the cerebellum assists with cognitive regulation through its connections via the thalamus to the prefrontal cortices.[13–15] Human imaging studies have also found that cerebellar activation occurs for a wide array of cognitive tasks including working memory, language, and executive functions.[14,16–18] Rodent models have provided evidence of functional connectivity between posterior regions of the cerebellum and frontal cortices.[19] Evidence from human and animal studies suggests that the cerebellum may play a role in cognitive functions.

The current study used the valproic acid (VPA) model of ASD in rodents. The VPA model was created when it was documented that pregnant women, prescribed medications containing VPA, had children that developed ASD at a higher rate than the regular population.[20–22] The VPA models has both construct and face validity[23], where VPA animals display altered social interactions.[24] In addition, VPA exposure leads to a less skewed sex ratio for development of ASD, where it occurs more often in both males and females.[25,26] The mechanisms of VPA exposure leading to ASD symptoms are still being investigated, but VPA exposure can cause hyperacetylation in the embryonic brain[27] and this can lead to loss of neurons in development.[23] Other possible mechanisms include excitatory and inhibitory imbalances related to altered GABA function[28], changes in fatty acid synthase expression[9] and changes in gene expression.[29]

Even though ASD is linked to several genes, 40–50% the variance of ASD is driven by environmental factors[30–32], therefore the VPA model is an important model to use in conjunction with knockout models.

The current study measured grey matter volumes using MRI (magnetic resonance imaging) with 3D scans of the entire cerebellum of VPA and control animals. Past research has indicated that VPA animals lose purkinje cells and that this could contribute to loss of cerebellar volume.[11,33–35] A recent MRI study indicated that loss of volume of vermis regions VI and VII were correlated with loss of Purkinje neurons in VPA rats.[35] One goal of the current study was to measure across many lobules to better understand how cerebellar volume may differ between anterior and posterior regions in both male and female rats. It was hypothesized that vermis lobules VI and VII, would be decreased in volume for VPA animals compared to controls. This study is unique in that 3D scans at high-resolution allowed accurate segmentation across individual lobules of the cerebellum to uncover differences between groups and to better understand sex differences within the VPA model.

For the current study, the behavioral data was published[36], but a brief overview of the set-shifting task is as follows. Rats were trained to dig in different media types with various scented flowerpots. The digging media and the odors are cues that inform the rat where to dig for reward. After reaching criterion on one rule, the rule is changed, and rats must learn to dig to the newly rewarded cue. A switch within a category (i.e., odor 1 vs 2 to odor 3 vs 4) is an intra-dimensional shift (IDS), the rat learns new odors, but it is the same rule, follow your nose. A switch between categories (i.e., odor 1 vs odor 2 to media 1 vs media 2) is an extra-dimensional shift (EDS), as now the rat ignores the odor cues and attends to the digging media, see Table 1 for an example of the pairings for one rat. This task assesses the ability of an animal to learn a rule and change their

behavior when the rule is changed. Accurate set-shifting performance relies on a network of frontal regions[37–39], but recent research suggests the cerebellum may also modulate cognitive function via its connections to the frontal cortices.[14,15,18] Our prior results found a main impairment of VPA rats compared to controls on the IDS phase of the task.[36] VPA rats completed more trials to reach criterion and made more error trials. One hypothesis related to the behavioral data was to examine if lobules impacted by VPA exposure were related to task performance. The relationship between overall task performance as measured by total trials completed across all phases of the task and the specific task phases (i.e., IDS) and cerebellar volumes impacted by VPA exposure were examined. It was predicted that for VPA rats that decreases in crus I would decrease performance accuracy on the behavioral task.

Table 1 When the rat reaches a criterion of 6 correct trials in a row it moves to the next phase. The task phases are simple discrimination (SD), compound discrimination (CD), intra-dimensional shift (IDS), Reversal 1 (R1), extra-dimensional shift (EDS) and Reversal 2 (R2). * Indicates the rewarded pot and correct choice for that trial. Note that for each phase there is another set of pots so that all combinations occur. For example, in the CD (manilla folders/ anise v. shredded paper/ cinnamon) would be offered on different trials.

Phase	SD	CD	IDS	R1	EDS	R2
Example Rat	Manilla folder* v. Aspen	Manilla folder*/Cinnamon v. Shredded paper/Anise	Foam rubber*/Rum v. Felt/ Vanilla	Felt*/Rum v. Foam Rubber/ Vanilla	Lemon*/ Burlap v. Almond/ Ribbon	Almond*/Burlap v. Lemon/ Ribbon

4.3 Results

Sixteen pregnant dams were injected (11 VPA, 5 saline), 2 dams did not deliver. There were 25 male control pups weaned and 23 female controls weaned. There were 29 VPA male pups weaned and 29 female pups, after weaning 7 VPA rats were lost to sickness. Seventy adult rats completed the set-shifting task and were imaged in the MRI. All cerebellums were imaged

but some images were not analyzable due to scanner artifacts or poor placement of tissue in the scanner, determined by a blind to condition reviewer, this excluded 1 female control, 6 male control, 5 female VPA, and 2 male VPA brains. This left 56 brains that were segmented for cerebellar volume (16 female control, 13 male control, 8 female VPA, and 19 male VPA for all regression and MRI analyses). Each lobule was color-coded. For lobules I-IV, IX and X vermis was included with entire portion of the lobule, Fig. 4.1. For lobules V, VII and VIII the vermis was separated from the left and right sides of the lobule, each coded into 3 segments (vermis, left, right). Crus I and Crus II were separated into left and right hemispheres. Segmentation was then screened for consistency through a 3-D modeling in ITK-SNAP before evaluation of total volume.

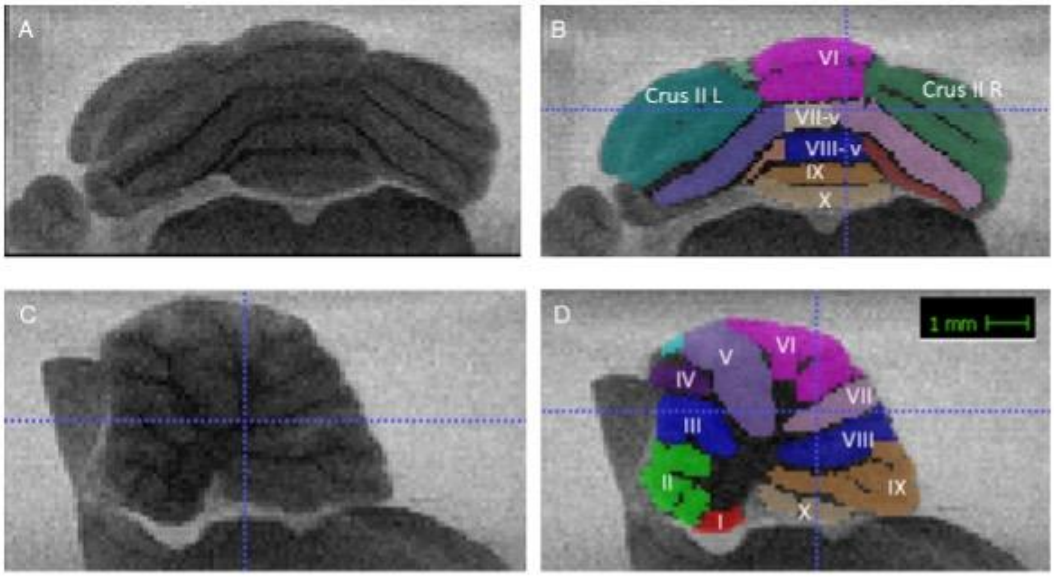

Figure 4.1 A and B are coronal sections outlining the areas of interest measured − 12.84 mm from bregma. C and D are sagittal views showing the same ROIs, 1.13 mm lateral.

The multi-level gamma regression had a sex effect, (B = 0.04, *SE* = 0.003, *t* = 11.69, *p* < .001; Fig. 4.2) and a condition difference (B_{diff} = -0.02, *SE* = 0.01, *t* = -2.21, *p* = .03; Fig. 4.3).

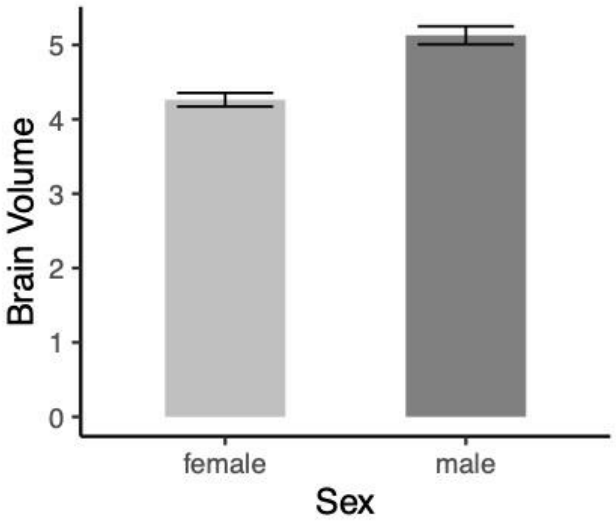

Figure 4.2 Sex differences in total cerebellar volume (mm^3). Error bars represent ± 1SE. Females had significantly smaller cerebellar volumes compared to male rats.

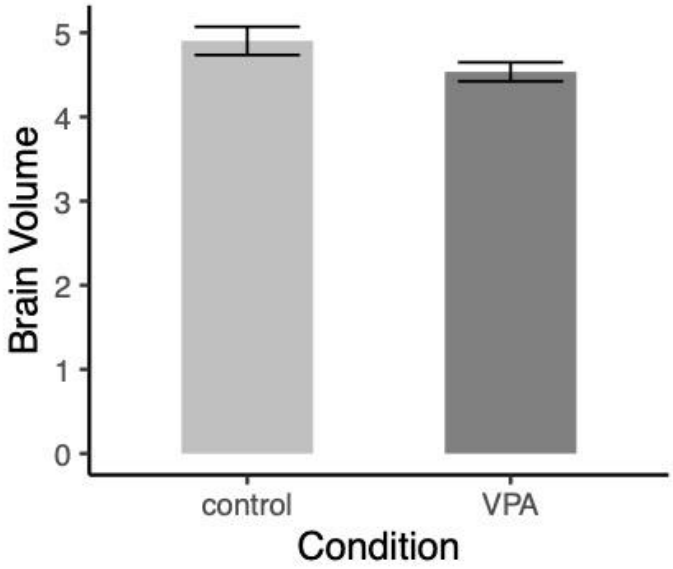

Figure 4.3 Condition differences in total cerebellar volume (mm^3). Error bars represent ±1SE. VPA rats had smaller cerebellar volumes than control rats.

These outcomes were driven by female VPA rats which had smaller cerebellar volumes than did their control counterparts (B_{diff} = -0.04, *SE* = 0.01, *z* = -4.14, *p* < .001); whereas this decrease was not present among male rats (B_{diff} = 0.002, *SE* = 0.01, *z* = 0.22, *p* = .99), Fig. 4.4.

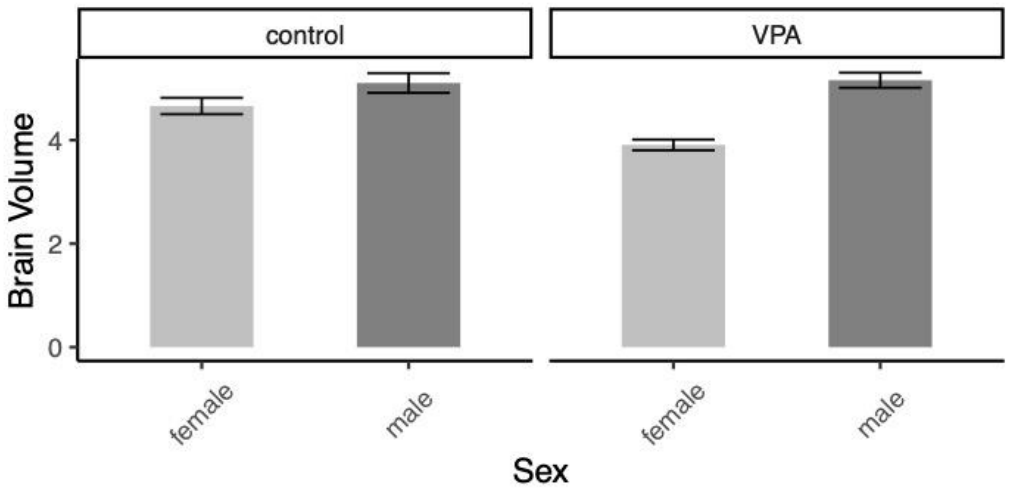

Figure 4.4 The female VPA rats had the smallest overall cerebellar volume (mm^3) compared to female control rats. Error bars represent ± 1SE.

Planned comparisons, with Tukey corrections, of specific brain regions supported these findings and indicated that VPA females had reduced cerebellar volume of lobules I, IV, and X compared to control females (Table 2 and Fig. 4.5). VPA males had increased cerebellar volume of lobule VI compared to control males (Table 3 and Fig. 4.5).

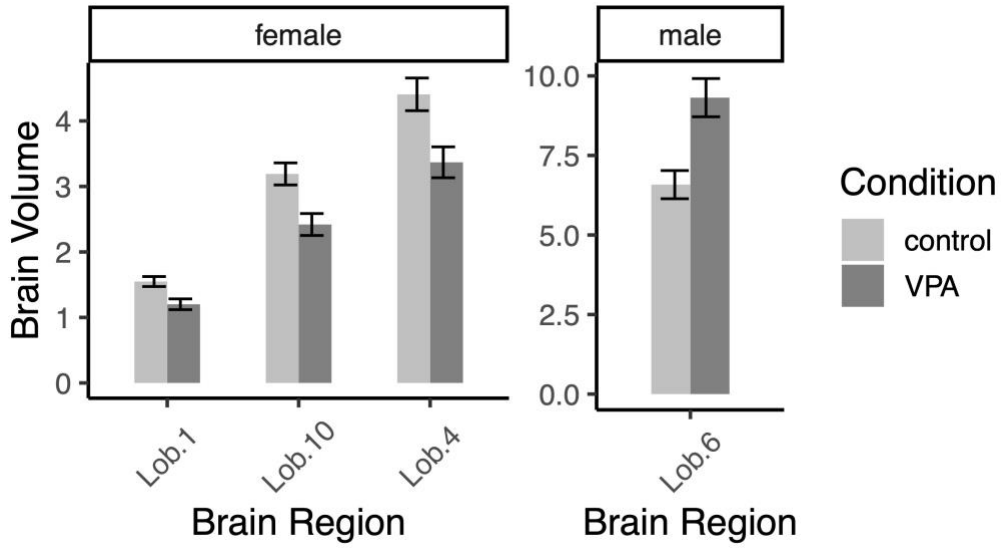

Figure 4.5 Prenatal exposure to VPA reduced cerebellar volume (mm^3) of lobules I, IV, and X in female rats and increased cerebellar volume of lobule VI in male rats. Error bars represent ±1SE.

Table 2 Planned contrasts compare female rats' regional cerebellar volume (mm^3) across control and VPA conditions.

Region	B_{diff}	SE	z	p
Crus I L	-0.03	0.01	-2.18	.13
Crus I R	-0.01	0.01	-1.11	.68
Crus II L	-0.02	0.01	-1.40	.50
Crus II R	-0.01	0.01	-1.05	.72
Lobule I	**-0.19**	**0.07**	**-2.85**	**.02**
Lobule II	-0.02	0.01	-1.50	.44
Lobule III	-0.02	0.01	-1.69	.33
Lobule IV	**-0.07**	**0.02**	**-2.86**	**.02**
Lobule V-vermis	-0.03	0.01	-2.52	.06
Lobule V L	-0.03	0.02	-1.39	.51
Lobule V R	-0.02	0.02	-0.75	.88
Lobule VI	-0.002	0.01	-0.18	.99
Lobule VII-vermis	-0.02	0.03	-0.51	.96
Lobule VII L	-0.03	0.02	-1.87	.24
Lobule VII R	-0.03	0.02	-1.78	.28
Lobule VIII-vermis	-0.04	0.02	-1.60	.38
Lobule VIII L	-0.08	0.05	-1.72	.32
Lobule VIII R	-0.08	0.04	-1.87	.24
Lobule IX	-0.02	0.01	-1.14	.66
Lobule X	**-0.10**	**0.03**	**-3.03**	**.01**

Table 3 Planned contrasts compare male rats' regional cerebellar volume (mm^3) across control and VPA conditions.

region	B_{diff}	*SE*	*z*	*p*
Crus I L	0.03	0.01	2.48	.06
Crus I R	0.02	0.01	2.16	.14
Crus II L	0.02	0.01	2.03	.18
Crus II R	0.02	0.01	1.70	.32
Lobule I	-0.06	0.04	-1.41	.49
Lobule II	-0.01	0.01	-1.01	.74
Lobule III	-0.01	0.01	-0.52	.95
Lobule IV	-0.02	0.01	-1.08	.70
Lobule V-vermis	0.01	0.01	0.57	.94
Lobule V L	-0.002	0.01	-0.14	.99
Lobule V R	-0.01	0.01	-0.88	.82
Lobule VI	**0.04**	**0.01**	**3.61**	**.001**
Lobule VII-vermis	-0.03	0.03	-1.32	.55
Lobule VII L	-0.003	0.01	-0.20	.99
Lobule VII R	-0.002	0.01	-0.19	.99
Lobule VIII-vermis	-0.02	0.02	-1.39	.51
Lobule VIII L	0.04	0.03	1.42	.49
Lobule VIII R	0.06	0.03	2.09	.16
Lobule IX	0.005	0.01	0.42	.97
Lobule X	-0.04	0.02	-1.86	.25

4.3.1 Effect of cerebellar volume and set-shifting performance

Complete behavioral results examining the set-shifting task were reported in (McKinnell et al., 2021)[36], but each phase of the task requires rats to reach criterion before moving to the next phase of the task. Therefore, the more trials required to complete the entire task the worse rats' overall performance. Total trials were used as a proxy of overall task performance. In addition, VPA rats performed the worst at the IDS phase of the task. The models examined if sex, condition, and the volume of specific cerebellar regions were predictive of behavior as measured by total trials and IDS trials. Cerebellar regions were selected based on significant differences between VPA and control groups (see prior analysis) or in the case of crus I L

because of its connections to the frontal cortices and homology with human crus region[40], this also preserved statistical power. The model included these important regions of interest for female (Lobules I, IV, and X; Crus I L) and male (Lobule VI, Crus I L) rats. These multi-level Poisson regressions included the main effects of condition and cerebellar region volume, as well as their two-way interactions. The model also nested by litter and allowed the model intercept to vary as a random effect. The condition predictor was dummy-coded, and the region predictors were means-centered to ensure that the estimate of the model's intercept represented the average cerebellar volume of rats in the control condition.

4.3.1.1 IDS trials – Male rats

The model indicated a significant interaction between Condition × Lobule VI (B = 0.18, *SE* = 0.09, *z* = 2.03, *p* = .04). VPA males with enlarged volumes of lobule VI performed worse at the IDS phase of the task compared to male controls, Fig. 4.6.

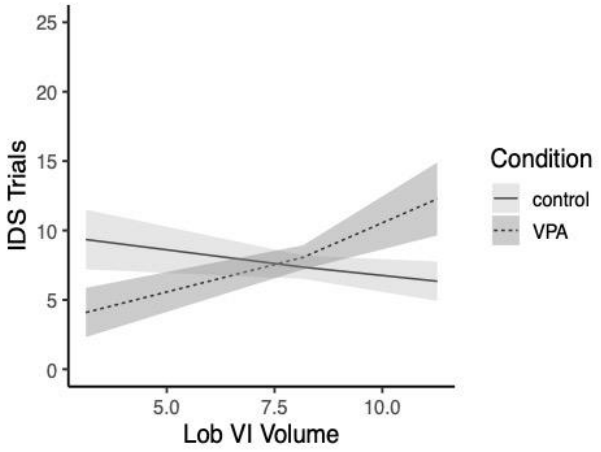

Figure 4.6 Male VPA rats with larger Lobule VI volumes (mm3) were worse at the IDS phase of the task.

For further visualization purposes trials to criterion were plotted for male rats as defined by a median split, to compare rats with larger volumes versus rats with smaller volumes. This

emphasized the observed behavioral impairment on trials to criterion for the IDS phase of the task for VPA rats with enlarged volumes, Fig. 4.7.

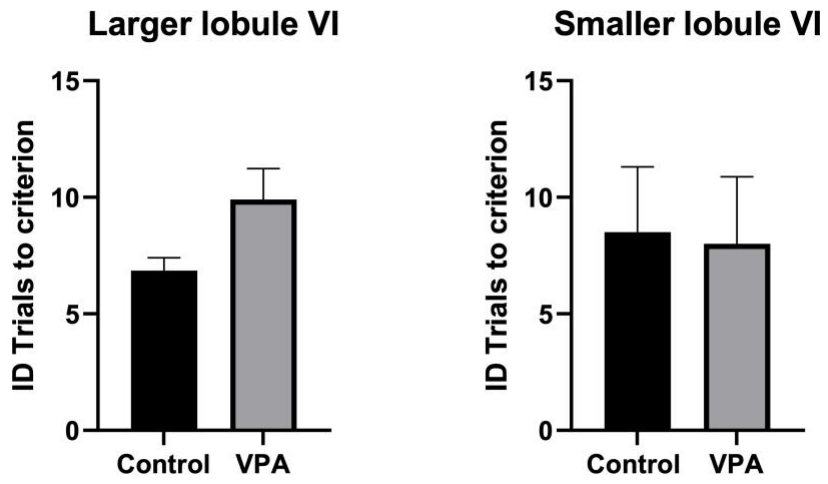

Figure 4.7 (Left panel) VPA rats with enlarged lobule VI volumes (greater than the median volume) were significantly worse compared to control rats (*p < 0.05, unpaired *t*-test). (Right panel) VPA rats with smaller volumes were not impaired on the IDS phase of the task.

4.3.1.2 Total trials – Female rats

The model indicated that condition (B = -0.34, *SE* = 0.17, *z* = -2.01, *p* = .04) and Crus I L volume (B = -0.06, *SE* = 0.03, *z* = -2.17, *p* = .03) were significant predictors of total trials in female rats. These main effects were qualified by a significant interaction (B = -0.14, *SE* = 0.05, *z* = -2.58, *p* = .01). Rats with smaller Crus I L volumes completed more total task trials, regardless of condition. At larger volumes, the VPA animals perform better than controls (Fig. 4.8), which suggests that if volumes in VPA rats could be restored it may improve cognitive performance.

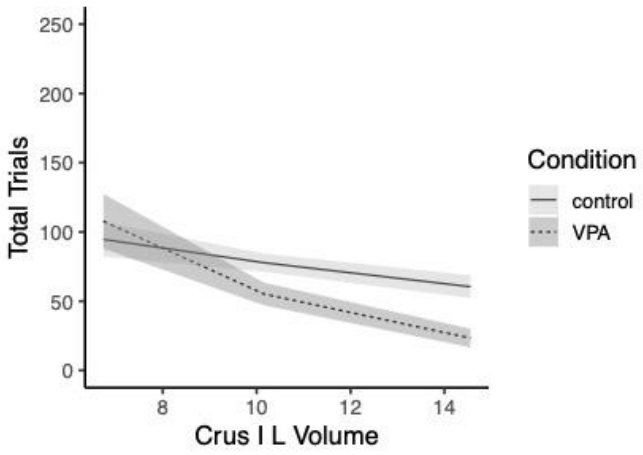

Figure 4.8 All female rats were worse across the task as measured by total trials for smaller Crus I L brain volumes (mm^3).

4.3.1.3 IDS Trials – Female Rats

The model contained one significant predictor: the Condition × Lobule X interaction. The interaction demonstrated that control rats with larger lobule X volumes were worse at the IDS phase of the task (B = -0.47, SE = 0.23, z = -2.03, p = .04; Fig 4.9).

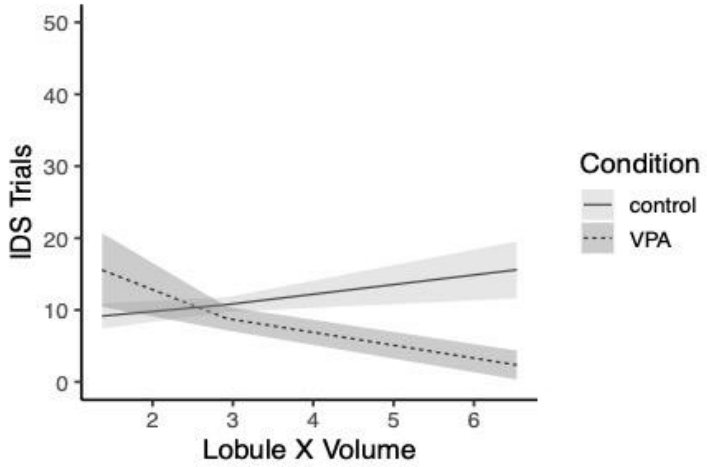

Figure 4.9 Prenatal VPA exposure was a predictor of IDS task trials in female rats at larger Lobule X brain volumes (mm^3).

4.4 Methods and materials

4.4.1 Subjects

Sixteen pregnant dams (Long-Evans) were injected on gestational day 12 with a single dose of saline or VPA (sodium valproate (Sigma), 250 mg/ml, mixed in saline, 600 mg/kg). Dams were briefly anesthetized on isoflurane gas in an induction chamber to administer a less stressful I.P. injection, required by the IACUC. This brief exposure to isoflurane is not associated with negative developmental outcomes.[41] Pups were reared with litter mates until weaning at PND 21, then were pair housed with a same-sex littermate.

4.4.2 Set-shifting task

Apparatus, stimuli and training. A Plexiglass box (50 x 37.5 x 25 cm) with a black divider was used as the testing arena. The sliding door allowed access to the flowerpots (which were held to the table with Velcro to prevent tipping). All stimuli were mixed and recycled between rats to allow any odor cues to be disseminated. After a dig (successful or unsuccessful the opposite pot was removed to prevent digging in the other flowerpot, after the first 4 discovery trials).

Adult rats were trained in the set shifting task with 6 stages (simple discrimination (SD), compound discrimination (CD), intra-dimensional shift (IDS), reversal 1 (R1), extra-dimensional shift (EDS) and reversal 2 (R2) to test cognitive flexibility. Rats underwent food restriction for between 7-10 days and then underwent training. Honey Nut Cheerios (General Mills, MN) and a flowerpot were introduced into the home cage the night before training began. Basic training consisted of shaping digging behavior. Rats were allowed to obtain cereal pieces on top of the bedding of the flowerpots. During successive trials the cereal was buried deeper until the rat was successfully digging to retrieve it at about 3.5 cm deep. Day 2 of training consisted of an odor

discrimination (tea tree oil vs lavender) with plain pine bedding, and a media discrimination (shredded paper vs pine shavings) on unscented pots. Pots themselves were not scented rather blotting paper was taped to the inner lip of the ceramic pot and scented. The paper was re-scented before every training session. Crushed Cheerio powder was applied to all digging media to prevent reward odor from serving as a digging cue. In all sessions the first four trials were discovery trials and were not scored, the rat could sample the other pot in these trials only. After these trials the undug pot was lifted out immediately after the rat initiated a dig (defined as vigorously moving the media with nose or paw). Training criteria for basic training (day 1) was 10 consecutive digs, whereas for all other training phases it was 6 consecutive trials to move to next phase of training or next phase of the task. On the day of the set shifting task the SD, CD, IDS, R1, EDS and R2 were administered. All stimuli were counterbalanced with a Latin square design and half of the rats were trained odor to media shifts, half media to odor shifts. Medias were shredded manila folders, aspen shavings, foam rubber, felt, burlap ribbon, and silk ribbon. Odors were rum, vanilla, lemon, almond, cinnamon, and anise. A pilot study demonstrated that rats could discriminate these odors. Behavioral data are reported in (McKinnell et al., 2021).[36] All procedures were approved by Kansas State University IACUC.

4.4.3 Brain processing

Adult rats were perfused, and brains were extracted. 4% Paraformaldehyde at a pH of 7.2 was used and a rate of 50mL/min for 8-10 minutes was utilized in the perfusion process. The cerebellums were removed and left in paraformaldehyde overnight then moved to a 30% sucrose solution until the brain sunk. Once sunk they were brought to the MRI for imaging. Cerebellums were placed in sucrose because they are also being processed for immunohistochemistry analysis to assess Purkinje cells, which is an ongoing project.

4.4.4 MRI Volumetric Analyses

Magnetic resonance images were obtained with a Bruker 600 MHz and a bottom loading probe. They were placed on an agar platform within an approximately 40 mm long glass tube and covered with a sucrose solution. Imaging was performed through Paravision 6.0.1 software with scan parameters: 27.52489 ms TE, 1575 TR, and a 90° flip angle for RARE imaging with a RARE factor of 16. A three-dimensional scan was obtained with a 100 μm3 voxel size, 66 slices in the axial orientation, and 150 slices for both sagittal and coronal. The field of view was limited to 15 x 15 x 6.6 mm and slices were obtained with an interlaced acquisition pattern. Segmentation was completed using the open source ITK-SNAP platform. Initially images were retrieved from the instrumentation in dicom format, then converted to NIfTI to condense data sets for easier file transfer using dcm2nii. Following the rat atlas (Paxinos, G, Watson, 2007)[42] the cerebellums was segmented according to different lobule identification in all three views. Blind to condition reviewers were trained to use anatomical landmarks and the atlas to manually segment the different lobules of the cerebellum.

4.4.5 Data analysis

4.4.5.1 Volumes and set-shifting data

Imaging data were analyzed with ITK-SNAP and all statistics were conducted in R or JMP analysis software (Statistical Discovery. From SAS, NC, USA). To determine how cerebellum volume was affected by VPA exposure multi-level gamma regressions were conducted.[43] The regression included the main effects of condition, cerebellar region, and sex as well as their higher-order interactions. Additionally, the model nested by litter and allowed the model intercept to vary as a random effect. This model structure controlled for differences in cerebellar volume being driven by litter[44,45], while still identifying sex-specific changes in

cerebellar volume due to VPA exposure. The sex, region, and condition predictors were effect coded to ensure that the estimate of the model's intercept represented the sample grand mean. Tukey-corrected planned comparisons were conducted using the emmeans package[46]; graphs were created with emmeans and ggplot2.[46,47]

4.5 Discussion

4.5.1 Male Rats

Lobule VI increases in male VPA rat volume aligns with some results found in humans with ASD.[9,48] Lobule VI also had altered functional connectivity to frontal network regions in humans with ASD.[5] In addition, lobule VI is connected to the anterior cingulate gyrus (ACC)[49] as well as infralimbic and prelimbic regions[50] and also is active during cognitive tasks such as the tower of London, which test similar executive functions.[51] In humans with ASD, the anterior cingulate is also associated with reduced cognitive control[52,53], and lobule VI is associated with working memory cognitive tasks.[54] In rodents, lesions or inactivation of the ACC lead to deficits on IDS performance[39,55]. Therefore, it is interesting that lobule VI's enlargement is associated with impaired cognitive performance on the set-shifting task. It is possible that overgrowth of this structure modified connectivity to the frontal regions that are important for IDS performance. In our previous paper the male VPA rats were worse at the IDS compared to male controls, but it did not reach statistical significance. Here, sorting rats by lobule VI volume, a region altered in ASD and connected to the critical area for IDS performance, revealed that male VPA rats with enlarged lobule VI were in fact significantly impaired at the IDS. This result is novel and suggests that the cerebellum could in part be modulating frontal cognitive function in an animal model of ASD. This hypothesis needs to be tested to verify the role of the cerebellum within this specific cognitive task. The cerebellum could be interacting with the thalamus to

decrease performance as well. Future research should examine this relationship more closely by manipulating lobule VI directly during task performance. Prior groups have used MRI to measure cerebellum volumes and found decreases in overall cerebellar volumes of VPA male rats.[35] The discrepancies in volume measurements between their study and this study could be due to several factors including scanning parameters and differences in rat strains. The current study is unique in that the 3D scans were performed at ultra-high fields of 14 Tesla in a 25 mm probe, compared to the 9.4 Tesla instrumentation utilized in previous studies. While the benefits and deficits of ultra-high field MRI are always a topic of debate, one factor remains consistent, as the strength of the instrumentation increases, the signal to noise ratio increases as well.[56] This was further improved by use of smaller probe which minimized free space around samples, enhancing contrast to noise ratios as well. Ultra-high field, and smaller probe size allowed for crisp images that were delineated without the same complications seen in lower field magnets as the result of low signal to noise ratios. Combining these benefits with imaging without motion, high signal to noise ratio, and high-resolution pushed the boundaries of what is possible in lower fields. The images were not exposed to rigorous post processing techniques that can attribute to artificial smoothing which can potentially obscure lobule folds within the cerebellum. Images acquired in 3D allowed for complete segmentation at each anatomical orientation which resulted in complete and thorough encapsulation of each voxel, which is difficult to perform correctly when restricted to two dimensional views. Additionally, the three-dimensional imaging allowed for tight voxel dimensions with high signal, thus tissue types were more accurately represented within the images. Within MRI, signals were averaged for each voxel which encloses them, by imaging at high resolutions it is possible to more accurately record the signal of limited tissue types which results in more accurate representation of true morphology. Through a combination

of ultra-high resolution and careful manual segmentation by blind to condition observers, it exposed volume changes that may be difficult to see through other methods. In addition, prior work has noted that decreases in lobules VI were associated with decreased purkinje cell numbers.[35] It is possible that the rats in this study also lost purkinje neurons, but that other cells compensated resulting in larger volume. For instance, glial cells have been found to increase in VPA rats.[57,58] To address this issue, the cerebellums from this project are being processed for histology to count purkinje neurons and will be presented in a different manuscript.

4.5.2 Female Rats

In general, female VPA rats had reduced total cerebellum volumes compared to control animals, both females and males. In addition, in alignment with prior groups[59] there was a sex effect demonstrating smaller volumes for female rats, regardless of condition. However, the VPA females had the smallest overall volumes, which is interesting because it coincides with the prior behavioral results from these same animals where VPA females performed the worst at the set-shifting task. Although the cerebellum is not the essential structure for the set-shifting task, it is connected to the frontal areas[60,61] that are necessary for accurate task performance.[37–39] Therefore, it is interesting that VPA females with loss of volume across the entire cerebellum, performed worse across the set-shifting task. The set-shifting task is a digging task and therefore requires motor planning and execution. However, any VPA rats that failed to complete the task were not included in this data set, because only rats that completed all stages of task were scanned in the MRI. VPA rats were not observed to have difficulty with digging, sniffing, or investigating the odor or media cues. This suggests that female rats with reduced overall volumes (rats that completed the task) of the cerebellum were impaired in a way that impacted cognition and not motor function.

Decreased volumes were found for lobule I, IV, and X of the VPA females compared to female control rats. The regression analysis did not find lobule I or IV to be a significant predictor for set-shifting behavior. Lobule IV is part of the anterior cerebellum and linked to the motor cortex.[51] The human literature has found correlations of decreased volume of lobule IV is associated with poorer scores on ASD diagnostic scales measuring social and repetitive behavior.[5] Future studies could evaluate this relationship by testing repetitive and social behaviors, where it would be hypothesized that decreases in lobule IV would lead to exacerbated repetitive behaviors in female VPA rats.

The result that all female rats, regardless of condition, with decreased volumes of left crus I were also worse at the overall task suggests that left crus I may be important for modulating cognitive performance. Crus I volumes were not found to be significantly different between conditions although it appears there was a trend toward the VPAs being smaller ($p = .13$ in table 2). Due to the fact that some VPA female brains were not analyzable, this could be an important factor to evaluate in a larger study. Crus I in rodents is homologous to crus I in humans[40,61] and is connected to the prefrontal cortices[50], to the regions which are critical for this task.[37,39] Crus I in humans is active during set-shifting tasks for non-motor functions in fMRI studies.[62,63] This relationship could be studied more directly in future work, such as manipulating crus I directly and measuring behavioral outcomes. Other groups have found that modulation of right crus I is related to social behaviors in a mouse model of ASD.[19] Perhaps, left crus I is important for cognitive functions future studies should evaluate this hypothesis as well.

Larger lobule X volumes for female control rats were associated with worse IDS performance. In this case, having smaller volumes of lobule X could have been advantageous for VPA rats. Lobule X has been shown to have decreased GABA receptors in VPA mice.[64] In

humans with ASD, alterations within lobule X have been associated with eye-gaze behaviors, although this was for males and not females.[65] Lobule X has mostly been associated with vestibular functions[66] therefore, understanding the role of lobule X as it relates to these issues needs more investigation.

4.5.3 Sex differences

These data also had robust sex differences. The behavioral data indicated that female control rats are worse at the set-shifting task compared to control males[36], however the MRI data highlights sex differences within the VPA model. The female VPA rats had the largest decreases in cerebellar volumes as a whole and were the most impaired on the set-shifting task. In general, VPA males did not have decreases in volume or general impairments in the set-shifting task. However, VPA males with larger lobule VI volumes were impaired at the IDS phase of the task, suggesting that the cerebellum's role for this task may be different based on sex. Female VPA rats were worse when they had decreased left Crus I volumes. Within the VPA model sex differences have been found in communication behaviors, where VPA males exhibited fewer vocalizations than VPA females.[67] Additional tests demonstrated that male VPA rats were more impaired on social behaviors, but both male and female VPA rats exhibited stereotypic behaviors.[67] Additional sex differences have been observed for purkinje cells in the posterior regions of the cerebellum of male mice, with greater loss of purkinje cells occurring in males compared to females.[68] This suggests that based on the specific domain of interest whether, social, cognitive, or repetitive behaviors, and/or brain region, the VPA impact may vary by sex, highlighting the need to test both VPA males and females.

Sex differences in humans with ASD have also been documented. In humans with ASD there is a bias of more males diagnosed with ASD[69], however this is in part due to diagnostic

criteria that were built around male patients. There is a push in the clinical community to acknowledge that different symptoms may occur in females with ASD and that there may be an under diagnosis of females with ASD.[70] This bias is mirrored in the MRI human literature, where most of the volumetric work did not examine sex differences or did not include females with ASD.[71] Therefore, it is possible the manifestation of the disorder is different between the sexes and that there are changes in the cerebellum of females. Additional models of ASD would also be beneficial in examining these issues.

However, sex differences in executive functions have been examined. For example, females with ASD perform worse at executive function tasks compared to males with ASD.[72–74] Clinicians have posited that diagnosis is marred by gender bias[69] and that females with ASD may have a different phenotype compared to males.[70] Whereas males with ASD are impaired in response latency for specific executive function tasks.[75] The current results suggest that it is important to evaluate behavioral and brain differences to understand possible sex differences related to the disorder. It is possible that decreased cerebellar volumes contribute to cognitive flexibility issues for females with ASD, whereas enlarged cerebellar volumes impact male behavior, additional studies are needed to verify this hypothesis.

Altered cerebellar structure and function impacts ASD behaviors including motor behavior but also extends to working memory deficits.[76] The IDS impairment in the male VPA rats suggests that the cerebellum may be modulating set-shifting behaviors in VPA rodents. An important caveat is that early developmental changes to the cerebellum have lifelong impacts on behavior[50], therefore future work should examine if volumes are altered earlier in development within the VPA model.

4.6 Limitations

Although all female VPA brains that completed the task were scanned, a number of them were unanalyzable due to scanner artifact or poor alignment in the holder, which was determined by a reviewer that was blind to condition for all scans. Future studies will need to use a larger sample size to verify the results found here for the female VPA rats. In addition, the volumetric measurements occurred in adult rats, the sex differences observed here could be driven by different developmental mechanisms. Neural sex differences can be impacted by hormones and even differences in micro-RNA functions during development.[77] Future research could measure volumes and behavior at critical developmental time points such as during adolescence, when changes in synaptic pruning are occurring.

One other concern with the version of this task was that there may not have been enough phases before the EDS to see an impairment in the VPA animals on the EDS. The EDS is viewed as being more difficult compared to the IDS, but rats may not show impairments on EDS if they have not formed an attentional set.[78] This may be the case for these rats, and future experiments are using a variant of the set-shifting task with multiple IDS phases, which should further drive set formation, and which may induce an EDS deficit.

4.7 Conclusions

Overall, the results support the hypothesis that changes in cerebellar volume in VPA rats impacts performance of the set-shifting task. Decreased volume was associated with impaired female performance, whereas increased volume of lobule VI was associated with impaired male performance. Recent work has provided evidence that the cerebellum can modulate behavior through frontal cortex connections.[19] These results support this interpretation and provide a

platform for future hypothesis testing to further investigate the role of the cerebellum in cognitive functions within ASD.

4.8 References

1. Demetriou EA, Lampit A, Quintana DS, et al. Autism spectrum disorders: a meta-analysis of executive function. *Molecular Psychiatry 2018 23:5*. 2017;23(5):1198-1204. doi:10.1038/mp.2017.75

2. Geurts HM, Corbett B, Solomon M. The paradox of cognitive flexibility in autism. *Trends in Cognitive Sciences*. 2009;13(2):74-82. doi:10.1016/J.TICS.2008.11.006

3. Hughes C, Russell J, Robbins TW. Evidence for executive dysfunction in autism. *Neuropsychologia*. 1994;32(4):477-492. doi:10.1016/0028-3932(94)90092-2

4. Ozonoff S, Pennington BF, Rogers SJ. Executive function deficits in high-functioning autistic individuals: relationship to theory of mind. *J Child Psychol Psychiatry*. 1991;32(7):1081-1105. doi:10.1111/J.1469-7610.1991.TB00351.X

5. D'Mello AM, Crocetti D, Mostofsky SH, Stoodley CJ. Cerebellar gray matter and lobular volumes correlate with core autism symptoms. *NeuroImage: Clinical*. 2015;7:631-639. doi:10.1016/J.NICL.2015.02.007

6. Fatemi SH, Aldinger KA, Ashwood P, et al. Consensus Paper: Pathological Role of the Cerebellum in Autism. *Cerebellum*. 2012;11(3):777. doi:10.1007/S12311-012-0355-9

7. Mosconi MW, Wang Z, Schmitt LM, Tsai P, Sweeney JA. The role of cerebellar circuitry alterations in the pathophysiology of autism spectrum disorders. *Frontiers in Neuroscience*. 2015;9(SEP):296. doi:10.3389/FNINS.2015.00296/BIBTEX

8. Pierce K, Courchesne E. Evidence for a cerebellar role in reduced exploration and stereotyped behavior in autism. *Biol Psychiatry*. 2001;49(8):655-664. doi:10.1016/S0006-3223(00)01008-8

9. Chen C, van Horn JD. Developmental neurogenetics and multimodal neuroimaging of sex differences in autism. *Brain Imaging and Behavior 2016 11:1*. 2016;11(1):38-61. doi:10.1007/S11682-015-9504-3

10. Morakotsriwan N, Wattanathorn J, Kirisattayakul W, Chaisiwamongkol K. Autistic-Like Behaviors, Oxidative Stress Status, and Histopathological Changes in Cerebellum of Valproic Acid Rat Model of Autism Are Improved by the Combined Extract of Purple Rice and Silkworm Pupae. *Oxidative Medicine and Cellular Longevity*. 2016;2016. doi:10.1155/2016/3206561

11. Mychasiuk R, Richards S, Nakahashi A, Kolb B, Gibb R. Effects of rat prenatal exposure to valproic acid on behaviour and neuro-anatomy. *Dev Neurosci*. 2012;34(2-3):268-276. doi:10.1159/000341786

12. Wang SSH, Kloth AD, Badura A. The Cerebellum, Sensitive Periods, and Autism. *Neuron*. 2014;83(3):518. doi:10.1016/J.NEURON.2014.07.016

13. Bernard JA, Seidler RD, Hassevoort KM, et al. Resting state cortico-cerebellar functional connectivity networks: A comparison of anatomical and self-organizing map approaches. *Frontiers in Neuroanatomy*. 2012;0(AUG 2012):31. doi:10.3389/FNANA.2012.00031/BIBTEX

14. D'Angelo E, Casali S. Seeking a unified framework for cerebellar function and dysfunction: from circuit operations to cognition. *Frontiers in Neural Circuits*. 2012;6(DEC). doi:10.3389/FNCIR.2012.00116

15. Schmahmann JD. The cerebellum and cognition. *Neuroscience Letters*. 2019;688:62-75. doi:10.1016/J.NEULET.2018.07.005

16. Buckner RL, Krienen FM, Castellanos A, Diaz JC, Thomas Yeo BT. The organization of the human cerebellum estimated by intrinsic functional connectivity. *J Neurophysiol*. 2011;106(5):2322-2345. doi:10.1152/JN.00339.2011

17. Guell X, Schmahmann JD, Gabrieli JDE, Ghosh SS. Functional gradients of the cerebellum. *Elife*. 2018;7. doi:10.7554/ELIFE.36652

18. Koppelmans V, Hoogendam YY, Hirsiger S, Mérillat S, Jäncke L, Seidler RD. Regional cerebellar volumetric correlates of manual motor and cognitive function. *Brain Struct Funct*. 2017;222(4):1929-1944. doi:10.1007/S00429-016-1317-7

19. Stoodley CJ, D'Mello AM, Ellegood J, et al. Altered cerebellar connectivity in autism and cerebellar-mediated rescue of autism-related behaviors in mice. *Nature Neuroscience 2017 20:12*. 2017;20(12):1744-1751. doi:10.1038/s41593-017-0004-1

20. Chomiak T, Turner N, Hu B. What We Have Learned about Autism Spectrum Disorder from Valproic Acid. *Patholog Res Int*. 2013;2013. doi:10.1155/2013/712758

21. Christensen J, Grnøborg TK, Srøensen MJ, et al. Prenatal valproate exposure and risk of autism spectrum disorders and childhood autism. *JAMA*. 2013;309(16):1696-1703. doi:10.1001/JAMA.2013.2270

22. Dean JCS, Hailey H, Moore SJ, Lloyd DJ, Turnpenny PD, Little J. Long term health and neurodevelopment in children exposed to antiepileptic drugs before birth. *Journal of Medical Genetics*. 2002;39(4):251. doi:10.1136/JMG.39.4.251

23. Mabunga DFN, Gonzales ELT, Kim J woon, Kim KC, Shin CY. Exploring the Validity of Valproic Acid Animal Model of Autism. *Experimental Neurobiology*. 2015;24(4):285. doi:10.5607/EN.2015.24.4.285

24. Schneider T, Przewłocki R. Behavioral Alterations in Rats Prenatally Exposed to Valproic Acid: Animal Model of Autism. *Neuropsychopharmacology 2005 30:1*. 2004;30(1):80-89. doi:10.1038/sj.npp.1300518

25. Jeon SJ, Gonzales EL, Mabunga DFN, et al. Sex-specific Behavioral Features of Rodent Models of Autism Spectrum Disorder. *Experimental Neurobiology*. 2018;27(5):321-343. doi:10.5607/EN.2018.27.5.321

26. Rasalam AD, Hailey H, Williams JHG, et al. Characteristics of fetal anticonvulsant syndrome associated autistic disorder. *Dev Med Child Neurol*. 2005;47(8):551-555. doi:10.1017/S0012162205001076

27. Phiel CJ, Zhang F, Huang EY, Guenther MG, Lazar MA, Klein PS. Histone Deacetylase Is a Direct Target of Valproic Acid, a Potent Anticonvulsant, Mood Stabilizer, and Teratogen *. *Journal of Biological Chemistry*. 2001;276(39):36734-36741. doi:10.1074/JBC.M101287200

28. Hou Q, Wang Y, Li Y, Chen D, Yang F, Wang S. A developmental study of abnormal behaviors and altered GABAergic signaling in the VPA-treated rat model of autism. *Frontiers in Behavioral Neuroscience*. 2018;12:182. doi:10.3389/FNBEH.2018.00182/BIBTEX

29. Weinstein-Fudim L, Ergaz Z, Turgeman G, Yanai J, Szyf M, Ornoy A. Gender Related Changes in Gene Expression Induced by Valproic Acid in A Mouse Model of Autism and the Correction by S-adenosyl Methionine. Does It Explain the Gender Differences in Autistic Like Behavior? *International Journal of Molecular Sciences 2019, Vol 20, Page 5278*. 2019;20(21):5278. doi:10.3390/IJMS20215278

30. Deng W, Zou X, Deng H, et al. The Relationship among Genetic Heritability, Environmental Effects, and Autism Spectrum Disorders. *Journal of Child Neurology*. 2015;30(13):1794-1799. doi:10.1177/0883073815580645

31. Hallmayer J, Cleveland S, Torres A, et al. Genetic Heritability and Shared Environmental Factors Among Twin Pairs with Autism. *Archives of General Psychiatry*. 2011;68(11):1095-1102. doi:10.1001/ARCHGENPSYCHIATRY.2011.76

32. Modabbernia A, Velthorst E, Reichenberg A. Environmental risk factors for autism: an evidence-based review of systematic reviews and meta-analyses. *Molecular Autism 2017 8:1*. 2017;8(1):1-16. doi:10.1186/S13229-017-0121-4

33. Ingram JL, Peckham SM, Tisdale B, Rodier PM. Prenatal exposure of rats to valproic acid reproduces the cerebellar anomalies associated with autism. *Neurotoxicol Teratol*. 2000;22(3):319-324. doi:10.1016/S0892-0362(99)00083-5

34. Main SL, Kulesza RJ. Repeated prenatal exposure to valproic acid results in cerebellar hypoplasia and ataxia. *Neuroscience*. 2017;340:34-47. doi:10.1016/J.NEUROSCIENCE.2016.10.052

35. Spisák T, Román V, Papp E, et al. Purkinje cell number-correlated cerebrocerebellar circuit anomaly in the valproate model of autism. *Scientific Reports 2019 9:1*. 2019;9(1):1-15. doi:10.1038/s41598-019-45667-1

36. McKinnell ZE, Maze T, Ramos A, Challans B, Plakke B. Valproic acid treated female Long-Evans rats are impaired on attentional set-shifting. *Behavioural Brain Research*. 2021;397. doi:10.1016/j.bbr.2020.112966

37. Birrell JM, Brown VJ. Medial frontal cortex mediates perceptual attentional set shifting in the rat. *J Neurosci*. 2000;20(11):4320-4324. doi:10.1523/JNEUROSCI.20-11-04320.2000

38. Chase EA, Tait DS, Brown VJ. Lesions of the orbital prefrontal cortex impair the formation of attentional set in rats. *Eur J Neurosci*. 2012;36(3):2368-2375. doi:10.1111/J.1460-9568.2012.08141.X

39. Ng CW, Noblejas MI, Rodefer JS, Smith CB, Poremba A. Double dissociation of attentional resources: prefrontal versus cingulate cortices. *J Neurosci*. 2007;27(45):12123-12131. doi:10.1523/JNEUROSCI.2745-07.2007

40. Luo Y, Fujita H, Nedelescu H, et al. Lobular homology in cerebellar hemispheres of humans, non-human primates and rodents: a structural, axonal tracing and molecular expression analysis. *Brain Structure and Function 2017 222:6*. 2017;222(6):2449-2472. doi:10.1007/S00429-017-1436-9

41. Andropoulos DB. Effect of Anesthesia on the Developing Brain: Infant and Fetus. *Fetal Diagnosis and Therapy*. 2018;43(1):1-11. doi:10.1159/000475928

42. Paxinos G, Watson C. The rat brain in stereotaxic coordinates. Academic Press. *Journal of Anatomy*. 2006;6th Edition(2).

43. CRAN - Package lme4. Accessed July 3, 2022. https://cran.r-project.org/web/packages/lme4/index.html

44. Gelman A, Hill J. Data Analysis Using Regression and Multilevel/Hierarchical Models. *Data Analysis Using Regression and Multilevel/Hierarchical Models*. Published online December 18, 2006. doi:10.1017/CBO9780511790942

45. Lazic SE, Essioux L. Improving basic and translational science by accounting for litter-to-litter variation in animal models. *BMC Neuroscience*. 2013;14(1):1-11. doi:10.1186/1471-2202-14-37/FIGURES/4

46. CRAN - Package emmeans. Accessed July 3, 2022. https://cran.r-project.org/web/packages/emmeans/index.html

47. CRAN - Package ggplot2. Accessed July 4, 2022. https://cran.r-project.org/web/packages/ggplot2/index.html

48. Courchesne E, Saitoh O, Yeung-Courchesne R, et al. Abnormality of cerebellar vermian lobules VI and VII in patients with infantile autism: identification of hypoplastic and hyperplastic subgroups with MR imaging. *AJR Am J Roentgenol*. 1994;162(1):123-130. doi:10.2214/AJR.162.1.8273650

49. Coffman KA, Dum RP, Strick PL. Cerebellar vermis is a target of projections from the motor areas in the cerebral cortex. *Proc Natl Acad Sci U S A*. 2011;108(38):16068-16073. doi:10.1073/PNAS.1107904108/ASSET/DC8EE52A-4C5F-4A26-AE43-C5CF2B413F07/ASSETS/GRAPHIC/PNAS.1107904108FIG07.JPEG

50. Badura A, Verpeut JL, Metzger JW, et al. Normal cognitive and social development require posterior cerebellar activity. *Elife*. 2018;7. doi:10.7554/ELIFE.36401

51. Stoodley CJ, Schmahmann JD. Evidence for topographic organization in the cerebellum of motor control versus cognitive and affective processing. *Cortex*. 2010;46(7):831-844. doi:10.1016/J.CORTEX.2009.11.008

52. Agam Y, Joseph RM, Barton JJS, Manoach DS. Reduced cognitive control of response inhibition by the anterior cingulate cortex in autism spectrum disorders. *Neuroimage*. 2010;52(1):336-347. doi:10.1016/J.NEUROIMAGE.2010.04.010

53. Charman T, Pickles A, Simonoff E, Chandler S, Loucas T, Baird G. IQ in children with autism spectrum disorders: data from the Special Needs and Autism Project (SNAP). *Psychol Med*. 2011;41(3):619-627. doi:10.1017/S0033291710000991

54. Stoodley CJ, Valera EM, Schmahmann JD. Functional topography of the cerebellum for motor and cognitive tasks: An fMRI study. *Neuroimage*. 2012;59(2):1560-1570. doi:10.1016/J.NEUROIMAGE.2011.08.065

55. Bubb EJ, Aggleton JP, O'Mara SM, Nelson AJD. Chemogenetics Reveal an Anterior Cingulate–Thalamic Pathway for Attending to Task-Relevant Information. *Cerebral Cortex*. 2021;31(4):2169-2186. doi:10.1093/CERCOR/BHAA353

56. Ladd ME, Bachert P, Meyerspeer M, et al. Pros and cons of ultra-high-field MRI/MRS for human application. *Progress in Nuclear Magnetic Resonance Spectroscopy*. 2018;109:1-50. doi:10.1016/J.PNMRS.2018.06.001

57. Bronzuoli MR, Facchinetti R, Ingrassia D, et al. Neuroglia in the autistic brain: evidence from a preclinical model. *Molecular Autism*. 2018;9(1):1-17. doi:10.1186/S13229-018-0254-0/FIGURES/10

58. Kazlauskas N, Campolongo M, Lucchina L, Zappala C, Depino AM. Postnatal behavioral and inflammatory alterations in female pups prenatally exposed to valproic acid. *Psychoneuroendocrinology*. 2016;72:11-21. doi:10.1016/J.PSYNEUEN.2016.06.001

59. Sumiyoshi A, Nonaka H, Kawashima R. Sexual differentiation of the adolescent rat brain: A longitudinal voxel-based morphometry study. *Neuroscience Letters*. 2017;642:168-173. doi:10.1016/J.NEULET.2016.12.023

60. Kelly RM, Strick PL. Cerebellar loops with motor cortex and prefrontal cortex of a nonhuman primate. *J Neurosci*. 2003;23(23):8432-8444. doi:10.1523/JNEUROSCI.23-23-08432.2003

61. Sugihara I. Crus I in the Rodent Cerebellum: Its Homology to Crus I and II in the Primate Cerebellum and Its Anatomical Uniqueness Among Neighboring Lobules. *The Cerebellum 2017 17:1*. 2017;17(1):49-55. doi:10.1007/S12311-017-0911-4

62. Ide JS, Li C shan R. A cerebellar thalamic cortical circuit for error-related cognitive control. *Neuroimage*. 2011;54(1):455-464. doi:10.1016/J.NEUROIMAGE.2010.07.042

63. Le TH, Pardo J v., Hu X. 4 T-fMRI study of nonspatial shifting of selective attention: Cerebellar and parietal contributions. *Journal of Neurophysiology*. 1998;79(3):1535-1548. doi:10.1152/JN.1998.79.3.1535/ASSET/IMAGES/LARGE/JNP.MR18F5.JPEG

64. Varman DR, Soria-Ortíz MB, Martínez-Torres A, Reyes-Haro D. GABAρ3 expression in lobule X of the cerebellum is reduced in the valproate model of autism. *Neuroscience Letters*. 2018;687:158-163. doi:10.1016/J.NEULET.2018.09.042

65. Skefos J, Cummings C, Enzer K, et al. Regional Alterations in Purkinje Cell Density in Patients with Autism. *PLOS ONE*. 2014;9(2):e81255. doi:10.1371/JOURNAL.PONE.0081255

66. Xiong G, Matsushita M. Connections of Purkinje cell axons of lobule X with vestibulocerebellar neurons projecting to lobule X or IX in the rat. *Experimental Brain Research 2000 133:2*. 2000;133(2):219-228. doi:10.1007/S002210000372

67. Melancia F, Schiavi S, Servadio M, et al. Sex-specific autistic endophenotypes induced by prenatal exposure to valproic acid involve anandamide signalling. *British Journal of Pharmacology*. 2018;175(18):3699-3712. doi:10.1111/BPH.14435

68. Roux S, Bailly Y, Bossu JL. Regional and sex-dependent alterations in Purkinje cell density in the valproate mouse model of autism. *NeuroReport*. 2019;30(2):82-88. doi:10.1097/WNR.0000000000001164

69. Loomes R, Hull L, Mandy WPL. What Is the Male-to-Female Ratio in Autism Spectrum Disorder? A Systematic Review and Meta-Analysis. *Journal of the American Academy of Child & Adolescent Psychiatry*. 2017;56(6):466-474. doi:10.1016/J.JAAC.2017.03.013

70. Lai MC, Lombardo M v., Pasco G, et al. A Behavioral Comparison of Male and Female Adults with High Functioning Autism Spectrum Conditions. *PLOS ONE*. 2011;6(6):e20835. doi:10.1371/JOURNAL.PONE.0020835

71. Stoodley CJ. Distinct regions of the cerebellum show gray matter decreases in autism, ADHD, and developmental dyslexia. *Frontiers in Systems Neuroscience*. 2014;8(MAY):92. doi:10.3389/FNSYS.2014.00092/ABSTRACT

72. Nydén A, Hjelmquist E, Gillberg C. Autism spectrum and attention – deficit disorders in girls. Some neuropsychological aspects. *European Child & Adolescent Psychiatry 2000 9:3*. 2000;9(3):180-185. doi:10.1007/S007870070041

73. Lemon JM, Gargaro B, Enticott PG, Rinehart NJ. Brief report: Executive functioning in autism spectrum disorders: A gender comparison of response inhibition. *Journal of Autism and Developmental Disorders*. 2011;41(3):352-356. doi:10.1007/S10803-010-1039-2/TABLES/2

74. Memari AH, Ziaee V, Shayestehfar M, Ghanouni P, Mansournia MA, Moshayedi P. Cognitive flexibility impairments in children with autism spectrum disorders: Links to age, gender and child outcomes. *Research in Developmental Disabilities*. 2013;34(10):3218-3225. doi:10.1016/J.RIDD.2013.06.033

75. Bölte S, Duketis E, Poustka F, Holtmann M. Sex differences in cognitive domains and their clinical correlates in higher-functioning autism spectrum disorders. *Autism*. 2011;15(4):497-511. doi:10.1177/1362361310391116

76. Tsai PT. Autism and cerebellar dysfunction: Evidence from animal models. *Seminars in Fetal and Neonatal Medicine*. 2016;21(5):349-355. doi:10.1016/J.SINY.2016.04.009

77. McCarthy MM, Pickett LA, VanRyzin JW, Kight KE. Surprising origins of sex differences in the brain. *Hormones and Behavior*. 2015;76:3-10. doi:10.1016/J.YHBEH.2015.04.013

78. Tait DS, Bowman EM, Neuwirth LS, Brown VJ. Assessment of intradimensional/extradimensional attentional set-shifting in rats. *Neurosci Biobehav Rev*. 2018;89:72-84. doi:10.1016/J.NEUBIOREV.2018.02.013

Chapter 5 - Adolescent female valproic acid rats have impaired extra-dimensional shifts of attention and enlarged anterior cingulate cortices[3]

5.1 Abstract

In order to develop better treatments for autism spectrum disorder (ASD) it is critical to understand the developmental trajectory of the disorder and the accompanying brain changes. This study used the valproic acid (VPA) model to induce ASD-like symptoms in rodents. Prior studies have demonstrated that VPA animals are impaired on executive function tasks, paralleling results in humans with ASD. Here, VPA adolescent female rats were impaired on a set-shifting task and had enlarged frontal cortices compared to control females. The deficits observed in the VPA female rats mirrors results in females with ASD. In addition, adolescent VPA females with enlarged frontal cortices performed the worst across the entire task. These brain changes in adolescence are also found in adolescent humans with ASD. These novel findings highlight the importance of studying the brain at different developmental stages.

[3]Reprinted with permission from Mali, I., Payne, M., King, C., Maze, T.R., Challans, B., Bossmann, S.H., Plakke, B. (2022). Adolescent female valproic acid rats have impaired extra-dimensional shifts of attention and enlarged anterior cingulate cortices. Manuscript submitted for publication

5.2 Introduction

Autism spectrum disorder (ASD) is a prevalent neurodevelopmental disorder with social, communication and repetitive behavior deficits. Frequently humans with ASD also exhibit problems with executive functions.[1–3] Clinical work has found that females with ASD have a different symptom profile than males with ASD[4,5] and that the error types in cognitive testing may also differ.[6] One way to begin to understand these differences is to use animal models of ASD. The valproic acid (VPA) model of ASD has been widely used and has both face and construct validity.[7] Different labs have established the timeline for VPA administration[8] and found social and repetitive behavioral deficits[9–12] in the offspring. The mechanisms of VPA exposure leading to ASD symptomology are still being researched, but hypotheses regarding changes in synaptic excitation and inhibition balance, HDAC inhibition as well as alterations to various neurotransmitter systems are being examined.[13,14] In addition, adult human females that have been taking medications with VPA compounds have children that develop ASD at a higher rate than the general population.[15–17] Although the VPA model is environmental, only 40-50% of the variance of developing ASD is unexplained by genetic risks, which means more than one model is needed to understand the various types of ASD.[18–20]

The rodent attentional set-shifting task (ASST) requires that animals learn that a particular cue leads to reward, while ignoring unnecessary cues in the environment. After the animal learns the specific rule such as odor (i.e., lemon) or digging medium (i.e., shredded paper) leads to reward and reaches criterion, then the rule is changed. The task was developed to model some of the deficits observed in humans that use the Wisconsin Card Sorting Task (WCST)[21]. There are different phases of the task. The intra-dimensional shift (ID) is when new exemplars are given to the subject, but the same rule applies (i.e., if odor was the rewarded cue,

then the new correct cue will also be an odor cue). For the extra-dimensional shift, the attentional domain shifts from the odor cue to the digging cue. Past research has indicated that multiple ID phases results in the formation of an attentional set[22,23], meaning that the ED is more difficult to perform compared to ID phases. The ASST relies on a wide neural network of brain regions for correct performance, with medial prefrontal regions mediating ED shifts[24,25] and the anterior cingulate mediating ID shifts.[26,27]

A recent publication demonstrates that VPA rats were impaired when performing the set-shifting task, which was designed to capture executive function deficits observed in humans.[25] This paper also found that VPA females were significantly impaired across the set-shifting task, compared to female controls and VPA males. In humans, executive function deficits are more common in females with ASD[28–33], which the set-shifting task measures and which supports the hypothesis that females with ASD may present different symptomology than males with ASD.[34] Recent research has found that adult VPA animals were impaired on an attentional set-shifting task[35], however since ASD is a developmental disorder it is important to study cognitive changes at earlier developmental ages.

In adolescent humans with ASD, it has been found that frontal regions of the brain, which are critical for cognitive flexibility, are enlarged with more cortical thickness compared to age matched controls.[36–38] Cortical thickness also decreases at an accelerated rate throughout the lifespan for ASD.[36,39–41] The VPA model has induced cellular changes within the medial prefrontal cortex, where pyramidal cells are less excitable than in controls.[42,43] This project asked if adolescent VPA rats would be impaired on the ED shift of the ASST and hypothesized that adolescent VPA rats would be impaired on the set-shifting task by taking more trials to complete the ED phase compared to control animals. It was also predicted that increased volumetric

measurements of the VPA animals within the medial prefrontal cortices would occur. These results would support the hypothesis that these structural brain changes are contributing to altered executive function and could indicate that earlier interventions to boost plasticity may improve cognition. It is necessary to know when brain volumes are impacted within development so that targeted treatments can be made before cognitive deficits occur. Children with ASD are impaired at similar tasks[44,45] and also show alterations within the frontal cortex.[46] Correlations between brain volume and performance on the task were conducted in order to examine if excessive frontal cortex volume was related to decreased task performance.

5.3 Results

5.3.1 ASST Performance

On trials to criterion for the females there was a significant interaction between phase and condition ($F_{6,72}$=2.34, p=0.03); and the LSD post hoc found that the ED phase between controls and VPA rats was different (p=0.04), with VPA rats having more trials to criterion, (**Figure 5.2**).

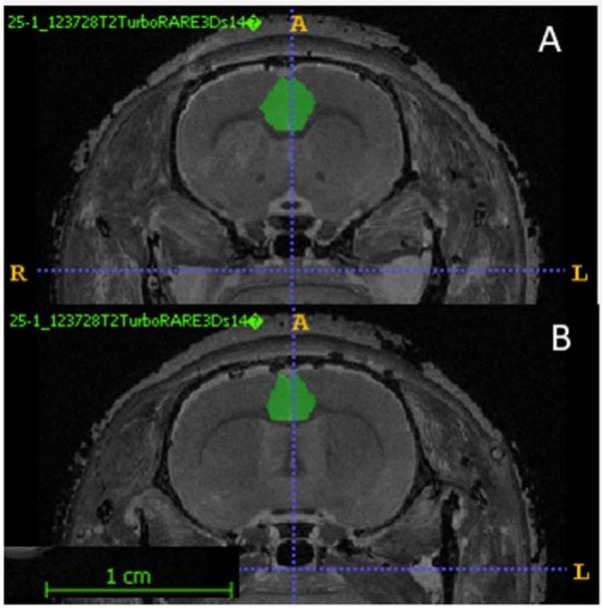

Figure 5.1 MRI of frontal cortex region. A) coronal view at +2.16 from bregma showing start of ACC and, B) shows end of ACC at -.60 mm from bregma.

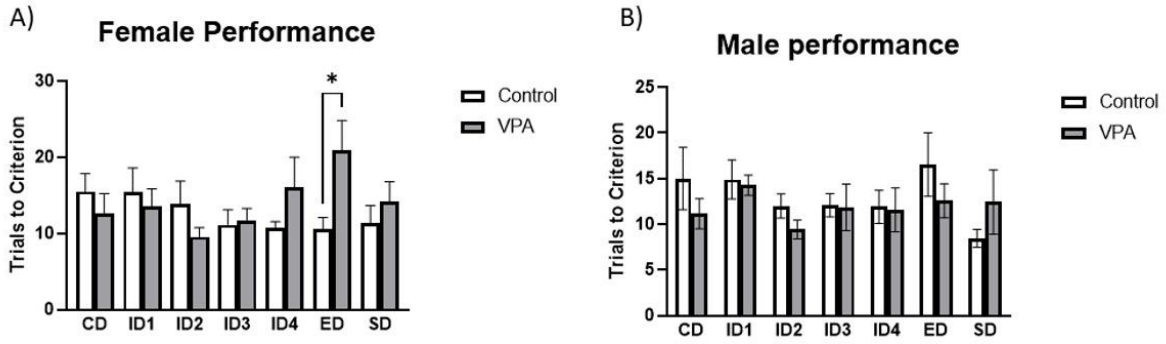

Figure 5.2 Trial to criterion data for set-shifting task. Panel A) VPA female rats were worse at the ED shift compared to control females (*p <0.05); VPA= 7, saline=8). Panel B) Male VPA rats were not different compared to control males (VPA= 7, saline=10).

On trials to criterion for males there were no significant condition or interaction effects. Female control rats improved across the ID phases (fewer trials to criterion for each phase (mean performance: ID1 = 15, ID2 = 14, ID3 = 11, ID 4 = 10), whereas for the VPA females there was a brief improvement for ID2 = 9, but worsened performance on ID3 = 12 and ID4 = 17. The impairments on ID4 and the ED phases for the VPA rats are not due to basic learning issues, motor problems or fatigue as there was no group difference on the simple discrimination after the ED.

One of the reasons the four phases of ID were used in this task, is that female rats in the prior studies failed to form an attentional set, including control females.[35] The four ID phases are meant to drive setformation.[22,47] Here, the control females still failed to form an attentional set as defined by completing more trials on the ED compared to the mean across the ID phases. Whereas the VPA females did show set-formation as demonstrated by having a shift cost (more trials on ED compared to mean of ID phases), **Figure 3**. Both VPA and control males demonstrated a shift cost as well, **Figure 5.3**. There were no significant group differences for latency data.

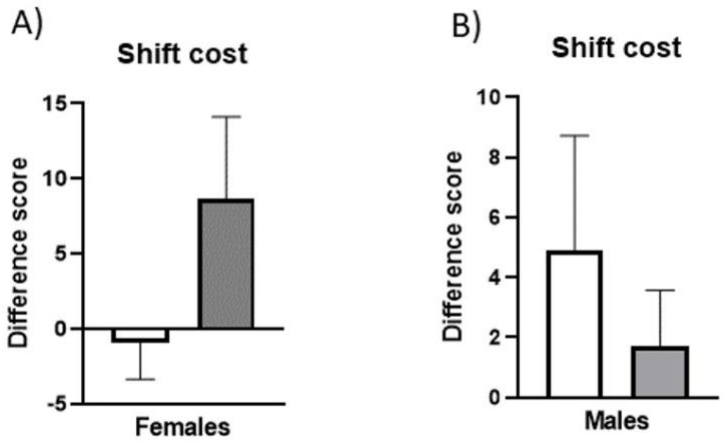

Figure 5.3 Mean shift costs for A) females and B) males. A) VPA females had a shift cost, that is it required more trials to criterion for the ED shift compared to the mean across the 1-4 ID phases. B) Both control and VPA males also showed this shift cost

5.3.2 Frontal Cortex Volumes

The mPFC was not significantly altered in the female VPA animals compared to female control rats. The ACC of female VPA rats was enlarged compared to control rats (t_{13}=2.05, p=.03), **Figure 5.4**). The total PFC of the VPA rats was marginally larger than the control rats (t_{13}=1.60, p=.06). There was also a significant correlation between total PFC volume and total trials completed for the VPA female rats (Pearson r =.7662, p= 0.04), indicating that enlarged frontal cortex volumes were associated with worse task performance, **Figure 5.5** (more trials across all phases of the task). This correlation was almost significant for the control rats as well (Pearson r =.7410, p= .05), which suggests that enlarged volumes during adolescence may impact cognitive performance. There were no significant group differences for male rats and frontal cortex regions, mPFC, ACC or the total PFC. **Figure 5.6**, demonstrates a significant correlation between performance on the first ID shift phase and anterior cingulate volume, (control: Pearson r =-.69, p= 0.03; VPA: r=-.79, p=0.03).

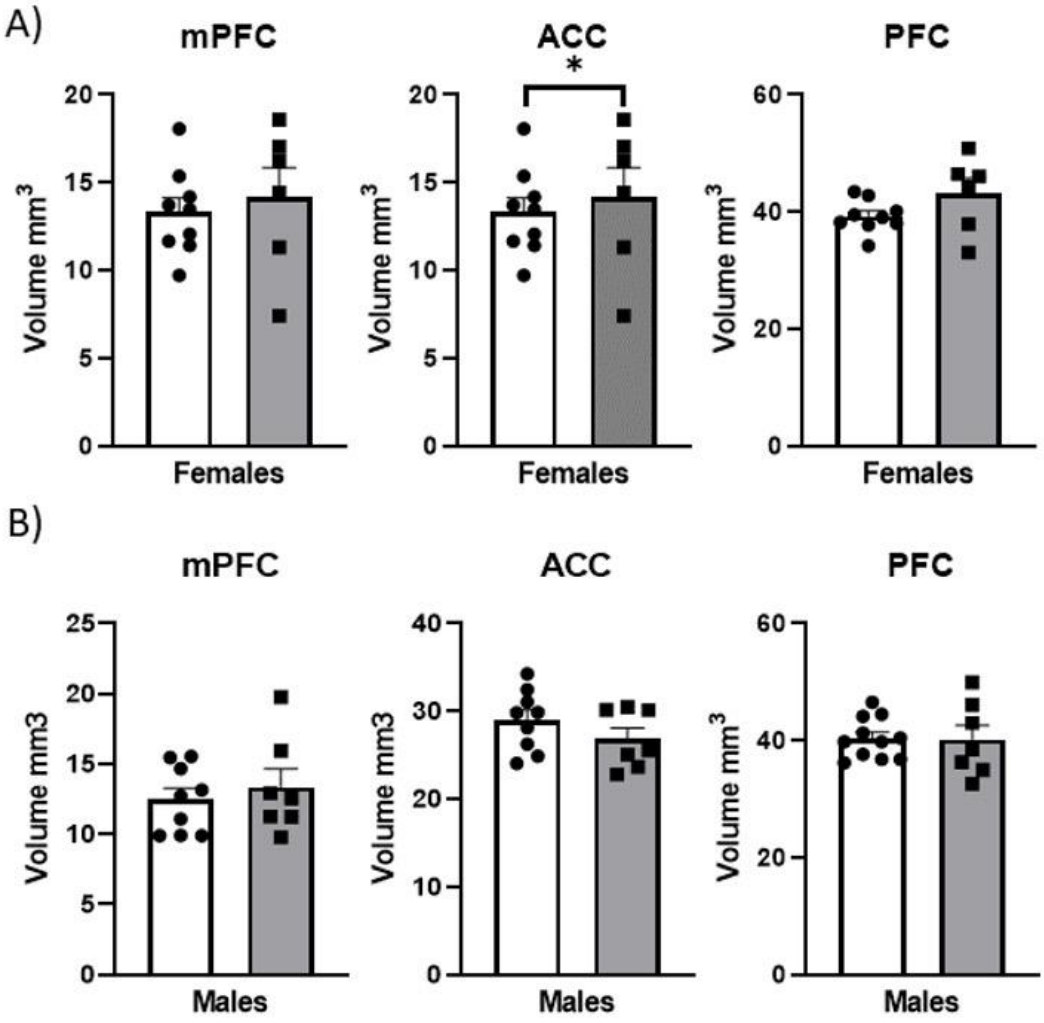

Figure 5.4 Volumes for A) females and B) males. A) Graphs for mPFC, ACC, and total PFC volume are shown. The VPA females had significantly increased volumes of the ACC compared to control females, ($p<0.05$). There were no significant condition differences for male volumes.

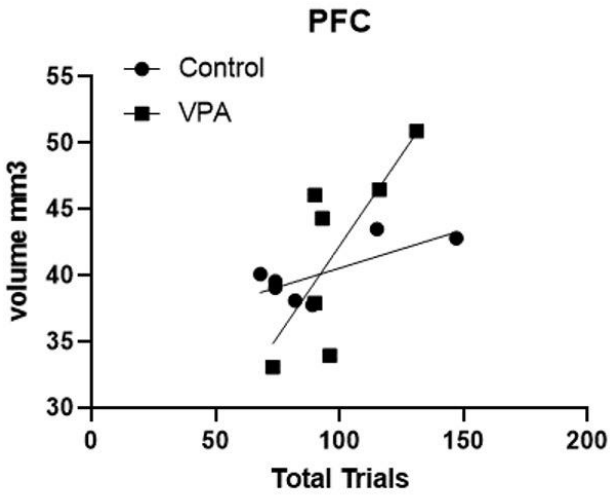

Figure 5.5 Correlation of total trials to PFC volume. A significant correlation (p=0.04, N=7) for VPA females demonstrated that females with worse task performance (as measured by more trials to complete the task) had enlarged frontal cortex volumes. Control rats had a similar trend (p=0.05, N=7).

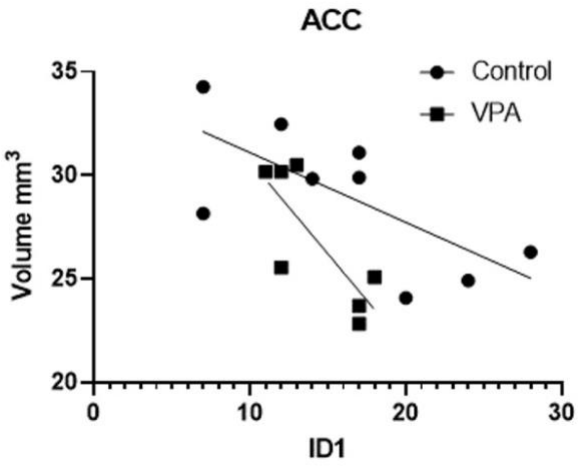

Figure 5.6 Correlation of ID 1 trials and ACC volume. A significant correlation (Control p=0.03, N=9; VPA p=0.03, N=7) indicated that larger volumes of the ACC, regardless of treatment condition, led to better performance on the first ID phase of the task.

5.3.3 Marble burying task

Adolescent rats (PND 28-29) performed a marble burying task. Behaviors were video coded for bouts and percent of time spent digging, being inactive, grooming, exploring the arena, and interacting with the marble.

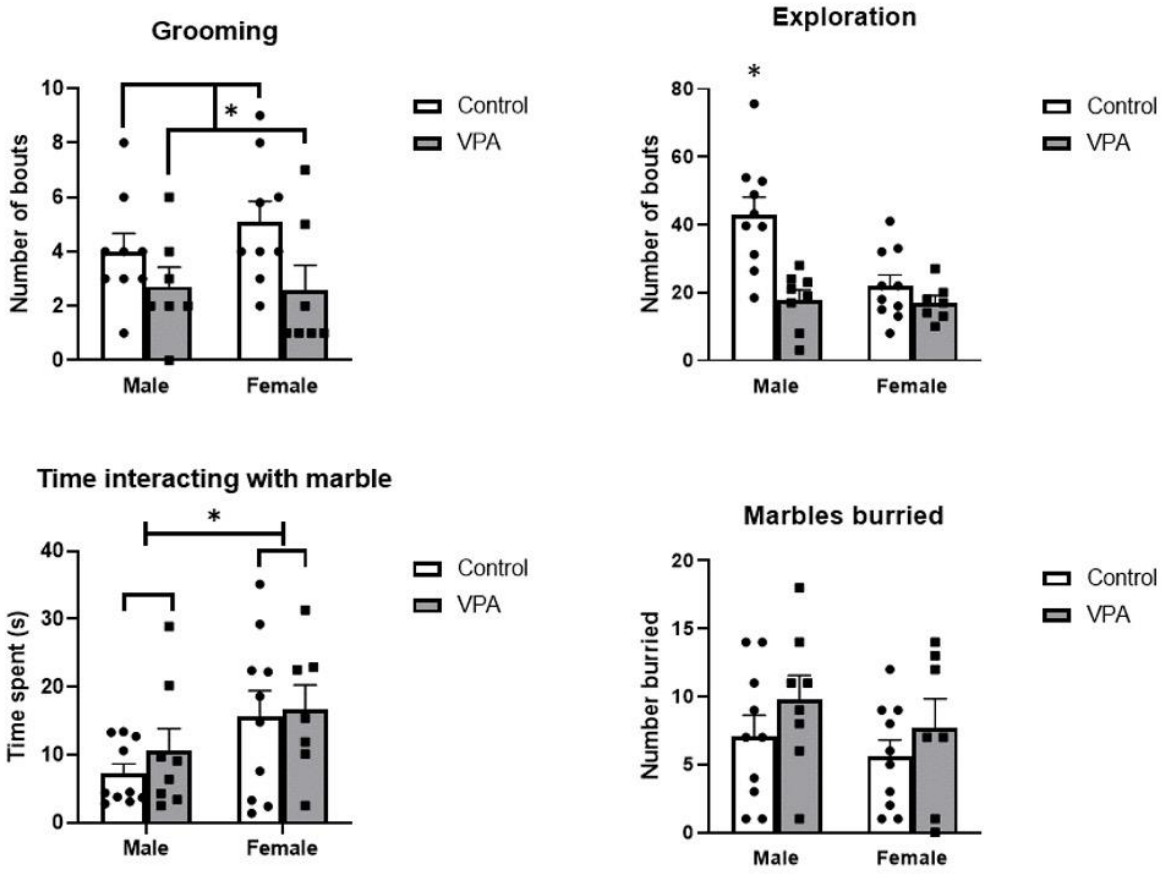

Figure 5.7 Behaviors scored during marble burying. A) Control male rats explored the area significantly more than VPA males, VPA females or control females. B) Both male and female VPA rats engaged in less selfgrooming during this task compared to controls. C) VPA rats spent more time interacting with marbles compared to controls. D) Number of marbles buried. (*p<0.05); N= 10 control males, N=8 VPA males, N=10 control females, N=7 VPA females).

There was a significant effect of condition for the number of grooming bouts ($F_{1,31}$=6.17, p=.01) demonstrating VPA rats spent less time than controls grooming. There was a significant

interaction for exploration bouts ($F_{1,31}$=6.73, p=.014) and significant main effect of sex ($F_{1,31}$=7.92, p=.008) and condition ($F_{1,31}$=15.03, p=.000). Tukey post hocs demonstrated that control males spent the most time exploring compared to VPA males (p=0.003), VPA females (p=0.000), and control females (p=0.001). In general females spent less time exploring and VPA rats spent less time than controls exploring. There was a significant main effect of time spent being inactive ($F_{1,31}$=5.39, p=.02), with females spending more time interacting with the marbles than males. VPA males buried (mean= 9.75) more marbles than control males (mean =7.1) and VPA females buried (7.4 vs 5.6 means) for control females; while this relationship did not reach statistical significance it supports the repetitive behaviors observed in VPA animals, **figure 5.7**.

5.4 Discussion

The main findings demonstrate that adolescent female VPA rats have impaired cognitive function as measured by the ASST. The impairment on this task aligns with similar data in humans with ASD where females performed worse on the Wisconsin Card Sorting Task[28] and is consistent with the prior findings in adult VPA females.[48] The second important result was that increased frontal cortex volumes in female VPA rats were associated with worse overall task performance. This is a novel finding for the VPA model and parallels the overgrowth seen in adolescent humans with ASD.[49] The VPA males were not impaired on the set-shifting task compared to male controls, which aligns with past findings.[35] Prior research has indicated that adolescent rats have more cognitive rigidity compared to adults and suggested that immature frontal cortex was a contributing factor[50]; the current data supports this hypothesis.

5.4.1 Sex differences

The behavioral deficit and change in brain volumes occurring in female rats is an important result. The clinical community has recognized that a different behavioral phenotype is

presented in females with ASD compared to males with ASD.[51,52] These results implicate changes in cognition and brain anatomy that align with those observed in adolescents with ASD. For instance, researchers have suggested that those with ASD have weaker long range connections that impact executive functions.[53] Loss of grey matter has also been found in twin females with ASD and the greater loss of volume in temporal lobes was associated with more symptoms.[54] Females with ASD have alterations in the default mode and central executive networks, whereas males have greater differences in salience networks[55], these differences could also contribute to altered executive functions in females with ASD. Other research has found females with ASD had more perseverative errors[31] compared to males with ASD, which is similar to the ED deficit observed in this study.

The shift-cost analysis suggests that VPA females, VPA males and control males formed an attentional set. This provides evidence that the multiple ID phases did drive set formation for most of the groups. Female controls failed to form an attentional set, even with the multiple ID phases. This could partly be driven by the fact that some control females had enlarged frontal cortices and also performed poorly across the entire task. Future studies could assess changes in cognition across developmental ages with different types of tasks. It would be beneficial to observe neural activity in critical regions such as the mPFC and ACC during task performance. In addition, differences could relate to synaptic pruning or other developmental changes occurring within this critical stage of development.

For male control and VPA rats there was a significant correlation between performance on phase ID1 and anterior cingulate volume, suggesting that enlarged volumes led to improved performance for this first exposure to the ID shift. There were no volume differences between control and VPA groups within the anterior cingulate which indicates this observation is

independent of treatment condition. Prior data has found that enlarged volumes of lobule VI of the cerebellum is associated with impaired ID performance[56], and lobule VI is connected to the anterior cingulate cortex[57]. Therefore, it would be interesting to track developmental changes occurring in both frontal and cerebellar regions and compare how those interactions could impact cognitive development.

5.4.2 Brain changes within ASD and parallels in the VPA model

Structurally it has been demonstrated that there is an excessive amount of grey matter within frontal areas in adolescent humans with ASD[38,49]. In addition, dysregulation of these frontal regions has been associated with changes in cognition in humans with ASD[58–60], including during adolescence.[61] Finding increases in frontal volumes in this study supports that the VPA model is capturing another component of the disorder, with the increases in PFC volume being greater in the VPA females compared to control females. Although the mPFC volumes did not reach statistical significance, this could be resolved in future studies with more animals, which may increase statistical power to verify this relationship.

Human longitudinal studies suggest that frontal cortex and other cortical regions with overgrowth are then followed by periods where grey matter declines at a faster rate in those with ASD.[36,39,62] One important factor to consider with excessive volumes is which cell type or process has contributed to the overgrowth. In human postmortem studies there have been reports of excessive levels of gliosis and enhanced levels of microglia.[63,64] During adolescence it has been found that those with ASD have increased levels of microglia within the ACC and orbital frontal cortex.[65] Some research suggests these differences in volume may relate to a delay in pruning mechanisms.[66] Future studies could examine glial cell ratios of cortex regions in VPA

rodents and also examine markers of pruning or synaptic changes at different developmental ages throughout adolescence.[67,68]

The marble burying task demonstrated an effect of condition on grooming behavior, where VPA animals spent less time grooming. In addition, there was an effect of condition and sex on exploration behavior. Control males explored the most with VPA animals exploring the least. Female rats interacted with the marbles more than males, regardless of condition. Lastly, although it did not reach statistical significance, the fact that both VPA males and VPA females buried more marbles than controls support the hypothesis that there was an increase in some repetitive behavior.

5.5 Conclusion

In summary, VPA adolescent females were impaired on the set-shifting task and had enlarged frontal cortices. These enlarged cortices were correlated to worse task performance. Both of the behavioral and frontal overgrowth results have corresponding outcomes in the adolescent ASD clinical population. These results provide evidence suggesting that neurobiological brain changes in adolescent are impacting cognition. Future research can clarify the type of cellular changes that are occurring at this critical age of development and may assist with creation of future treatments for autism.

5.6 Methods and Materials

5.6.1 Subjects

Pregnant dams (Long-Evans) rats were shipped from Charles River on gestational day 6 to the research facility. Dams were injected on gestational day 12 with a single dose of saline or VPA (sodium valproate (Sigma), 250mg/ml, mixed in saline, 600 mg/kg). Dams were briefly

anesthetized on isoflurane gas to administer a less stressful I.P. injection. The isoflurane administration (required by the IACUC) was very brief lasting only a few minutes and should not have adversely effected the pups, as more prolonged exposure is required to see adverse effects in offspring.[69] All procedures were conducted in accordance with the Kansas State University IACUC guidelines. Rats were given free access to food except for when undergoing preparation for the set-shifting task. Lights were on starting at 7 am- 7 pm. Rats were reared with litter mates until weaning, then were pair housed with a same sex littermate. One male and one female from each litter was used for each experimental condition to account for the litter effect.[70]

5.6.2 Video equipment

All videos were collected and analyzed with the Limelight software camera system (Actimetrics, IL).

5.6.3 Marble burying

Rats (PND 28) were placed in a doublewide home cage (40 W x 43 L x 20 H cm) filled 3 cm deep with regular pine bedding. They were allowed to habituate for 5 minutes then placed in their home cage briefly while an arrangement of 20 marbles (2.5 cm diameter of the marble) in a 4 x 5 pattern were placed on the bedding in the double wide cage. Rats were then placed back in the double-wide cage and had 10 minutes to bury marbles. Rats were videotaped and a picture was taken at the end of the session. The container was emptied, wiped down with Peroxigard cleaner, dried and then refilled for the next session. Marbles buried by greater than 2/3 were considered buried. Additional behaviors, coded by blind to condition reviewers, were self-grooming, digging, and inactive using definitions from a prior study. [71]. Behaviors were coded for the percent of time spent performing that behavior and the number of bouts.

5.6.4 Attentional set-shifting task and apparatus

5.6.4.1 Apparatus and stimuli

A Plexiglas box (50 x 37.5 x 25 cm) with a black divider was used as the testing arena. The sliding door allowed access to the flowerpot. All media stimuli were mixed and recycled between rats to allow any odor cues to be disseminated. However, once a pot had been scented with the blotting paper it was only ever scented with the same scent. Crushed Honey Nut Cheerio powder was applied to all digging media to prevent reward odor from serving as a digging cue. Media were shredded manila folders, aspen shavings, foam rubber, felt, burlap ribbon, silk ribbon, plastic beads, plastic jewels, cloth string, wire string, cigarette filters, and shredded cotton pads. Odors were rum, vanilla, lemon, almond, cinnamon, anise, watermelon, grapefruit, strawberry, blueberry, marjoram, and cumin. A pilot study demonstrated that rats could discriminate these odors.

5.6.4.2 Training

For the set-shifting task rats were given basic digging training with plain bedding for 1-2 days. Basic training consisted of shaping digging behavior in the testing arena. Rats were allowed to obtain a small 1/3 piece of cereal on top of the bedding of the flowerpots. During successive trials the cereal was buried deeper until the rat was successfully digging to retrieve it at about 3.5 cm deep. Then 1-2 days of training to learn with one odor pair (tea tree oil vs lavender) and one media pair (shredded paper vs pine shavings) with unscented pots. Since prior work has found that adolescent rats were impaired on the CD phase50, compared to adults, basic training was extended to ensure rats could complete the full set-shifting task. After reaching 7 correct trials on the odor and media pairs they performed the full set-shifting task the next day on PND 37-40. All rats that completed the set-shifting task were euthanized on PND 39-40. Honey

Nut Cheerios (General Mills, MN) and a flowerpot were introduced into the home cage the night before training began. Pots themselves were not scented, rather blotting paper was taped to the inner lip of the ceramic pot and scented with a pipettor (2.5 microliters). The paper was re-scented before every training session.

5.6.4.3 Set-shifting task

Rats were trained in the set-shifting task with 7 stages: compound discrimination (CD), intra-dimensional shift 1-4 (ID), extra-dimensional shift (ED), and a (simple discrimination (SD). The SD was included as a control, and no condition differences were expected. Rats underwent food restriction for around 7 days, obtaining around 90% of their body weight.

Table 4 Set-shifting task with an example of media and odor pairings for a sample rat. Half the rats were rewarded for odor cues then shifted to media cues and half the rats were rewarded for media and then shifted to odor cues.

Phase	CD	ID1	ID2	ID3	ID4	ED	SD
Example rat	**Marjoram**/Cloth pads vs Cumin/Cigarette filters	**Rum**/aspen vs Vanilla/ Shredded manilla folders	**Strawberry** /Cloth string vs Blueberry/ Wire string	**Cinnamon**/Felt vs Anise/Foam rubber	**Watermelon** /Wood beads vs Grapefruit/ Glass beads	Beads/Lemon vs Jewels/ Almond	Ribbon vs Burlap
CD-Compound discrimination, ID1-4=Intradimensional shift, ED- Extradimensional shift, SD-Simple discrimination							
Bolded item indicates rewarded and correct choice. (Note: For any phase of the task there is another pairing of pots to offer all combinations. For example, for the CD (Cumin/Cloth pads vs Marjoram/ Cigarette filters) would be offered.)							

In all sessions the first four trials were discovery trials; the rat could sample the other pot in these trials only. After these trials, once the rat initiated a dig (defined as moving the medium with nose or paw), it was scored, and rats were allowed to finish digging in incorrect pots but not allowed to go back to the correct pot. After reaching criterion on the basic digging training, rats

completed the set-shifting task CD, ID 1-4, ED, and SD phases. Trials to criterion was set to 7 trials as the subjects were adolescents.[72] Discovery trials were included in the 7 trials to criterion. All stimuli were counterbalanced with a Latin square design and half of the rats were trained odor to medium shifts, half medium to odor shifts, Table 4.

5.6.4.4 MRI volumetric measurements

Volumetric measurements were collected via magnetic resonance imaging (MRI) with a Bruker 600 MHz that had a bottom loading probe, 30 mm x 40 mm. They were placed in a flat bottom glass tube and covered with Fomblin (a safe, nontoxic, inert perfluoropolyether oil which is MRI silent and often used to increase signal-to-noise ratios and decrease magnetic susceptibility distortions[73]) and secured with a pronged glass stabilizer specially made to ensure sample position consistency. Scans were be performed with Rapid Acquisition with Refocused Echoes (RARE) pulse sequences in ~1 hour and 45 minutes with one repetition, a repetition time of 2500 ms, echo time of 30.23 ms, and a RARE factor of 16. The pulse sequence used a flip angle of 90°, acquired two averages, with slices acquired in an interlaced pattern. Image resolution was approximately 100 x 100 x 300 μm with matrix sizes, field of view, and number of slices varying according to brain size. The use of Fomblin reduces the prevalence of susceptibility artifacts, which are often present in whole brain *ex vivo* imaging. Additionally, a pronged glass sample holder was made to ensure consistent orientation and sample position throughout imaging as well as between samples. The utilization of adaptable parameters for imaging allows for maximal signal-to-noise and contrast-to-noise ratios dependent upon sample size.

Volume of the medial prefrontal cortex (areas: A32D, A32V) and the anterior cingulate cortex (ACC) (areas: A24a, A24b) from Paxinos and Watson 7th edition were segmented with

ITK SNAP software by blind to condition researchers. The mPFC and ACC were chosen because of their importance to set-shifting performance.[25–27] Segmentation was screened for consistency through a 3-D modeling in ITK-SNAP before evaluation of total volume. Each ROI was outlined based on anatomical landmarks and the volume for each lobule and frontal region was measured.

5.6.4.5 Data analysis

Behavioral data for set-shifting was separated by sex based on prior research findings.[35] Trials to criterion data were analyzed with a repeated measure ANOVA (phase-repeated measure) x condition as the between-subject factor followed by LSD posthocs after a significant interaction. Behaviors coded by reviewer's blind to condition during the marble bury task included digging, inactive time, grooming, exploring, and marble interaction time. They were analyzed with 2-way ANOVAs (Condition x Sex). Brain volumes were separated by sex and examined with unpaired one-tailed t-tests based on the prior prediction of enlarged frontal cortex occurring in the treatment group.

5.7 References

1. Demetriou EA, Lampit A, Quintana DS, et al. Autism spectrum disorders: a meta-analysis of executive function. *Molecular psychiatry*. Published online 2017. doi:10.1038/mp.2017.75 [doi]

2. Ozonoff S, Pennington BF, Rogers SJ. Executive function deficits in high-functioning autistic individuals: relationship to theory of mind. *Journal of child psychology and psychiatry, and allied disciplines*. 1991;32(7):1081-1106.

3. Hughes C, Russell J, Robbins TW. Evidence for executive dysfunction in autism. *Neuropsychologia*. 1994;32(4):477-493. doi:0028-3932(94)90092-2 [pii]

4. Lai MC, Lombardo M V., Pasco G, et al. A behavioral comparison of male and female adults with high functioning autism spectrum conditions. *PLoS ONE*. 2011;6(6). doi:10.1371/journal.pone.0020835

5. Chen C, Van Horn JD. Developmental neurogenetics and multimodal neuroimaging of sex differences in autism. *Brain Imaging and Behavior*. 2017;11(1):38-61. doi:10.1007/s11682-015-9504-3

6. Memari AH, Ziaee V, Shayestehfar M, Ghanouni P, Mansournia MA, Moshayedi P. Cognitive flexibility impairments in children with autism spectrum disorders: Links to age, gender and child outcomes. *Research in Developmental Disabilities*. 2013;34(10):3218-3225. doi:10.1016/j.ridd.2013.06.033

7. Mabunga DF, Gonzales EL, Kim JW, Kim KC, Shin CY. Exploring the Validity of Valproic Acid Animal Model of Autism. *Experimental neurobiology*. 2015;24(4):285-301. doi:10.5607/en.2015.24.4.285 [doi]

8. Kim KC, Kim P, Go HS, et al. The critical period of valproate exposure to induce autistic symptoms in Sprague-Dawley rats. *Toxicology letters*. 2011;201(2):137-143. doi:10.1016/j.toxlet.2010.12.018 [doi]

9. Kerr DM, Downey L, Conboy M, Finn DP, Roche M. Alterations in the endocannabinoid system in the rat valproic acid model of autism. *Behavioural brain research*. 2013;249:124-133. doi:10.1016/j.bbr.2013.04.043 [doi]

10. Edalatmanesh MA, Nikfarjam H, Vafaee F, Moghadas M. Increased hippocampal cell density and enhanced spatial memory in the valproic acid rat model of autism. *Brain research*. 2013;1526:15-26. doi:10.1016/j.brainres.2013.06.024 [doi]

11. Schneider T, Przewlocki R. Behavioral alterations in rats prenatally exposed to valproic acid: animal model of autism. *Neuropsychopharmacology : official publication of the American College of Neuropsychopharmacology*. 2005;30(1):80-90. doi:10.1038/sj.npp.1300518 [doi]

12. Markram K, Rinaldi T, La Mendola D, Sandi C, Markram H. Abnormal fear conditioning and amygdala processing in an animal model of autism. *Neuropsychopharmacology : official publication of the American College of Neuropsychopharmacology*. 2008;33(4):901-913. doi:1301453 [pii]

13. Nicolini C, Fahnestock M. The valproic acid-induced rodent model of autism. *Experimental neurology*. Published online 2017. doi:S0014-4886(17)30110-3 [pii]

14. Tartaglione AM, Schiavi S, Calamandrei G, Trezza V. Prenatal valproate in rodents as a tool to understand the neural underpinnings of social dysfunctions in autism spectrum disorder. *Neuropharmacology*. 2019;159(January):107477. doi:10.1016/j.neuropharm.2018.12.024

15. Chomiak T, Turner N, Hu B. What We Have Learned about Autism Spectrum Disorder from Valproic Acid. *Pathology research international*. 2013;2013:712758. doi:10.1155/2013/712758 [doi]

16. Christensen J, Gronborg TK, Sorensen MJ, et al. Prenatal valproate exposure and risk of autism spectrum disorders and childhood autism. *Jama*. 2013;309(16):1696-1704. doi:10.1001/jama.2013.2270 [doi]

17. Dean JC, Hailey H, Moore SJ, Lloyd DJ, Turnpenny PD, Little J. Long term health and neurodevelopment in children exposed to antiepileptic drugs before birth. *Journal of medical genetics*. 2002;39(4):251-260.

18. Modabbernia A, Velthorst E, Reichenberg A. Environmental risk factors for autism: an evidence-based review of systematic reviews and meta-analyses. *Molecular Autism*. 2017;8(1):1-16. doi:10.1186/s13229-017-0121-4

19. Deng W, Zou X, Deng H, et al. The Relationship among Genetic Heritability, Environmental Effects, and Autism Spectrum Disorders. *Journal of Child Neurology*. 2015;30(13):1794-1799. doi:10.1177/0883073815580645

20. Hallmayer J, Cleveland S, Torres A, et al. Genetic heritability and shared environmental factors among twin pairs with autism. *Archives of General Psychiatry*. 2011;68(11):1095-1102. doi:10.1001/archgenpsychiatry.2011.76

21. Owen, Adrian M, Roberts AC, Poley CE, Sahakian BJ RT. VERSUS INTRA-DIMENSIONAL SET SHIFTING PERFORMANCE FOLLOWING FRONTAL LOBE EXCISIONS , TEMPORAL LOBE EXCISIONS OR AMYGDALO-HIPPOCAMPECTOMY IN MAN. *Neuropsychologia*. 1991;29(10):993-1006.

22. Chase EA, Tait DS, Brown VJ. Lesions of the orbital prefrontal cortex impair the formation of attentional set in rats. *The European journal of neuroscience*. 2012;36(3):2368-2376. doi:10.1111/j.1460-9568.2012.08141.x [doi]

23. Lindgren HS, Wickens R, Tait DS, Brown VJ, Dunnett SB. Lesions of the dorsomedial striatum impair formation of attentional set in rats. *Neuropharmacology*. 2013;71:148-154. doi:10.1016/j.neuropharm.2013.03.034 [doi]

24. Tait DS, Bowman EM, Neuwirth LS, Brown VJ. Assessment of intradimensional/extradimensional attentional set-shifting in rats. *Neuroscience and biobehavioral reviews*. 2018;89:72-85. doi:S0149-7634(17)30751-0 [pii]

25. Birrell JM, Brown VJ. Medial frontal cortex mediates perceptual attentional set shifting in the rat. *The Journal of neuroscience : the official journal of the Society for Neuroscience*. 2000;20(11):4320-4325. doi:20/11/4320 [pii]

26. Bubb EJ, Aggleton JP, Mara SMO, Nelson AJD. ORIGINAL ARTICLE Chemogenetics Reveal an Anterior Cingulate–Thalamic Pathway for Attending to Task-Relevant Information. *Cerebral Cortex*. Published online 2020:1-18. doi:10.1093/cercor/bhaa353

27. Ng CW, Noblejas MI, Rodefer JS, Smith CB, Poremba A. Double dissociation of attentional resources: prefrontal versus cingulate cortices. *The Journal of neuroscience : the official journal of the Society for Neuroscience*. 2007;27(45):12123-12132. doi:27/45/12123 [pii]

28. Memari AH, Ziaee V, Shayestehfar M, Ghanouni P, Mansournia MA, Moshayedi P. Cognitive flexibility impairments in children with autism spectrum disorders: links to age, gender and child outcomes. *Research in developmental disabilities*. 2013;34(10):3218-3226. doi:10.1016/j.ridd.2013.06.033 [doi]

29. Hjelmquist E. Nydn2000. 2000;185:180-185.

30. Lemon JM, Gargaro B, Enticott PG, Rinehart NJ. Brief report: Executive functioning in autism spectrum disorders: A gender comparison of response inhibition. *Journal of Autism and Developmental Disorders*. 2011;41(3):352-356. doi:10.1007/s10803-010-1039-2

31. Kiep M, Spek AA. Executive functioning in men and women with an autism spectrum disorder. *Autism Research*. 2017;10(5):940-948. doi:10.1002/aur.1721

32. White EI, Wallace GL, Bascom J, et al. Sex differences in parent-reported executive functioning and adaptive behavior in children and young adults with autism spectrum disorder. *Autism Research*. 2017;10(10):1653-1662. doi:10.1002/aur.1811

33. Baio J, Wiggins L, Christensen DL, et al. Prevalence of Autism Spectrum Disorder Among Children Aged 8 Years - Autism and Developmental Disabilities Monitoring Network, 11 Sites, United States, 2014. *Morbidity and mortality weekly reportSurveillance summaries (Washington, DC: 2002)*. 2018;67(6):1-24. doi:10.15585/mmwr.ss6706a1 [doi]

34. Halladay AK, Bishop S, Constantino JN, et al. Sex and gender differences in autism spectrum disorder: Summarizing evidence gaps and identifying emerging areas of priority. *Molecular Autism*. 2015;6(1):1-5. doi:10.1186/s13229-015-0019-y

35. McKinnell ZE, Maze T, Ramos A, Challans B, Plakke B. Valproic acid treated female Long-Evans rats are impaired on attentional set-shifting. *Behavioural brain research*. 2021;397:112966. doi:10.1016/j.bbr.2020.112966

36. Khundrakpam BS, Lewis JD, Kostopoulos P, Carbonell F, Evans AC. Cortical Thickness Abnormalities in Autism Spectrum Disorders Through Late Childhood, Adolescence, and Adulthood: A Large-Scale MRI Study. *Cerebral cortex (New York, NY : 1991)*. 2017;27(3):1721-1731. doi:10.1093/cercor/bhx038

37. Courchesne E, Pramparo T, Gazestani VH, Lombardo M V., Pierce K, Lewis NE. The ASD Living Biology: from cell proliferation to clinical phenotype. *Molecular Psychiatry*. 2019;24(1):88-107. doi:10.1038/s41380-018-0056-y

38. Van Rooij D, Anagnostou E, Arango C, et al. Cortical and subcortical brain morphometry differences between patients with autism spectrum disorder and healthy individuals across the lifespan: Results from the ENIGMA ASD working group. *American Journal of Psychiatry*. 2018;175(4):359-369. doi:10.1176/appi.ajp.2017.17010100

39. Braden BB, Riecken C. Thinning faster? Age-related cortical thickness differences in adults with autism spectrum disorder. *Research in Autism Spectrum Disorders*. 2019;64(February):31-38. doi:10.1016/j.rasd.2019.03.005

40. Laidi C, Boisgontier J, de Pierrefeu A, et al. Decreased Cortical Thickness in the Anterior Cingulate Cortex in Adults with Autism. *Journal of Autism and Developmental Disorders*. 2019;49(4):1402-1409. doi:10.1007/s10803-018-3807-3

41. Mensen VT, Wierenga LM, van Dijk S, et al. Development of cortical thickness and surface area in autism spectrum disorder. *NeuroImage: Clinical*. 2017;13:215-222. doi:10.1016/j.nicl.2016.12.003

42. Lauber E, Filice F, Schwaller B. Prenatal valproate exposure differentially affects parvalbumin-expressing neurons and related circuits in the cortex and striatum of mice. *Frontiers in Molecular Neuroscience*. 2016;9(DEC2016):1-16. doi:10.3389/fnmol.2016.00150

43. Rinaldi T, Silberberg G, Markram H. Hyperconnectivity of local neocortical microcircuitry induced by prenatal exposure to valproic acid. *Cerebral cortex (New York, NY: 1991)*. 2008;18(4):763-771. doi:bhm117 [pii]

44. Yerys BE, Wallace GL, Harrison B, Celano MJ, Giedd JN, Kenworthy LE. Set-shifting in children with autism spectrum disorders: reversal shifting deficits on the Intradimensional/Extradimensional Shift Test correlate with repetitive behaviors. *Autism : the international journal of research and practice*. 2009;13(5):523-539. doi:10.1177/1362361309335716 [doi]

45. Reed P, Watts H, Truzoli R. Flexibility in young people with autism spectrum disorders on a card sort task. *Autism : the international journal of research and practice*. 2013;17(2):162-172. doi:10.1177/1362361311409599 [doi]

46. Postema MC, van Rooij D, Anagnostou E, et al. Altered structural brain asymmetry in autism spectrum disorder in a study of 54 datasets. *Nature communications*. 2019;10(1):4958. doi:10.1038/s41467-019-13005-8

47. Wright NF, Vann SD, Aggleton JP, Nelson AJ. A critical role for the anterior thalamus in directing attention to task-relevant stimuli. *The Journal of neuroscience : the official journal of the Society for Neuroscience*. 2015;35(14):5480-5489. doi:10.1523/JNEUROSCI.4945-14.2015 [doi]

48. McKinnell ZE, Maze T, Ramos A, Challans B, Plakke B. Valproic acid treated female Long-Evans rats are impaired on attentional set-shifting. *Behavioural brain research*. 2020;397:112966. doi:10.1016/j.bbr.2020.112966

49. Uddin LQ, Menon V, Young CB, et al. Multivariate searchlight classification of structural magnetic resonance imaging in children and adolescents with autism. *Biological Psychiatry*. 2011;70(9):833-841. doi:10.1016/j.biopsych.2011.07.014

50. Newman LA, Mcgaughy J. Adolescent rats show cognitive rigidity in a test of attentional set shifting. *Developmental Psychobiology*. 2011;53(4):391-401. doi:10.1002/dev.20537

51. de Giambattista C, Ventura P, Trerotoli P, Margari F, Margari L. Sex Differences in Autism Spectrum Disorder: Focus on High Functioning Children and Adolescents. *Frontiers in Psychiatry*. 2021;12(July):1-13. doi:10.3389/fpsyt.2021.539835

52. Rynkiewicz A, Lucka I. Autism spectrum disorder (ASD) in girls. Co-occurring psychopathology. Sex differences in clinical manifestation. *Psychiatria Polska*. 2018;52(4):629-639. doi:10.12740/PP/ONLINEFIRST/58837

53. Tavares V, Fernandes LA, Antunes M, Ferreira H, Prata D. Sex Differences in Functional Connectivity Between Resting State Brain Networks in Autism Spectrum Disorder. *Journal of Autism and Developmental Disorders*. Published online 2021. doi:10.1007/s10803-021-05191-6

54. Cauvet É, Van'T Westeinde A, Toro R, et al. Sex differences along the autism continuum: A twin study of brain structure. *Cerebral Cortex*. 2019;29(3):1342-1350. doi:10.1093/cercor/bhy303

55. Lawrence KE, Hernandez LM, Bowman HC, et al. Sex differences in functional connectivity of the salience, default mode, and central executive networks in youth with asd. *Cerebral Cortex*. 2020;30(9):5107-5120. doi:10.1093/cercor/bhaa105

56. Payne M, Mali I, McKinnell ZE, et al. Increased volumes of lobule VI in a valproic acid model of autism are associated with worse set-shifting performance in male Long-Evan rats. *Brain research*. 2021;1765(April):147495. doi:10.1016/j.brainres.2021.147495

57. Coffman KA, Dum RP, Strick PL. Cerebellar vermis is a target of projections from the motor areas in the cerebral cortex. *Proceedings of the National Academy of Sciences of the United States of America*. 2011;108(38):16068-16073. doi:10.1073/pnas.1107904108

58. Agam Y, Joseph RM, Barton JJ, Manoach DS. Reduced cognitive control of response inhibition by the anterior cingulate cortex in autism spectrum disorders. *NeuroImage*. 2010;52(1):336-348. doi:10.1016/j.neuroimage.2010.04.010 [doi]

59. Barttfeld P, Wicker B, Cukier S, et al. State-dependent changes of connectivity patterns and functional brain network topology in autism spectrum disorder. *Neuropsychologia*. 2012;50(14):3653-3662. doi:10.1016/j.neuropsychologia.2012.09.047

60. Schmitz N, Rubia K, Daly E, Smith A, Williams S, Murphy DG. Neural correlates of executive function in autistic spectrum disorders. *Biological psychiatry*. 2006;59(1):7-17. doi:S0006-3223(05)00713-4 [pii]

61. Yerys BE, Antezana L, Weinblatt R, et al. Neural Correlates of Set-Shifting in Children With Autism. *Autism research : official journal of the International Society for Autism Research*. 2015;8(4):386-398. doi:10.1002/aur.1454 [doi]

62. Braden BB, Smith CJ, Thompson A, et al. Executive function and functional and structural brain differences in middle-age adults with autism spectrum disorder. *Autism research : official journal of the International Society for Autism Research*. 2017;10(12):1945-1960. doi:10.1002/aur.1842 [doi]

63. Morgan JT, Chana G, Pardo CA, et al. Microglial activation and increased microglial density observed in the dorsolateral prefrontal cortex in autism. *Biological Psychiatry*. 2010;68(4):368-376. doi:10.1016/j.biopsych.2010.05.024

64. Petrelli F, Pucci L, Bezzi P. Astrocytes and microglia and their potential link with autism spectrum disorders. *Frontiers in Cellular Neuroscience*. 2016;10(FEB):1-8. doi:10.3389/fncel.2016.00021

65. Suzuki K, Sugihara G, Ouchi Y, et al. Microglial activation in young adults with autism spectrum disorder. *Archives of General Psychiatry*. 2013;70(1):49-58. doi:10.1001/jamapsychiatry.2013.272

66. Zielinski BA, Prigge MBD, Nielsen JA, et al. Longitudinal changes in cortical thickness in autism and typical development. *Brain*. 2014;137(6):1799-1812. doi:10.1093/brain/awu083

67. Cheadle L, Rivera SA, Phelps JS, et al. Sensory Experience Engages Microglia to Shape Neural Connectivity through a Non-Phagocytic Mechanism. *Neuron*. 2020;108(3):451-468.e9. doi:10.1016/j.neuron.2020.08.002

68. Schuldiner O, Yaron A. Mechanisms of developmental neurite pruning. *Cellular and Molecular Life Sciences*. 2015;72(1):101-119. doi:10.1007/s00018-014-1729-6

69. Andropoulos DB. Effect of Anesthesia on the Developing Brain : Infant and Fetus. 2018;77030:1-11. doi:10.1159/000475928

70. Lazic SE, Essioux L. Improving basic and translational science by accounting for litter-to-litter variation in animal models. *BMC Neuroscience*. 2013;14. doi:10.1186/1471-2202-14-37

71. Ku KM, Weir RK, Silverman JL, Berman RF, Bauman MD. Behavioral phenotyping of juvenile long-evans and sprague-dawley rats: Implications for preclinical models of autism spectrum disorders. *PLoS ONE*. 2016;11(6):1-25. doi:10.1371/journal.pone.0158150

72. Cain RE, Wasserman MC, Waterhouse BD, McGaughy JA. Atomoxetine facilitates attentional set shifting in adolescent rats. *Developmental cognitive neuroscience*. 2011;1(4):552-560. doi:10.1016/j.dcn.2011.04.003 [doi]

73. Li R, Liu X, Sidabras JW, et al. Restoring susceptibility induced MRI signal loss in rat brain at 9.4 T: A step towards whole brain functional connectivity imaging. *PLoS ONE*. 2015;10(4). doi:10.1371/journal.pone.0119450

Chapter 6 - Summary and Future Outlook

While MRI scanners of low field strength are still being used in clinical studies, the use of high field scanners in preclinical studies have opened a new realm of possibilities for medical applications. With high field strength comes high signal-to-noise ratio, high-resolution, and short scan times. This study uses an ultra-high-field scanner of 14.1 T for imaging cell lines, excised tissues, and small animals. High-resolution *in vivo* MR images of mouse models of PDACs were acquired for longitudinal monitoring of the orthotopic tumors. For most advanced tumors, surgery is the ultimate choice of treatment although it is accompanied by many complications. In our study, we demonstrate the efficacy of a non-invasive image-guided thermal therapy platform on mouse models of solid tumors (**Chapter 2**). Thermal treatments use temperatures above physiological temperature to destroy cancer cells. We used two different mouse models of solid tumors (KPC mouse models of PDAC and HAC15 mouse model of adrenal adenoma). From the thermometry results, four out of the six HAC15 mice had more than 90% of the tumor volume heated. Moreover, we observed increase in T1 relaxation values after application of thermal therapies on tumor tissues, whereas the values remained fairly constant for normal tissues. Future studies should use a larger sample size and strategies to reduce motion-related artifacts.

One of the objectives of this study was to demonstrate the feasibility of performing proton MRS using ultra-high field scanner and optimized pulse sequences. We utilized a 10 mm diameter imaging coil to perform ^{1}H-MRS experiments on five cell lines and excised tumor tissues from mice and human subjects (**Chapter 3**). Using a smaller imaging coil increases the SNR, allows for smaller voxel sizes, and eliminate noise from between the coil and the sample. A PRESS pulse sequence was optimized using different TE and TRs to acquire signals from major metabolites. To homogenize the B_0, appropriate voxel specific shimming procedures were

run. Furthermore, VAPOR water suppression and outer volume suppression were applied to visualize the metabolites better. Signals from lipid, lactate, N-acetyl aspartate, creatine, choline, glutamate/glutamine, and inositol were detected. We used an external software (Chenomx) to correct phase and baseline related distortions in the spectra. Based on our results, short TE was found most effective in acquiring signal from most metabolites. One major limitation of this study is that it lacks quantitative analysis. Unlike MRI, MRS lacks robust processing and analysis tools. LCModel and jMRUI are two software packages mostly used to quantify ^{1}H-MRS data. However, they lack user friendliness and require simulation of basis sets depending on the parameters used during the study. Future studies will test different software and pipelines to acquire absolute concentrations of the metabolites.

Another aim of this study was to use high-resolution MRI in studying autism spectrum disorder. MRI based volumetric studies in small animals is challenging due to low spatial resolution which causes difficulty in delineating and segmenting specific regions. In this study (**Chapter 4 and Chapter 5**), we used a VPA model of ASD in rodents. With the use of ultra-high-field MRI and RARE pulse sequences, we acquired high-resolution 3D MRI scans of rat cerebellums and whole brains. This allowed for accurate segmentation across specific regions of the cerebellum and whole brains. Use of fomblin for whole brain *ex vivo* imaging helped in reducing susceptibility artifacts arising from the aural cavity. The volumetric analysis of cerebellar regions in VPA rats demonstrated impact in ASST performance. VPA adult male and female rats had increased and decreased cerebellar lobule VI volume respectively and this was associated with impaired performance. VPA adolescent female rats had enlarged frontal cortices, and this was associated with impaired set-shifting task. Structural MRI studies can help understand the role of brain volumes in ASD. However, it is important to study the underlying

pathophysiology in finding effective biomarkers linked to ASD. A method is under development to acquire high-resolution ^{1}H-MRS from VPA and control rats to study metabolic changes associated to ASD. An example for ^{1}H-MRS acquired from the caudate region of a rat brain *ex vivo* is shown in **Figure 6.18**.

Appendix A - Supporting information for Chapter 2

Table 5 MRI thermometry data. Achieved coverage of tumor by thermal dose of at least 240 CEM43 and maximum estimated temperature in tumor for 5 out of 6 mice. In 1 mouse, thermometry data were unusable because of excessive sample movement. V_{tumor}, volume of tumor; V_{cov}, volume of tumor encompassed by the threshold ablative thermal dose of 240 CEM43; T_{max}, maximum achieved temperature in tissue as estimated by MRI thermometry. Adapted with permission from Sebek, J., Shrestha, T. B., Basel, M. T., Chamani, F., Zeinali, N., **Mali, I**., Payne, M., Timmerman, S. A., Faridi, P., Pyle, M., O'Halloran, M., Dennedy, M. C., Bossmann, S. H., & Prakash, P. (2022). System for delivering microwave ablation to subcutaneous tumors in small-animals under high-field MRI thermometry guidance. *International Journal of Hyperthermia*, *39*(1), 584–594.

Mouse	V_{tumor} [mm^3]	V_{cov} [mm^3]	V_{cov}/V_{tumor} [%]	T_{max} [°C]	Heating time [s]
1	9.06	0	0	50.5	259
2	12.46	11.81	94.71	70	103
3	35.92	22.02	61.31	66.5	150
4	8.29	7.52	90.73	59	134
5	5.43	5.32	97.98	67.5	135

A

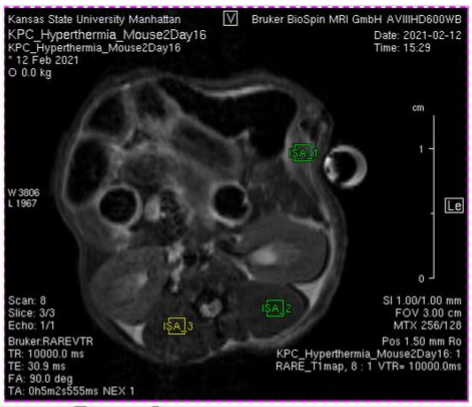

B

ROI name	ISA_1			ISA_2			ISA_3		
ROI area	0.0181 cm2			0.0181 cm2			0.0181 cm2		
parameter	value	std dev	usage	value	std dev	usage	value	std dev	usage
absolute bias	0	0	fixed	0	0	fixed	0	0	fixed
signal intensity	8.27475	0.537668	varied	5.07351	0.0513177	varied	5.17529	0.636979	varied
T1 relaxation time [ms]	2617.94	256.748	varied	3176.09	58.4511	varied	3201.69	643.298	varied
std dev of the fit	0.176992			0.0276661			0.242517		
recovery time [msec]	mean	std dev	func	mean	std dev	func	mean	std dev	func
442.15	1.40	0.27	1.29	0.65	0.204705	0.66	0.69	0.33	0.67
884.12	2.37	0.41	2.37	1.22	0.214578	1.23	1.32	0.46	1.25
1452.30	3.57	0.56	3.52	1.85	0.260798	1.86	2.03	0.70	1.89
2248.94	4.31	0.81	4.77	2.64	0.327727	2.57	2.83	0.77	2.61
3592.98	6.14	1.04	6.18	3.42	0.281663	3.44	2.90	0.79	3.49
9942.15	8.39	1.44	8.09	4.85	0.380407	4.85	5.28	1.17	4.94

C

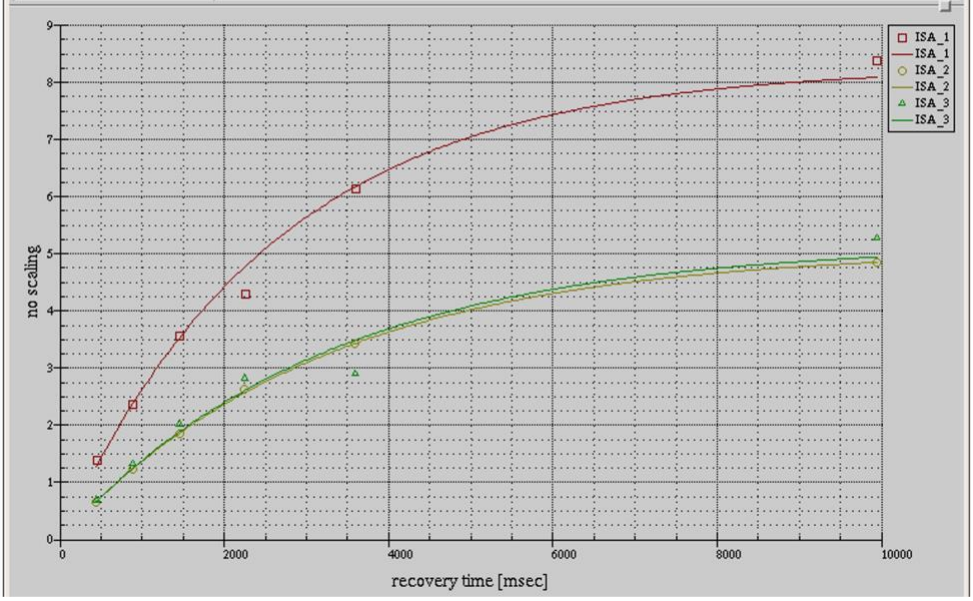

Figure 6.1 T1 relaxation values before mild hyperthermia for mouse 2, day 16 after KPC tumor implantation. (A) T2 RARE image used for ROI placement. ISA 1 is for the region with the tumor; ISA 2 and ISA 3 are for regions outside the tumor. (B) T1 relaxation values shown in msec for each ROI. (C) Representative fit showing different recovery times.

A

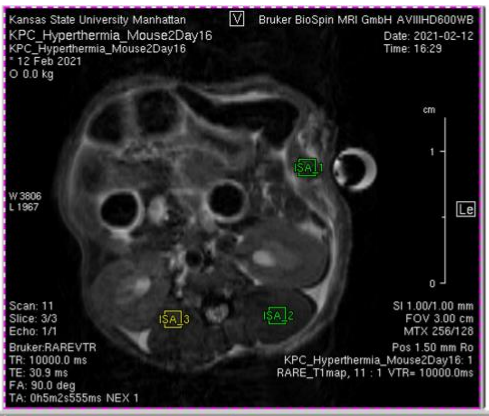

B

ROI name	ISA_1			ISA_2			ISA_3		
ROI area	0.0181 cm2			0.0181 cm2			0.0181 cm2		
parameter	value	std dev	usage	value	std dev	usage	value	std dev	usage
absolute bias	0	0	fixed	0	0	fixed	0	0	fixed
signal intensity	5.82512	0.238663	varied	4.64849	0.47866	varied	5.19666	0.262532	varied
T1 relaxation time [ms]	2732.85	171.175	varied	3151.46	512.946	varied	3188.53	243.772	varied
std dev of the fit	0.0800888			0.181449			0.0813666		
recovery time [msec]	mean	std dev	func	mean	std dev	func	mean	std dev	func
442.15	0.87	0.33	0.87	0.56	0.17213	0.61	0.64	0.23	0.67
884.12	1.71	0.55	1.61	0.91	0.186424	1.14	1.34	0.32	1.26
1452.30	2.26	0.73	2.40	1.81	0.284076	1.72	1.91	0.61	1.90
2248.94	3.26	1.03	3.27	2.53	0.219685	2.37	2.47	0.59	2.63
3592.98	4.30	1.24	4.26	3.26	0.405883	3.16	3.59	0.82	3.51
9942.15	5.68	1.70	5.67	4.27	0.517725	4.45	4.99	1.10	4.97

C

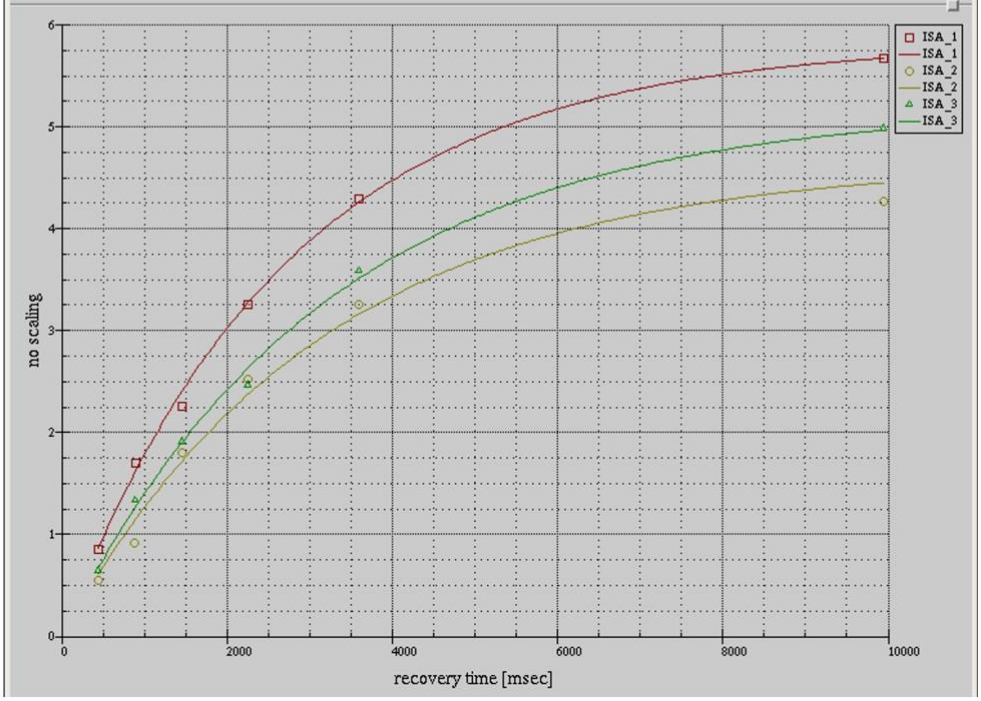

Figure 6.2 T1 relaxation values after mild hyperthermia for mouse 2, day 16 after KPC tumor implantation. (A) T2 RARE image used for ROI placement. ISA 1 is for the region with the tumor; ISA 2 and ISA 3 are for regions outside the tumor. (B) T1 relaxation values shown in msec for each ROI. (C) Representative fit showing different recovery times

A

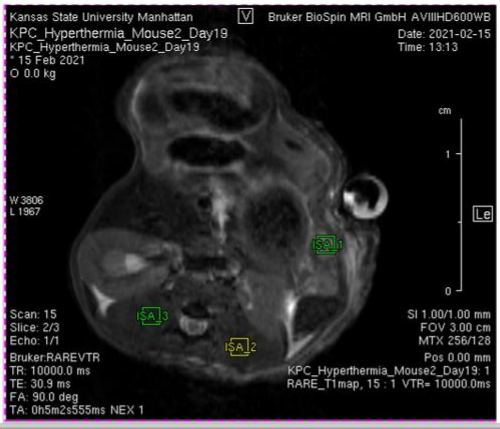

B

ROI name	ISA_1			ISA_2			ISA_3		
ROI area	0.0181 cm2			0.0211 cm2			0.0181 cm2		
parameter	value	std dev	usage	value	std dev	usage	value	std dev	usage
absolute bias	0	0	fixed	0	0	fixed	0	0	fixed
signal intensity	10.9039	0.159334	varied	4.48753	0.475286	varied	4.36973	0.22285	varied
T1 relaxation time [ms]	3234.68	73.326	varied	3271.13	542.935	varied	3477.39	289.897	varied
std dev of the fit	0.0536079			0.161016			0.0930942		
recovery time [msec]	mean	std dev	func	mean	std dev	func	mean	std dev	func
442.15	1.40	0.31	1.39	0.63	0.196305	0.57	0.56	0.178134	0.52
884.12	2.63	0.41	2.61	0.93	0.26052	1.06	0.91	0.228077	0.98
1452.30	3.97	0.59	3.94	1.84	0.337335	1.61	1.61	0.277143	1.49
2248.94	5.48	0.71	5.46	2.03	0.439864	2.23	2.00	0.255776	2.08
3592.98	7.16	0.85	7.31	2.97	0.447567	2.99	2.94	0.55946	2.81
9942.15	10.49	1.25	10.40	4.33	0.761643	4.27	4.12	0.463809	4.12

C

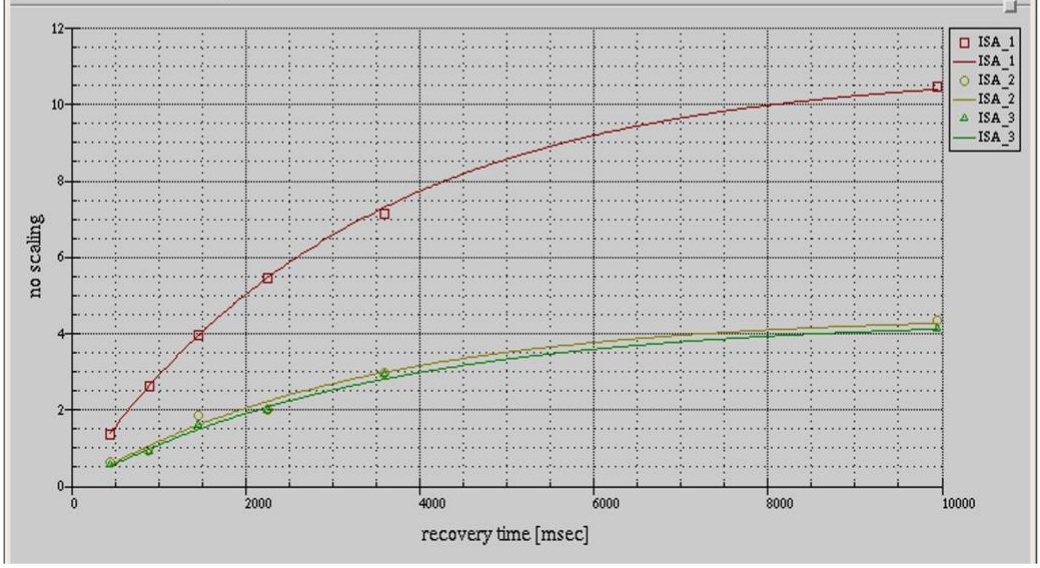

Figure 6.3 T1 relaxation values before mild hyperthermia for mouse 2, day 19 after KPC tumor implantation. (A) T2 RARE image used for ROI placement. ISA 1 is for the region with the tumor; ISA 2 and ISA 3 are for regions outside the tumor. (B) T1 relaxation values shown in msec for each ROI. (C) Representative fit showing different recovery times.

A

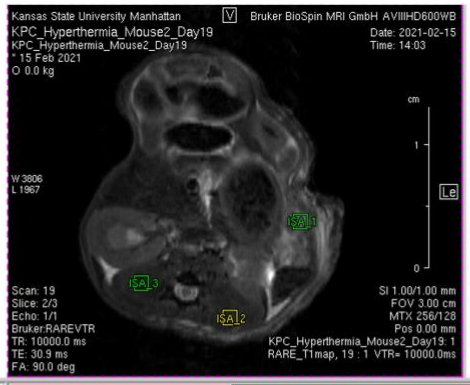

B

ROI name	ISA_1			ISA_2			ISA_3		
ROI area	0.0181 cm2			0.0181 cm2			0.0181 cm2		
parameter	value	std dev	usage	value	std dev	usage	value	std dev	usage
absolute bias	0	0	fixed	0	0	fixed	0	0	fixed
signal intensity	10.6266	0.228691	varied	4.63657	0.263792	varied	3.9329	0.308399	varied
T1 relaxation time [ms]	3330.17	113.463	varied	4229.79	388.726	varied	3536.09	448.542	varied
std dev of the fit	0.0824947			0.0853689			0.120466		
recovery time [msec]	mean	std dev	func	mean	std dev	func	mean	std dev	func
442.15	1.32	0.29	1.32	0.46	0.152786	0.46	0.48	0.165123	0.46
884.12	2.58	0.42	2.48	0.83	0.269036	0.87	1.04	0.243661	0.87
1452.30	3.75	0.54	3.76	1.49	0.28698	1.35	1.35	0.235863	1.32
2248.94	5.07	0.66	5.22	1.77	0.372037	1.91	1.67	0.283273	1.85
3592.98	7.00	0.89	7.01	2.63	0.477833	2.65	2.50	0.411846	2.51
9942.15	10.14	1.06	10.09	4.21	0.509029	4.19	3.76	0.475035	3.70

C

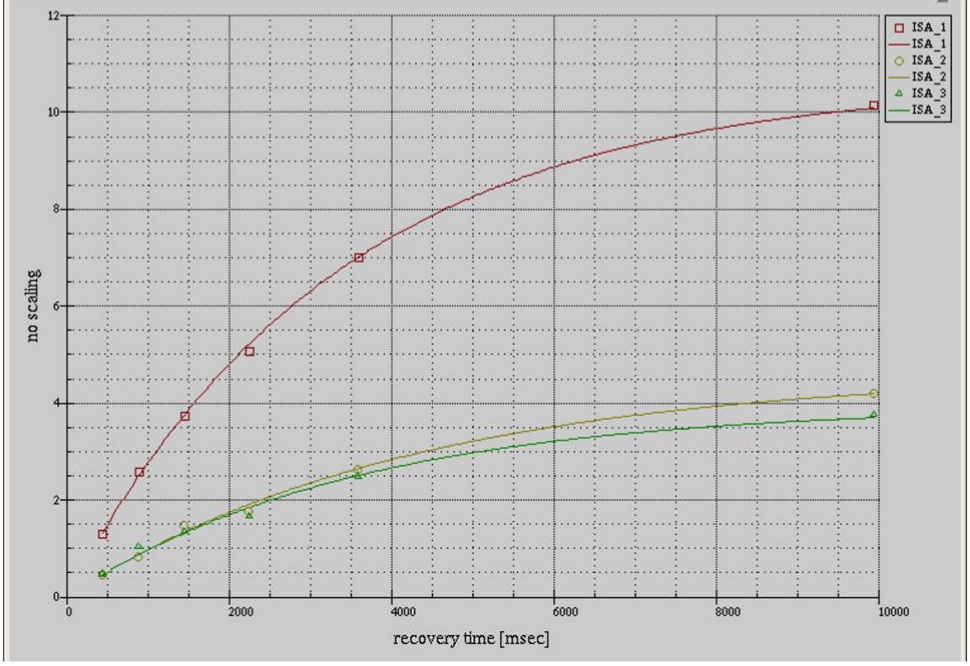

Figure 6.4 T1 relaxation values after mild hyperthermia for mouse 2, day 19 after KPC tumor implantation. (A) T2 RARE image used for ROI placement. ISA 1 is for the region with the tumor; ISA 2 and ISA 3 are for regions outside the tumor. (B) T1 relaxation values shown in msec for each ROI. (C) Representative fit showing different recovery times.

A

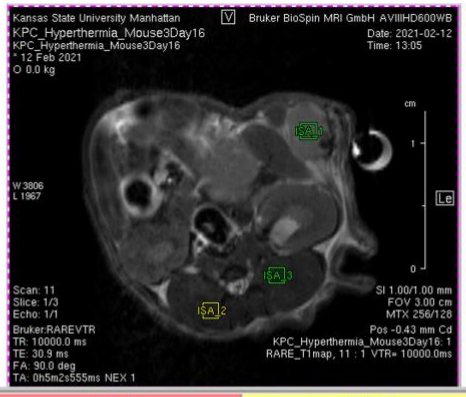

B

ROI name	ISA_1			ISA_2			ISA_3		
ROI area	0.0181 cm2			0.0181 cm2			0.0181 cm2		
parameter	value	std dev	usage	value	std dev	usage	value	std dev	usage
absolute bias	0	0	fixed	0	0	fixed	0	0	fixed
signal intensity	10.6351	0.22294	varied	5.3389	0.21906	varied	5.06621	0.417047	varied
T1 relaxation time [ms]	2852.86	104.887	varied	3164.52	217.443	varied	3349.41	450.419	varied
std dev of the fit	0.114092			0.0983765			0.168628		
recovery time [msec]	mean	std dev	func	mean	std dev	func	mean	std dev	func
442.15	1.57	0.277292	1.56	0.76	0.244485	0.70	0.70	0.210418	0.63
884.12	2.92	0.43956	2.89	1.26	0.282148	1.30	1.21	0.229458	1.18
1452.30	4.50	0.570636	4.32	1.92	0.369676	1.96	1.56	0.276105	1.78
2248.94	5.70	0.592126	5.91	2.90	0.54935	2.72	2.69	0.289924	2.48
3592.98	7.73	0.682663	7.76	3.47	0.613317	3.62	3.20	0.34477	3.33
9942.15	10.56	0.782531	10.50	5.14	0.655136	5.11	4.85	0.534105	4.81

C

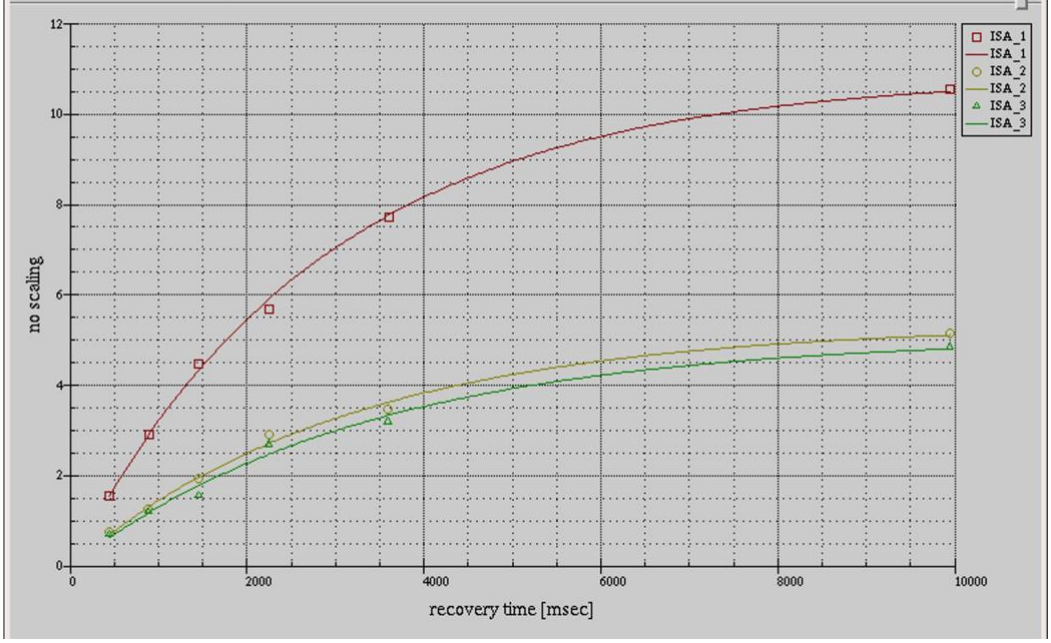

Figure 6.5 T1 relaxation values before mild hyperthermia for mouse 3, day 16 after KPC tumor implantation. (A) T2 RARE image used for ROI placement. ISA 1 is for the region with the tumor; ISA 2 and ISA 3 are for regions outside the tumor. (B) T1 relaxation values shown in msec for each ROI. (C) Representative fit showing different recovery times.

A

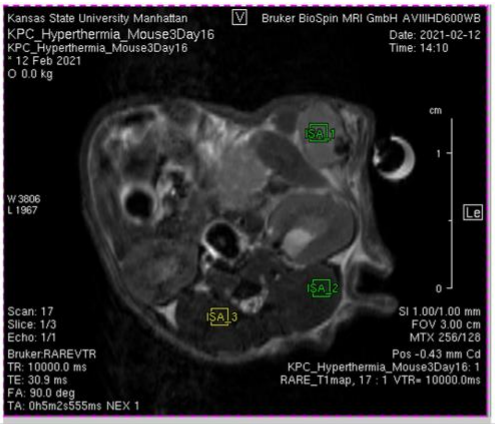

B

ROI name	ISA_1			ISA_2			ISA_3		
ROI area	0.0181 cm2			0.0181 cm2			0.0181 cm2		
parameter	value	std dev	usage	value	std dev	usage	value	std dev	usage
absolute bias	0	0	fixed	0	0	fixed	0	0	fixed
signal intensity	9.88683	0.074004	varied	4.27248	0.0856443	varied	3.92679	0.183794	varied
T1 relaxation time [ms]	3011.71	37.3034	varied	2933.73	102.776	varied	2824.02	227.693	varied
std dev of the fit	0.0328773			0.0433737			0.0910847		
recovery time [msec]	mean	std dev	func	mean	std dev	func	mean	std dev	func
442.15	1.36	0.199372	1.35	0.58	0.227296	0.60	0.57	0.264342	0.57
884.12	2.53	0.193406	2.52	1.17	0.258635	1.11	0.99	0.339068	1.06
1452.30	3.79	0.212904	3.78	1.65	0.340879	1.67	1.68	0.458271	1.58
2248.94	5.16	0.203543	5.20	2.25	0.412017	2.29	2.06	0.48255	2.16
3592.98	6.93	0.292529	6.89	3.01	0.443249	3.02	3.01	0.664239	2.83
9942.15	9.52	0.436554	9.52	4.14	0.543812	4.13	3.75	0.714745	3.81

C

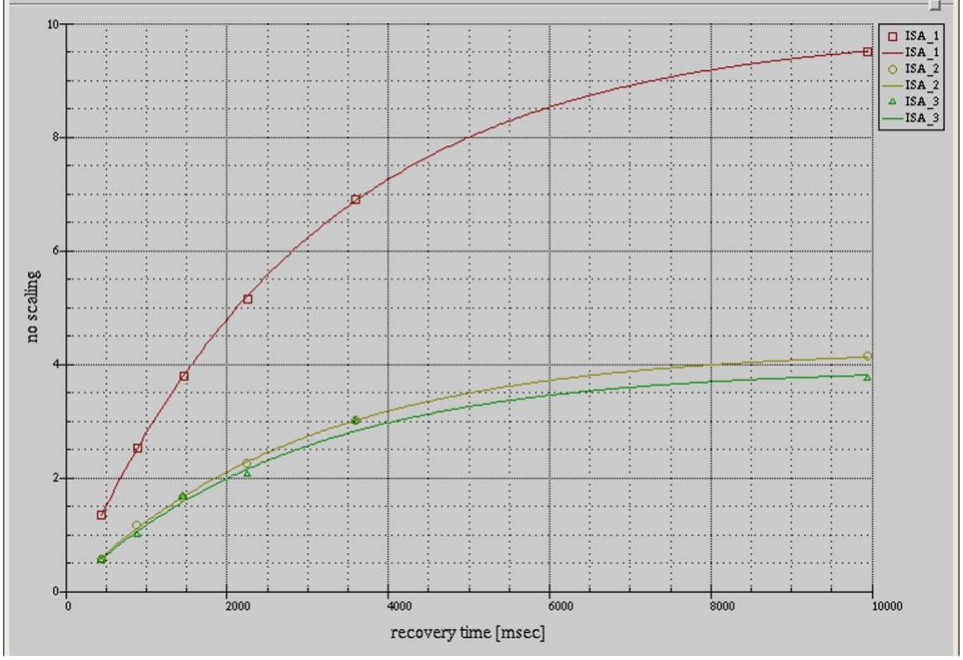

Figure 6.6 T1 relaxation values after mild hyperthermia for mouse 3, day 16 after KPC tumor implantation. (A) T2 RARE image used for ROI placement. ISA 1 is for the region with the tumor; ISA 2 and ISA 3 are for regions outside the tumor. (B) T1 relaxation values shown in msec for each ROI. (C) Representative fit showing different recovery times.

A

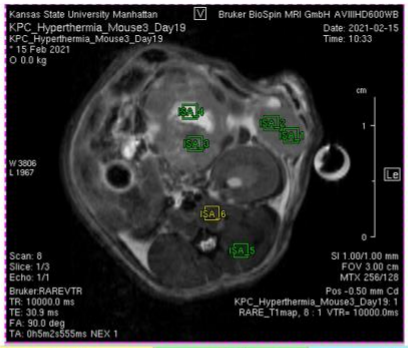

B

ROI name	ISA_1			ISA_2			ISA_3			ISA_4			ISA_5			ISA_6		
ROI area	0.0181 cm2			0.0181 cm2			0.0181 cm2			0.0181 cm2			0.0181 cm2			0.0181 cm2		
parameter	value	std dev	usage	value	std dev	usage	value	std dev	usage	value	std dev	usage	value	std dev	usage	value	std dev	usage
absolute bias	0	0	fixed	0	0	fixed	0	0	fixed	0	0	fixed	0	0	fixed	0	0	fixed
signal intensity	9.22968	0.0421531	varied	9.4442	0.107293	varied	10.4835	0.331588	varied	22.7524	0.632893	varied	4.25473	0.195461	varied	5.11461	0.380215	varied
T1 relaxation time [ms]	3216.45	27.35	varied	3590.12	65.796	varied	3681.49	183.956	varied	4577.12	207.616	varied	2803.08	230.293	varied	3091.91	374.557	varied
std dev of the fit	0.0234375			0.0416286			0.115774			0.228137			0.104281			0.154229		
recovery time [msec]	mean	std dev	func	mean	std dev	func	mean	std dev	func	mean	std dev	func	mean	std dev	func	mean	std dev	func
442.15	1.18	0.167041	1.19	1.06	0.14788	1.09	1.23	0.42	1.19	2.18	0.545825	2.10	0.56	0.166147	0.62	0.62	0.229945	0.68
884.12	2.24	0.219452	2.22	2.09	0.1968	2.06	2.12	0.45	2.24	4.03	0.370871	4.00	1.20	0.214709	1.15	1.39	0.239705	1.27
1452.30	3.31	0.254889	3.35	3.20	0.203501	3.14	3.40	0.73	3.42	6.65	0.666438	6.19	1.66	0.222925	1.72	2.20	0.48379	1.92
2248.94	4.66	0.233439	4.64	4.37	0.200071	4.40	5.01	1.05	4.79	8.60	0.516093	8.83	2.57	0.325116	2.35	2.50	0.285709	2.64
3592.98	6.21	0.226539	6.21	5.95	0.293781	5.97	6.63	1.12	6.53	12.32	0.562407	12.37	3.01	0.287335	3.07	3.48	0.468179	3.51
9942.15	8.81	0.310306	8.81	8.87	0.389099	8.85	9.71	1.31	9.78	20.23	0.814436	20.16	4.13	0.393644	4.13	5.00	0.651971	4.91

C

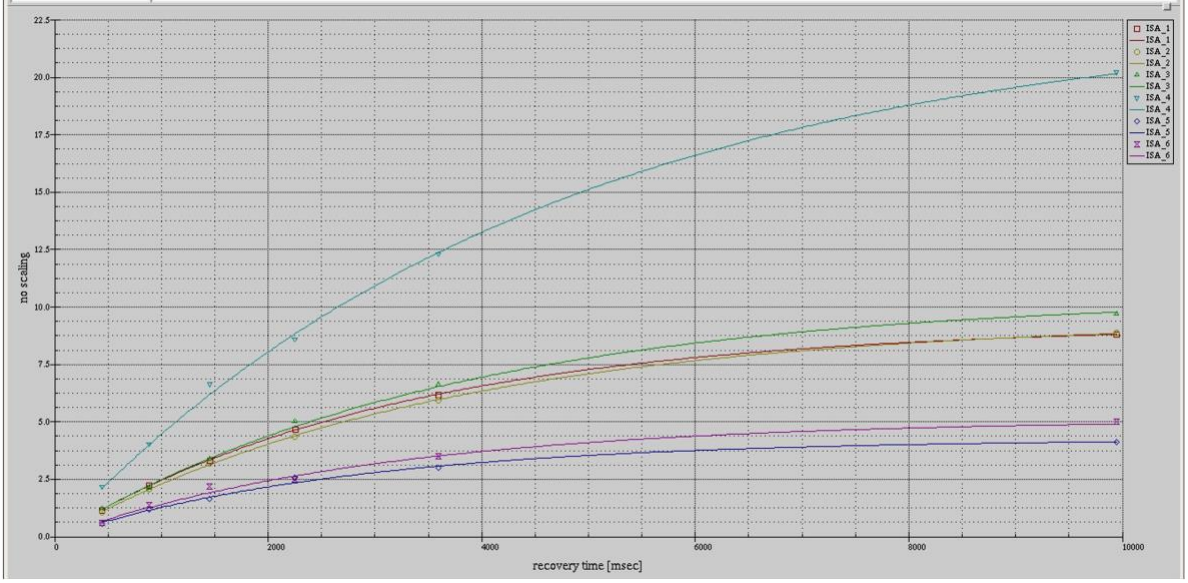

Figure 6.7 T1 relaxation values before mild hyperthermia for mouse 3, day 19 after KPC tumor implantation. (A) T2 RARE image used for ROI placement. ISA 1 is the tumor region closest to the microwave applicator; ISA 2 and ISA 3 are tumor regions away from the microwave applicator. ISA 4 is a fluid filled region suspected to be a cyst. (B) T1 relaxation values shown in msec for each ROI. (C) Representative fit showing different recovery times.

A

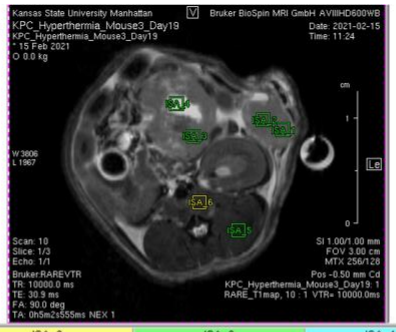

B

ROI name	ISA_1			ISA_2			ISA_3			ISA_4			ISA_5			ISA_6		
ROI area	0.0181 cm2			0.0181 cm2			0.0181 cm2			0.0181 cm2			0.0181 cm2			0.0181 cm2		
parameter	value	std dev	usage	value	std dev	usage	value	std dev	usage	value	std dev	usage	value	std dev	usage	value	std dev	usage
absolute bias	0	0	fixed	0	0	fixed	0	0	fixed	0	0	fixed	0	0	fixed	0	0	fixed
signal intensity	9.47742	0.109612	varied	8.96604	0.148375	varied	9.52841	0.157196	varied	21.7766	1.08642	varied	3.91795	0.244258	varied	4.99931	0.266425	varied
T1 relaxation time [ms]	3324.99	67.3085	varied	3361.22	105.809	varied	3023.06	84.85	varied	4514.81	317.873	varied	2939.81	312.498	varied	3031.28	288.424	varied
std dev of the fit	0.0536107			0.0870461			0.0697911			0.249041			0.115305			0.137615		
recovery time [msec]	mean	std dev	func	mean	std dev	func	mean	std dev	func	mean	std dev	func	mean	std dev	func	mean	std dev	func
442.15	1.16	0.187643	1.18	1.12	0.159084	1.11	1.34	0.222398	1.30	2.12	0.44	2.03	0.62	0.191324	0.55	0.76	0.269912	0.68
884.12	2.27	0.208769	2.21	2.21	0.182605	2.07	2.46	0.369891	2.42	4.09	0.33	3.87	0.86	0.241332	1.02	1.22	0.357354	1.26
1452.30	3.35	0.246052	3.35	3.10	0.201845	3.15	3.62	0.435311	3.63	5.63	0.59	5.99	1.61	0.287299	1.53	1.92	0.391601	1.90
2248.94	4.67	0.308675	4.66	4.35	0.247924	4.37	4.99	0.446314	5.00	8.49	0.55	8.54	2.15	0.311228	2.09	2.75	0.380741	2.62
3592.98	6.17	0.323841	6.26	5.81	0.25708	5.89	6.49	0.556863	6.63	11.73	0.97	11.95	2.71	0.386612	2.76	3.25	0.415435	3.47
9942.15	9.04	0.392535	9.00	8.53	0.26043	8.50	9.26	0.704888	9.17	19.57	1.37	19.37	3.79	0.504439	3.78	4.92	0.593105	4.81

C

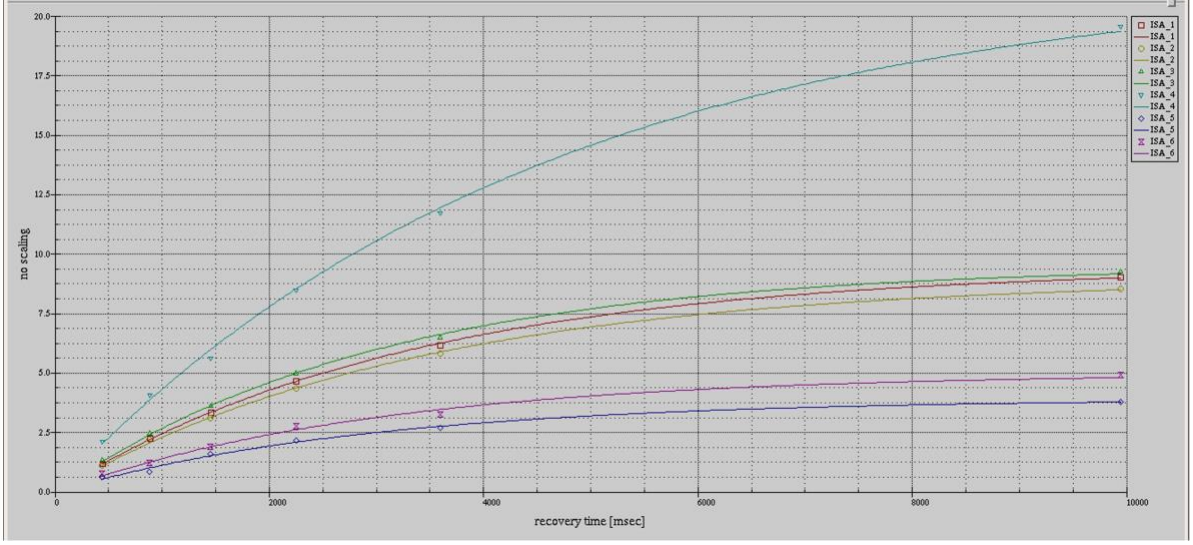

Figure 6.8 T1 relaxation values after mild hyperthermia for mouse 3, day 19 after KPC tumor implantation. (A) T2 RARE image used for ROI placement. ISA 1 is the tumor region closest to the microwave applicator; ISA 2 and ISA 3 are tumor regions away from the microwave applicator. ISA 4 is a fluid filled region suspected to be a cyst. (B) T1 relaxation values shown in msec for each ROI. (C) Representative fit showing different recovery times.

A

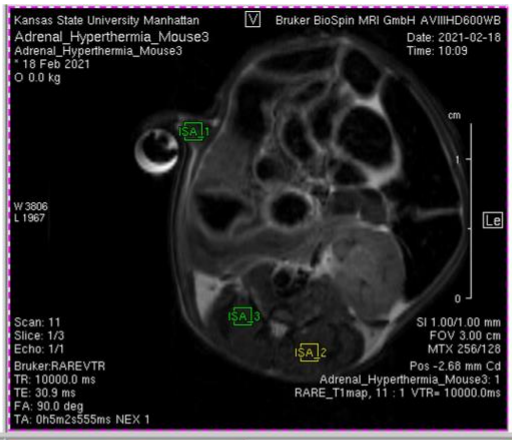

B

ROI name	ISA_1			ISA_2			ISA_3		
ROI area	0.0181 cm2			0.0198 cm2			0.0181 cm2		
parameter	value	std dev	usage	value	std dev	usage	value	std dev	usage
absolute bias	0	0	fixed	0	0	fixed	0	0	fixed
signal intensity	5.86207	0.159291	varied	4.78587	0.279417	varied	5.31234	0.18569	varied
T1 relaxation time [ms]	2357.74	108.096	varied	2718.74	275.71	varied	2846.96	170.983	varied
std dev of the fit	0.0765818			0.148643			0.0999577		
recovery time [msec]	mean	std dev	func	mean	std dev	func	mean	std dev	func
442.15	1.07	0.32	1.00	0.84	0.377547	0.72	0.80	0.235164	0.76
884.12	1.77	0.53	1.83	1.46	0.332399	1.33	1.49	0.18928	1.42
1452.30	2.71	0.70	2.70	1.96	0.400922	1.98	1.99	0.238461	2.12
2248.94	3.57	0.90	3.60	2.49	0.480456	2.69	2.88	0.318863	2.90
3592.98	4.46	1.10	4.58	3.47	0.578828	3.51	3.93	0.438978	3.81
9942.15	5.86	1.19	5.78	4.78	0.740322	4.66	5.14	0.425836	5.15

C

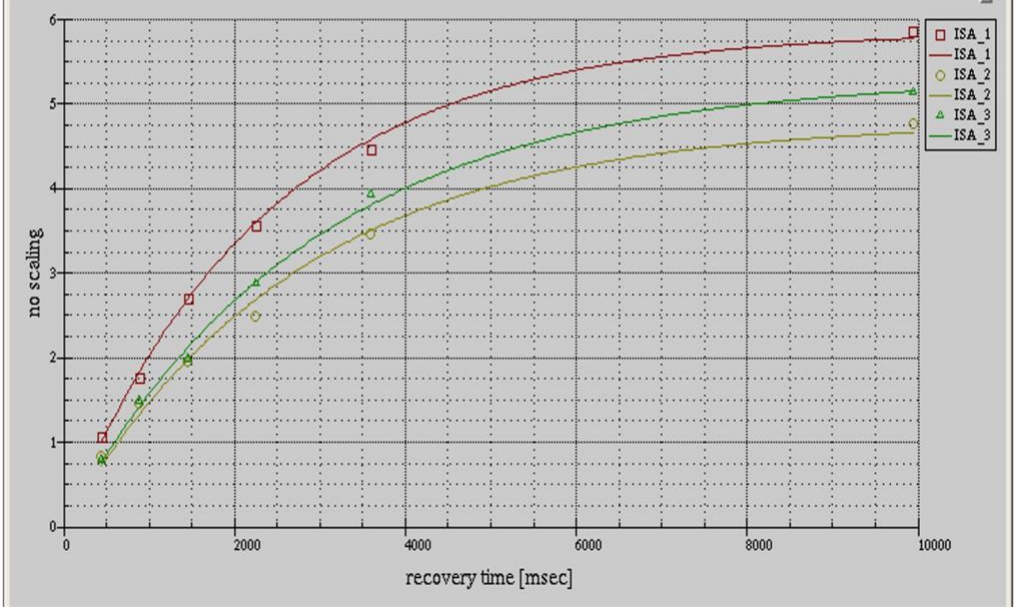

Figure 6.9 T1 relaxation values pre-ablation for mouse 3 with adrenal tumor. (A) T2 RARE image used for ROI placement. ISA 1 is for the region with the tumor; ISA 2 and ISA 3 are for regions outside the tumor. (B) T1 relaxation values shown in msec for each ROI. (C) Representative fit showing different recovery times.

A

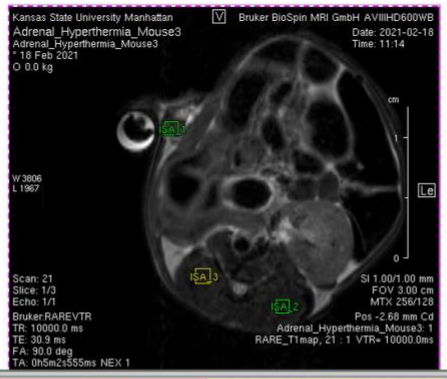

B

ROI name	ISA_1			ISA_2			ISA_3		
ROI area	0.0181 cm2			0.0181 cm2			0.0181 cm2		
parameter	value	std dev	usage	value	std dev	usage	value	std dev	usage
absolute bias	0	0	fixed	0	0	fixed	0	0	fixed
signal intensity	8.31949	0.41441	varied	3.92175	0.456371	varied	4.22172	0.275929	varied
T1 relaxation time [ms]	2632.03	205.134	varied	2957.56	547.789	varied	2750.48	285.91	varied
std dev of the fit	0.134232			0.184414			0.112096		
recovery time [msec]	mean	std dev	func	mean	std dev	func	mean	std dev	func
442.15	1.31	0.41	1.29	0.68	0.239604	0.54	0.59	0.21258	0.63
884.12	2.55	0.74	2.37	0.99	0.388377	1.01	1.28	0.221812	1.16
1452.30	3.50	0.89	3.53	1.56	0.393355	1.52	1.72	0.302765	1.73
2248.94	4.53	1.10	4.76	1.67	0.621265	2.09	2.29	0.34494	2.36
3592.98	6.14	1.18	6.20	2.83	0.989923	2.76	2.87	0.528052	3.08
9942.15	8.44	2.46	8.13	3.90	0.861289	3.79	4.27	0.673533	4.11

C

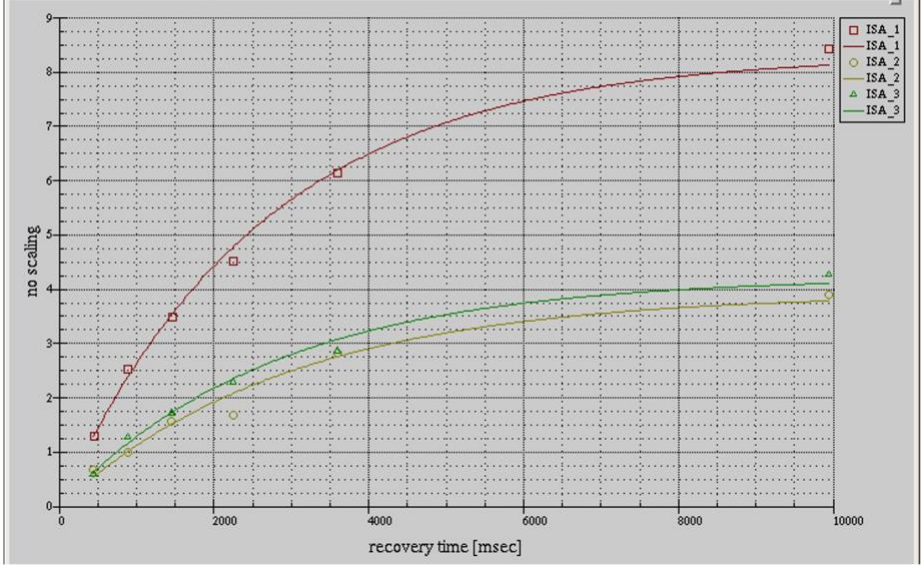

Figure 6.10 T1 relaxation values post-ablation for mouse 3 with adrenal tumor. (A) T2 RARE image used for ROI placement. ISA 1 is for the region with the tumor; ISA 2 and ISA 3 are for regions outside the tumor. (B) T1 relaxation values shown in msec for each ROI. (C) Representative fit showing different recovery times.

A

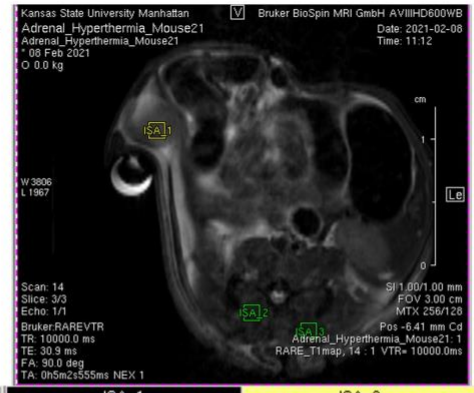

B

ROI name	ISA_1			ISA_2			ISA_3		
ROI area	0.0181 cm2			0.0181 cm2			0.0181 cm2		
parameter	value	std dev	usage	value	std dev	usage	value	std dev	usage
absolute bias	0	0	fixed	0	0	fixed	0	0	fixed
signal intensity	7.38456	0.377324	varied	4.55489	0.299483	varied	4.02334	0.479734	varied
T1 relaxation time [ms]	2040.32	181.341	varied	2951.87	324.206	varied	2695.8	494.942	varied
std dev of the fit	0.199808			0.127411			0.174961		
recovery time [msec]	mean	std dev	func	mean	std dev	func	mean	std dev	func
442.15	1.59	0.24212	1.44	0.63	0.170967	0.63	0.64	0.203945	0.61
884.12	2.63	0.35183	2.60	1.28	0.325398	1.18	0.93	0.225928	1.12
1452.30	3.72	0.454255	3.76	1.50	0.475493	1.77	1.69	0.285936	1.68
2248.94	4.66	0.557264	4.93	2.63	0.559932	2.43	2.56	0.381721	2.28
3592.98	5.85	0.697415	6.12	3.06	0.91202	3.21	3.01	0.57565	2.96
9942.15	7.69	0.832203	7.33	4.41	0.652892	4.40	3.71	0.776023	3.92

C

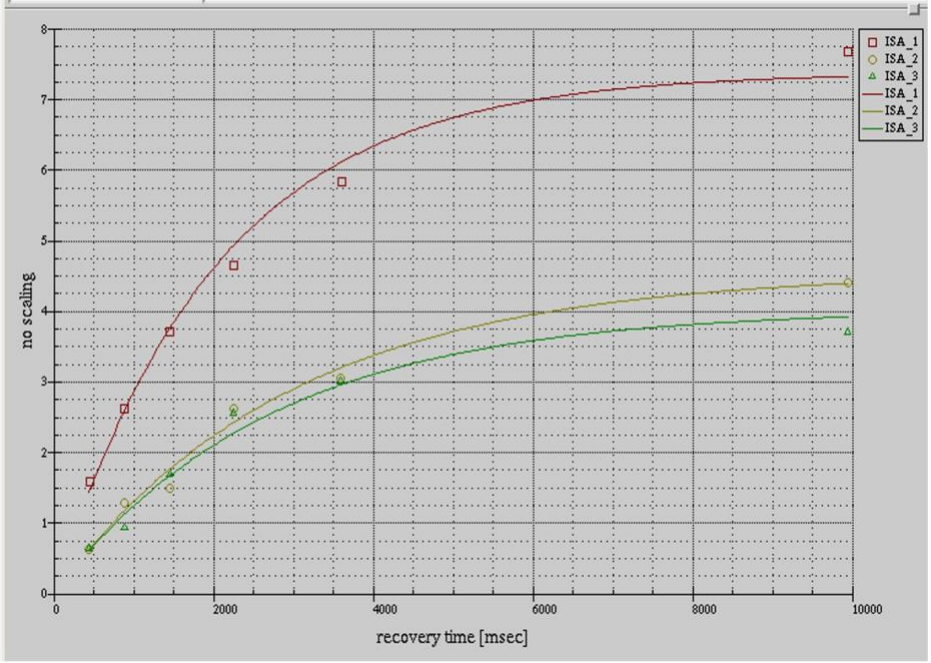

Figure 6.11 T1 relaxation values pre-ablation for mouse 21 with adrenal tumor. (A) T2 RARE image used for ROI placement. ISA 1 is for the region with the tumor; ISA 2 and ISA 3 are for regions outside the tumor. (B) T1 relaxation values shown in msec for each ROI. (C) Representative fit showing different recovery times.

A

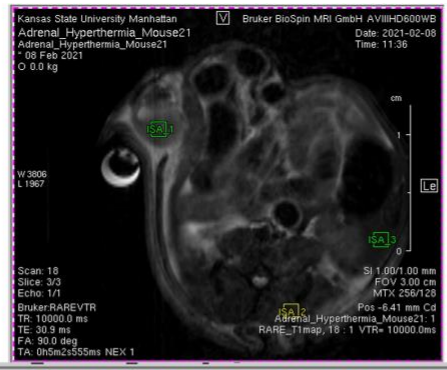

B

ROI name	ISA_1			ISA_2			ISA_3		
ROI area	0.0181 cm2			0.0198 cm2			0.0181 cm2		
parameter	value	std dev	usage	value	std dev	usage	value	std dev	usage
absolute bias	0	0	fixed	0	0	fixed	0	0	fixed
signal intensity	8.15872	0.263219	varied	4.22228	0.1706	varied	3.79055	0.142533	varied
T1 relaxation time [ms]	2605.25	139.471	varied	2727	196.773	varied	2931.5	196.337	varied
std dev of the fit	0.0886604			0.0873319			0.0718717		
recovery time [msec]	mean	std dev	func	mean	std dev	func	mean	std dev	func
442.15	1.26	0.24	1.19	0.66	0.24	0.63	0.57	0.157791	0.53
884.12	2.12	0.29	2.21	1.14	0.54	1.17	0.92	0.231772	0.99
1452.30	3.24	0.35	3.30	1.55	0.63	1.74	1.57	0.234102	1.48
2248.94	4.56	0.40	4.50	2.44	0.67	2.37	1.99	0.278502	2.03
3592.98	5.97	0.59	5.89	3.23	1.09	3.09	2.62	0.260439	2.68
9942.15	7.83	1.01	7.92	4.09	0.79	4.11	3.71	0.395293	3.66

C

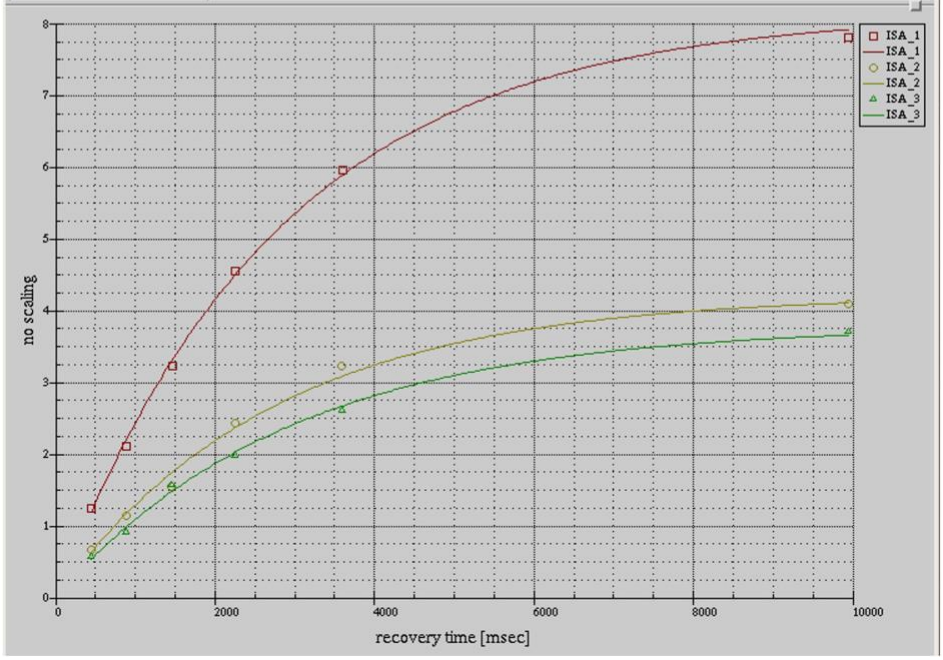

Figure 6.12 T1 relaxation values post-ablation for mouse 21 with adrenal tumor. (A) T2 RARE image used for ROI placement. ISA 1 is for the region with the tumor; ISA 2 and ISA 3 are for regions outside the tumor. (B) T1 relaxation values shown in msec for each ROI. (C) Representative fit showing different recovery times.

A

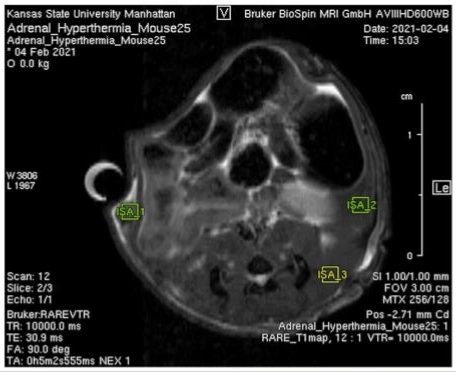

B

ROI name	ISA_1			ISA_2			ISA_3		
ROI area	0.0181 cm2			0.0181 cm2			0.0181 cm2		
parameter	value	std dev	usage	value	std dev	usage	value	std dev	usage
absolute bias	0	0	fixed	0	0	fixed	0	0	fixed
signal intensity	7.91154	0.142965	varied	4.71164	0.0594399	varied	5.24871	0.150645	varied
T1 relaxation time [ms]	2879.64	82.5148	varied	3041.5	60.932	varied	3290.24	176.484	varied
std dev of the fit	0.0551463			0.022922			0.0886299		
recovery time [msec]	mean	std dev	func	mean	std dev	func	mean	std dev	func
442.15	1.15	0.27	1.13	0.64	0.163393	0.64	0.70	0.171608	0.66
884.12	2.06	0.36	2.09	1.22	0.185378	1.19	1.22	0.171649	1.24
1452.30	3.10	0.47	3.13	1.78	0.254163	1.79	1.83	0.196021	1.87
2248.94	4.41	0.66	4.29	2.44	0.309619	2.46	2.75	0.245148	2.60
3592.98	5.58	0.78	5.64	3.23	0.392267	3.27	3.35	0.298472	3.49
9942.15	7.66	1.03	7.66	4.56	0.536775	4.53	5.01	0.270006	4.99

C

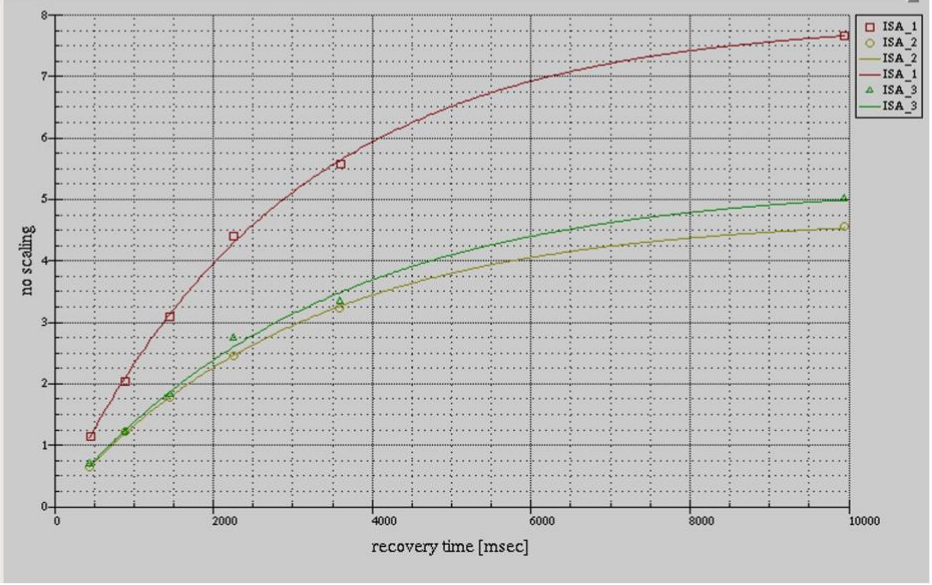

Figure 6.13 T1 relaxation values pre-ablation for mouse 25 with adrenal tumor. (A) T2 RARE image used for ROI placement. ISA 1 is for the region with the tumor; ISA 2 and ISA 3 are for regions outside the tumor. (B) T1 relaxation values shown in msec for each ROI. (C) Representative fit showing different recovery times.

A

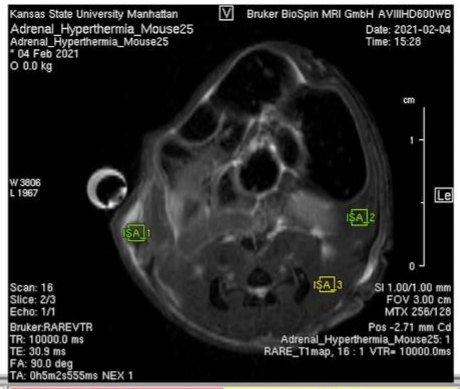

B

ROI name	ISA_1			ISA_2			ISA_3		
ROI area	0.0181 cm2			0.0181 cm2			0.0181 cm2		
parameter	value	std dev	usage	value	std dev	usage	value	std dev	usage
absolute bias	0	0	fixed	0	0	fixed	0	0	fixed
signal intensity	7.05378	0.199256	varied	4.61728	0.106634	varied	4.83828	0.154187	varied
T1 relaxation time [ms]	3364.03	142.586	varied	3133.41	110.497	varied	3543.47	192.866	varied
std dev of the fit	0.0598093			0.0353853			0.0694181		
recovery time [msec]	mean	std dev	func	mean	std dev	func	mean	std dev	func
442.15	0.89	0.22	0.87	0.61	0.167714	0.61	0.62	0.176767	0.57
884.12	1.64	0.33	1.63	1.13	0.196377	1.14	1.07	0.193582	1.07
1452.30	2.50	0.42	2.47	1.74	0.219009	1.71	1.66	0.219817	1.63
2248.94	3.46	0.61	3.44	2.38	0.287255	2.36	2.31	0.23092	2.27
3592.98	4.43	0.75	4.63	3.06	0.380157	3.15	2.97	0.241459	3.08
9942.15	6.80	1.04	6.69	4.48	0.621658	4.42	4.61	0.35559	4.55

C

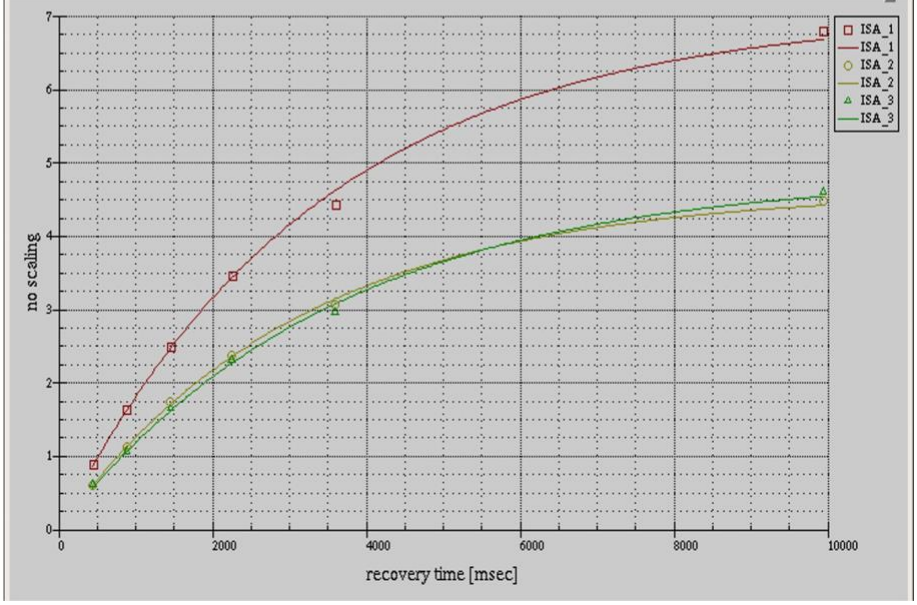

Figure 6.14 T1 relaxation values post-ablation for mouse 25 with adrenal tumor. (A) T2 RARE image used for ROI placement. ISA 1 is for the region with the tumor; ISA 2 and ISA 3 are for regions outside the tumor. (B) T1 relaxation values shown in msec for each ROI. (C) Representative fit showing different recovery times.

Appendix B - Supporting information for Chapter 3

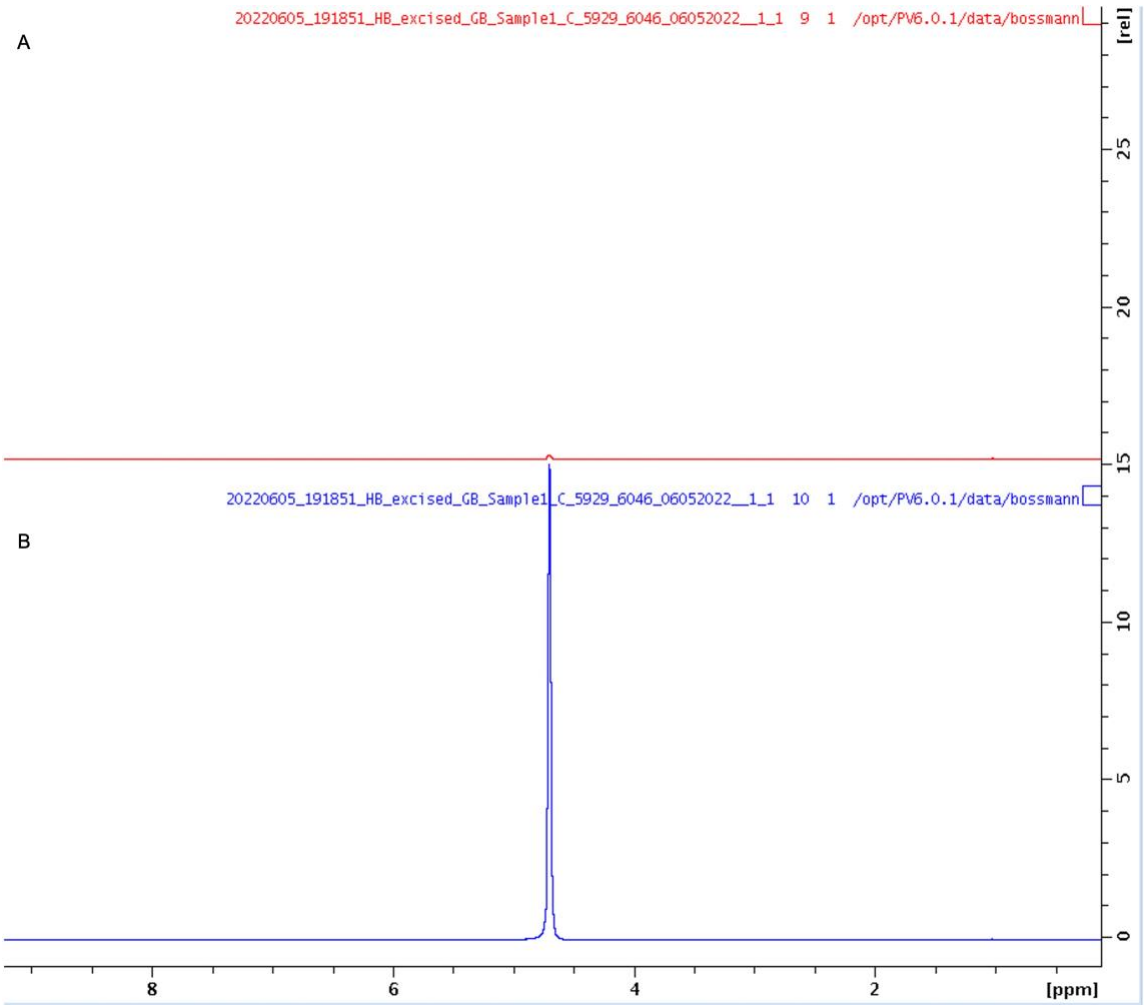

Figure 6.15 ^{1}H-MRS of glioblastoma sample 1 excised from a human subject. Spectrum with (A) VAPOR water suppression and (B) without water suppression.

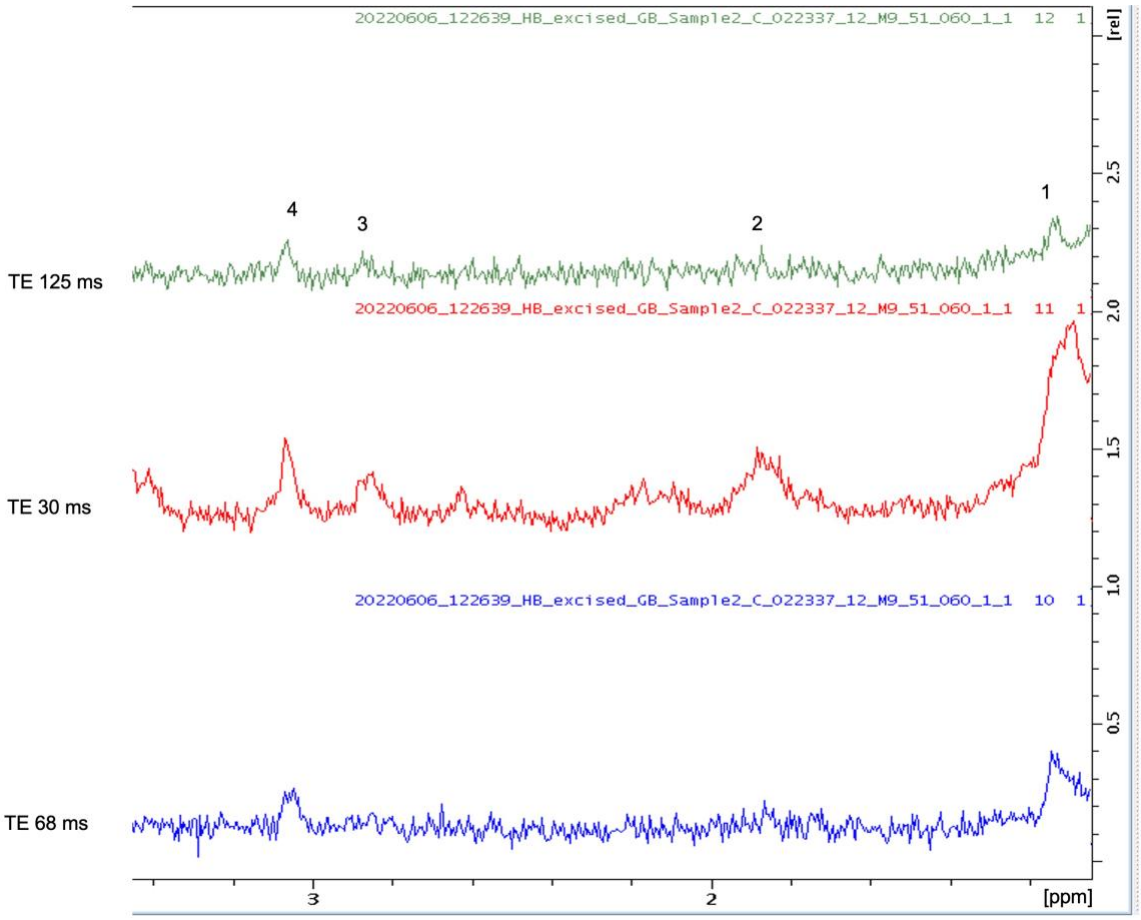

Figure 6.16 ^{1}H-MRS acquired with different TEs for glioblastoma sample 2 excised from a human subject. Varying TEs of 125 ms (green), 30 ms (red), and 68 ms (blue) were used. Signals were detected from lactate (1), N-acetyl aspartate (2), creatine (3), and total choline (4). TE, echo time

Appendix C - Supporting information for Chapter 4 and Chapter 5

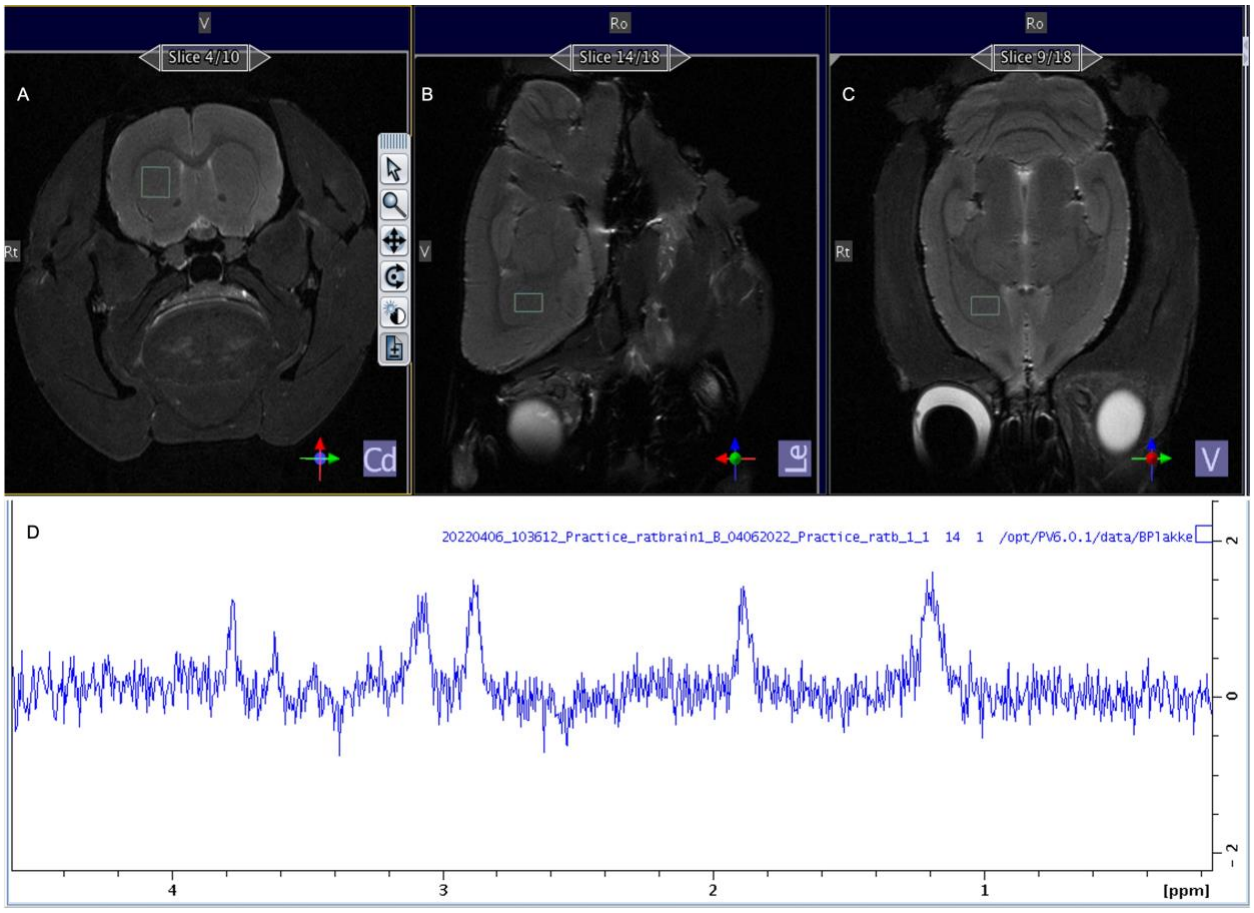

Figure 6.17 ^{1}H-MRS acquired from the caudate region of a rat brain *ex vivo*. Axial (A), sagittal (B) and coronal (C) T2 RARE images showing voxel placement in the caudate region. Voxel size was 2 x 2 x 1.2 mm^3. Representative spectrum for the voxel is shown in (D).